Modeling the Influence of Surface Pitting on Contact Pressure and Friction Coefficient Under Elastohydrodynamic Lubrication Conditions

by

Hengameh Sadat MIRKARIMI

THESIS PRESENTED TO ÉCOLE DE TECHNOLOGIE SUPÉRIEURE IN PARTIAL FULFILLMENT FOR A MASTER'S DEGREE WITH THESIS IN MECHANICAL ENGINEERING
M.A.Sc.

MONTREAL, JULY 22 2020

ÉCOLE DE TECHNOLOGIE SUPÉRIEURE
UNIVERSITÉ DU QUÉBEC

© Copyright 2020 reserved by Hengameh Sadat Mirkarimi

© Copyright reserved

It is forbidden to reproduce, save or share the content of this document either in whole or in parts. The reader who wishes to print or save this document on any media must first get the permission of the author.

BOARD OF EXAMINERS

THIS THESIS HAS BEEN EVALUATED

BY THE FOLLOWING BOARD OF EXAMINERS

Mr. Raynald Guilbault, Thesis Supervisor
Mechanical Engineering Department at École de technologie supérieure

Mr. Patrick Terriault, President of the Board of Examiners
Mechanical Engineering Department at École de technologie supérieure

Mr. Tan Pham, Member of the jury
Mechanical Engineering Department at École de technologie supérieure

THIS THESIS WAS PRENSENTED AND DEFENDED

IN THE PRESENCE OF A BOARD OF EXAMINERS AND PUBLIC

JULY 14, 2020

AT ÉCOLE DE TECHNOLOGIE SUPÉRIEURE

ACKNOWLEDGMENT

First and foremost, I would like to express my sincerest gratitude to my supervisor, Professor Raynald Guilbault, for his constant support, patient guidance, and encouragement during my studies. His persistent help and advice have been very helpful to me throughout the completion of my thesis. I have gained so much, not only professionally but also personally, during my study here. This is an experience that will remain with me and inspires me for the rest of my life.

My special thanks are due to my parents, Mostafa and Zhaleh, for their unconditional love, generous support, and continued inspiration. I appreciate all the sacrifices they have done for me. I owe all my success in life to my beloved parents. I, also thank my brother, Foad, and my sister, Talayeh, for their endless love, encouragement, and friendship. Even if we are miles apart, you are always in my heart.

Last but not the least, my heartfelt appreciation goes to my beloved husband, Hossein, who has been always supporting and encouraging me in the moments when there was no one else. Without his devotion, support, and sacrifices, I could have never come this far.

Modélisation de l'influence des piqûres de surface sur les pressions de contact et les coefficients de frottement en régime de lubrification élastohydrodynamique

Hengameh Sadat MIRKARIMI

RÉSUMÉ

Les composants mécaniques utilisés dans les machines sont lubrifiés pour prévenir l'usure et améliorer leur efficacité. La lubrification réduit la génération de chaleur, atténue la pression de surface, et enfin améliore le fonctionnement des équipements. En fonction ses charges externes et des vitesses, différents régimes de lubrification peuvent exister. Plus précisément, le régime élastohydrodynamique décrit le comportement d'un lubrifiant entre surfaces soumises à une charge externes concentrée sur une petite zone de contact, et provoquant des déformations élastiques d'amplitude comparable à l'épaisseur du film de lubrifiant. Ce régime de lubrification apparaît principalement entre des surfaces non conformes.

Les modèles numériques classiques de lubrification élastohydrodynamique ont été développés pour prédire les distributions de pression et les épaisseurs de film de lubrifiant générées entre surfaces lisses ou rugueuses. Cependant, dans des applications réelles, différents types de dégradation peuvent détériorer la qualité des surfaces, et entraîner des changements micro et souvent macroscopiques des conditions de contact.

Les piqûres font partie des défaillances de surface les plus courantes. Ce dommage résulte de chargements cycliques. La présence de piqûres de surface affecte de manière significative les distributions de pression, les épaisseurs de film de lubrifiant et les coefficients de frottement. Ce mémoire s'attelle d'abord à modéliser le contact sec entre deux cylindres. L'approche adoptée s'appuie sur l'algorithme proposé par Hartnet. Cet algorithme est complété par l'ajout de cellules de pression en miroir, combinées au facteur de sur-correction proposé par Guilbault, afin d'éliminer les distributions de contrainte normale et de cisaillement générées sur les surfaces libres. Par la suite, dans le but d'obtenir un modèle élastohydrodynamique pour surfaces lisses, la démarche proposée ajoute l'équation de Reynolds à la solution. La validation du modèle repose sur une comparaison des distributions de pression et épaisseurs de film prédites à des valeurs de référence. Le processus considère différentes conditions de charge et de vitesse. Ensuite, les développements intègrent le terme de l'équation de Reynolds variant dans le temps. Cet élément permet de modéliser des piqûres de surface. L'étude considère différentes profondeurs et configurations de piqûres, afin de comprendre l'influence des défauts de surface sur la lubrification de rouleaux cylindriques. L'analyse compare les réponses obtenues pour des surfaces lisses et dégradées. Les prédictions du modèle numérique confirment que la présence de piqûres affecte de manière importante les pressions de surface, les épaisseurs de film de lubrification, ainsi que les coefficients de frottement.

Mots-clés : Lubrification élastohydrodynamique, pression de surface, épaisseur de film, friction, piqûres, défauts de surface

Modeling the Influence of Surface Pitting on Contact Pressures and Friction Coefficients Under Elastohydrodynamic Lubrication Conditions

Hengameh Sadat MIRKARIMI

ABSTRACT

Mechanical components used in machinery are lubricated to prevent wear and enhance their efficiency. Fluid film lubrication reduces heat generation, attenuates surface pressure, and eventually, results in improvements in equipment operation. Depending on external loads and speed, different lubrication regimes may take place. Specifically, the elastohydrodynamic regime describes the lubrication response produced between two mating surfaces sustaining an external load concentrated on a small contact area and causing elastic deformations comparable to the fluid film thickness. This regime of lubrication mainly appears between non-conformal surfaces.

Classical numerical models for elastohydrodynamic lubrication were developed to predict the pressure distributions and the lubricant film thickness profiles generated between smooth or rough surfaces. In addition, in real-world applications, different failure types deteriorate the surface quality and cause micro and even macro changes in the contact conditions.

Pitting is one of the most common surface failures. This damage results from cyclic contact loadings. Surface pits significantly affect pressure distributions, lubricant film thickness, and friction coefficients. In this thesis, we examine the consequences of surface pitting on the line contact problem. The thesis first tackles the modeling of the dry contact between two cylinders. The considered approach is based on the Hartnet algorithm. This algorithm is enhanced by the mirroring of the pressure patches associated with the Guilbault's overcorrection factor to eliminate the shear and normal stress distributions generated onto the free surfaces. Afterward, the model preparation introduces the Reynolds equation to the solution and form the elastohydrodynamic model for smooth surfaces. The model validation compares the predicted pressure distributions and film thicknesses to reference values. This process considers different loading and speed conditions. Then, the developments integrate the time-variant term of the Reynolds equation into the model. This element allows for modeling surface pits. The study examines different pit depths and arrangements to investigate the influence of surface damages on the lubrication of cylindrical rollers. The analysis compares the response established for smooth and pitted surfaces. The numerical predictions confirm that the introduction of pits significantly affects the surface pressures, the film thicknesses, and the coefficients of friction.

Keywords: Elastohydrodynamic lubrication, surface pressure, film thickness, friction, pitting, surface failure

TABLE OF CONTENTS

Page

INTRODUCTION 1

CHAPTER 1 DRY CONTACT 9
1.1 Introduction 9
1.2 Contact problem 9
1.3 Modeling 15
  1.3.1 Dry Contact Problem 15
  1.3.2 Mirroring Process 16
  1.3.3 Correction Factor 19
  1.3.4 Misalignment 21
1.4 Conclusion 27

CHAPTER 2 EHL MODELING 29
2.1 Introduction 29
2.2 Reynolds Equation 29
2.3 Film Thickness 31
2.4 Lubricant Properties 33
  2.4.1 Lubricant density 33
  2.4.2 Lubricant viscosity 34
  2.4.3 Carreau expression 34
2.5 Numerical Simulation 35
2.6 Conclusion 45

CHAPTER 3 EHL MODELING OF PITTED SURFACES 47
3.1 Introduction 47
3.2 Surface pitting failure 47
3.3 Surface pitting simulation 48
3.4 Validation-Film thickness and pressure distribution 52
3.5 Single pit simulation 57
3.6 Effect of pit depth 64
3.7 Effect of pit arrangement 67
3.8 Friction 75
  3.8.1 Validation-Calculation of friction coefficients 77
  3.8.2 Single pit simulation 79
  3.8.3 Effect of pit depth 81
  3.8.4 Effect of pit arrangement 82
3.9 Conclusion 84

CONCLUSION 87

RECOMMENDATIONS 89

LIST OF BIBLIOGRAPHICAL REFERENCES 91

LIST OF TABLES

Page

Table 1.1 Dry contact simulation parameters 16

Table 3.2 Simulation conditions and dent dimensions-Taken from (Warhadpande & Sadeghi, 2010)...53

Table 3.3 Comparison of the pressure profile and film thickness extremums for the two numerical models 54

Table 3.4 Experimental (Taken from (Höhn et al., 2006)) and simulation parameters...56

Table 3.5 Comparison of the pressure distribution and film thickness extremums for the experimental measurements and the present model......................57

Table 3.6 Material parameters and problem conditions for single pit simulation 58

Table 3.7 Rollers and lubricant properties Taken from (Najjari & Guilbault, 2014)...78

LIST OF FIGURES

Page

Figure 0.1 Different lubrication regimes 1

Figure 0.2 Stribeck curve demonstrating different lubrication regimes Taken from (Chong & De La Cruz, 2014) 3

Figure 0.3 Schematic conformal and non-conformal mating surfaces Taken from (Shirzadegan, 2016) 4

Figure 0.4 Pitting failure in a gear-Taken from (“Defects Treated (Gears) |Novexa,” n.d.) 5

Figure 1.1 (a) Point contact between two spheres (b) Line contact between two cylinders 10

Figure 1.2 Contact area expansion during load application-Taken from (Collins, 2015) 10

Figure 1.3 The contact of elastic bodies-Taken from (Hartnett, 1980) 11

Figure 1.4 Contact of arbitrarily shaped indenters-Taken from (Hartnett, 1980) 13

Figure 1.5 Numerical solution of dry contact problem 15

Figure 1.6 Surface Pressure Distribution-right circular cylinder 16

Figure 1.7 Surface Pressure Distribution-right circular cylinder - 1st step mirroring process 18

Figure 1.8 Surface Pressure Distribution-right circular cylinder - 2nd step mirroring process 18

Figure 1.9 Correction process of quarter-plane free boundary-Taken from (Guilbault, 2011) 19

Figure 1.10 Surface Pressure Distribution-right circular cylinder-1st step mirroring process-Effect of the correction factor 20

Figure 1.11 Comparison between different modification methods of pressure distribution correction 21

Figure 1.12 Two types of misalignments (a) Perpendicular to the contact plane, (b) In contact plane 22

Figure 1.13 Surface Pressure Distribution-right circular cylinder-1st step mirroring process -0.05 radians misalignment....23

Figure 1.14 Surface Pressure Distribution-right circular cylinder-1st step mirroring process and correction factor- 0.05 radians misalignment....23

Figure 1.15 Surface Pressure Distribution-right circular cylinder-1st step mirroring process and correction factor - 0.5 radians in-plane misalignment (a) Symmetric view, (b) Top view 25

Figure 1.16 Surface Pressure Distribution-right circular cylinder-1st step mirroring process - effect of different radii....26

Figure 1.17 Surface Pressure Distribution-right circular cylinder-1st step mirroring process and correction factor - effect of different radii 27

Figure 2.1 Equivalent contact for the point contact problem -Taken from (Shirzadegan, 2016) 32

Figure 2.2 Equivalent contact for the line contact problem-Taken from (Shirzadegan, 2016) 32

Figure 2.3 Flowchart of the numerical solution 37

Figure 2.4 EHL pressure distribution ($\mathrm{F} = 6000$ N, ue $= 2.7$ m/s) 38

Figure 2.5 Comparison between dry contact and EHL solution along with the film thickness ($\mathrm{F} = 6000$ N, ue $= 2.7$ m/s)....39

Figure 2.6 Pressure distribution at the midplane of EHL contact for different loads (ue $= 2.7$ m/s) 40

Figure 2.7 Pressure distribution at the midplane of EHL contact for different rolling speeds ($\mathrm{F} = 5000$ N)....40

Figure 2.8 Lubricant film thickness ($\mathrm{F} = 6000$ N, ue $= 2.7$ m/s)....41

Figure 2.9 Film thickness at the midplane of EHL contact for different loads (ue $= 2.7$ m/s) 42

Figure 2.10 Film thickness at the midplane of EHL contact for different rolling speeds ($\mathrm{F} = 5000$N) 42

Figure 2.11 Lubricant viscosity at the midplane of EHL contact for different loads....43

Figure 2.12 Lubricant viscosity at the midplane of EHL contact for different rolling speeds....44

Figure 2.13 Lubricant density at the midplane of EHL contact for different loads 44

Figure 2.14 Lubricant density at the midplane of EHL contact for different rolling speeds 45

Figure 3.1 Crater formation for the two pitting types-Taken from (“Polishing - Gear Failures - Failure Atlas - ONYX InSight,” n.d.) 48

Figure 3.2 Schematic single pit passing through the contact zone 49

Figure 3.3 Modified flowchart of the numerical solution 51

Figure 3.4 Pit passing through contact zones 52

Figure 3.5 Result comparison (a) EHL pressure distribution for the smooth condition, (b) EHL film thickness profile for the smooth condition, (c) EHL pressure distribution for the pitted surface condition, and (d) EHL film thickness profile for the pitted surface condition. 54

Figure 3.6 Transverse surface texture shape study in (Höhn et al., 2006) 55

Figure 3.7 Comparing the experimental pressure distribution in (Höhn et al., 2006) with present model 57

Figure 3.8 3D EHL pressure distribution when the pit position $xp = -0.78\ mm$ 59

Figure 3.9 3D EHL pressure distribution when the pit position $xp = -0.67\ mm$ 60

Figure 3.10 3D EHL pressure distribution when the pit position $xp = -0.56\ mm$ 60

Figure 3.11 3D EHL pressure distribution when the pit position $xp = 0$ 61

Figure 3.12 3D EHL pressure distribution when the pit position $xp = 0.27\ mm$ 61

Figure 3.13 3D EHL pressure distribution when the pit position $xp = 0.56\ mm$ 62

Figure 3.14 2D EHL pressure distributions at the central axial position of the rollers for the pit locations (a) $xp = -0.78\ mm$, (b) $xp = -0.67\ mm$, (c) $xp = -0.56\ mm$, (d) $xp = 0$, (e) $xp = 0.27\ mm$, (f) $xp = 0.56\ mm$ 63

Figure 3.15 Longitudinal pressure distribution in the presence of a single pit passing through the contact zone 64

Figure 3.16 Effect of pit depth - 2D EHL pressure distributions at the central axial position of the rollers for the pit locations (a) $xp = -0.78\ mm$, (b) $xp = -0.67\ mm$, (c) $xp = -0.56\ mm$, (d) $xp = 0$, (e) $xp = 0.27\ mm$, (f) $xp = 0.56\ mm$ 66

Figure 3.17 Multiple pit arrangements 67

Figure 3.18 3D EHL pressure distribution for the 3-pit configuration 68

Figure 3.19 3D EHL pressure distribution for the 9-pit configuration 69

Figure 3.20 3D EHL Film thickness profile for the 3-pit configuration 69

Figure 3.21 3D EHL Film thickness profile for the 9-pit configuration 70

Figure 3.22 2D effect of pit configuration at the axial position crossing the central pit - (a) 2D EHL pressure distributions and (b) EHL film thickness profiles 72

Figure 3.23 Longitudinal pressure distributions calculated along the x = 0 for two multipit configurations 74

Figure 3.24 Comparing friction coefficient derived from the current model and reference (Najjari & Guilbault, 2014) 79

Figure 3.25 Effect of a single pit on the friction coefficient (a) Changes in friction coefficient with pit location in the contact zone when SRR $= 0.02$, (b) Effect of SRR on friction coefficients calculated for the single pit and the smooth surface conditions 80

Figure 3.26 Effect of single pit depth on the friction coefficient (a) Changes in friction coefficient with pit location in the contact zone when $SRR = 0.02$, (b) Effect of SRR on friction coefficients calculated for single-pit configurations with different depths 82

Figure 3.27 Effect of pits arrangement on the friction coefficient (a) Changes in friction coefficient with pit location in the contact zone when $SRR = 0.02$, (b) Effect of SRR on friction coefficients calculated for different pit arrangements 84

LIST OF SYMBOLS

A	Contact area
a	Half-length of a cell
b	Half-width of a cell
d_d	Dent depth
d_w	Dent width
E	Elastic modulus
E'	Equivalent modulus
F	Applied load
F_f	Friction force
f_c	Friction coefficient
$f_{kj,ip}$	Flexibility matrix (Influence coefficient relating cell j strip k to cell p strip i)
G	Dimensionless material parameter
G_f	Lubricant modulus
g	Initial separation of undeformed solids
h	Film thickness
h_0	Minimum film thickness
L	Contact length
l_c	Separation between two circumferential pit rows
l_{l1}, l_{l2}	Distance from cylinder ends
l_{lp}	Separation between two consecutive pits

n	Slope in the lubricant shear-thinning zone
p	Pressure
P^*	Mirror corrected pressure
P_{HZ}	Maximum dry contact pressure
$\bar{P}_{kj}$	Average pressure on cell j strip k
P_d	Pit depth
P_l	Pit length
P_w	Pit width
R	Equivalent radius
R_x, R_y	Equivalent radius in x and y directions
R_{ix}, R_{iy}	Radius of curvature i in x and y directions
S_0	Dimensionless slope of viscosity-temperature relationship
T	Temperature
T_0	Ambient temperature
t	Time
U	Dimensionless speed parameter
u_e	Rolling speed
u_1, u_2	Velocities of surfaces 1 and 2
w	Total load
W	Dimensionless load parameter
w_i	Normal displacement of body i
w_{i_p}	Normal displacement of body i at the center of cell p

x_p	Pit location
$\bar{x}, \bar{y}$	Local coordinate position
z_0	Dimensionless viscosity-pressure index
z_i	Separation of body i to plane
z_{i_p}	Separation of body i to plane at the center of cell p
α	Pressure-viscosity coefficient
α'	Approach of the bodies
β	Density-temperature coefficient
$\dot{\gamma}$	Shear rate
δ	Elastic deformation of the contact surfaces
δ_{ik}	Kronecker delta
η	Dynamic viscosity
η_0,η_1	Shear independent dynamic viscosity
Λ	Limiting shear stress-pressure coefficient
ν	Poisson's ratio
ρ	Density
ρ_0	Density at ambient temperature
τ	Shear stress
τ_l	Limiting shear stress
ψ	Guilbault's correction factor

INTRODUCTION

Background

In most types of machinery, several rotating or sliding objects are in contact with each other. To reduce friction and wear between sliding surfaces, a substance should be interposed between them. This process is called lubrication. Generally, fluid film lubrication reduces heat generation and moderates contact pressure distribution, which eventually results in a more efficient operation of the equipment. In many mechanical components, such as gears, roller/ball bearings, clutches, and tappet cam mechanisms, contacts take place under various lubrication regimes. Regarding the load and the speed of the contacting surfaces, different lubrication regimes are categorized (Bolander & Sadeghi, 2006) as shown in Figure 0.1.

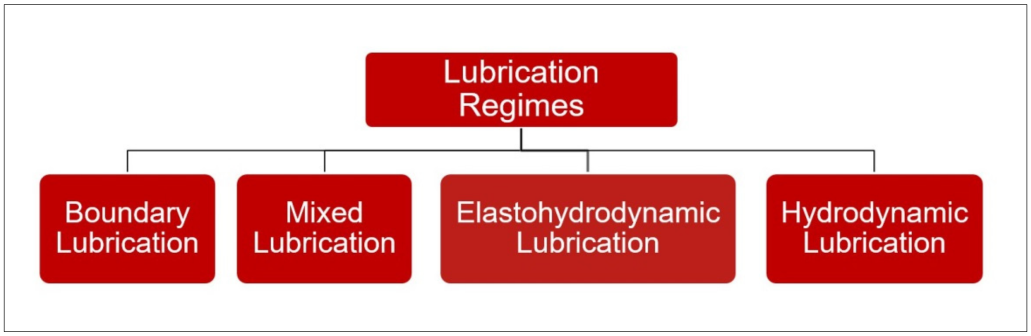

Figure 0.1 Different lubrication regimes

a. Boundary lubrication

In this mode of lubrication, solid surfaces come into contact mainly at their asperities. Therefore, the surface asperities are considered as the principal load supporters. In this case, the role of the lubricant and its hydrodynamic effects in carrying the load are negligible. Due to the asperities contact, wear and friction are significant in this lubrication regime.

b. Mixed lubrication

The transient regime between boundary lubrication and hydrodynamic lubrication is called mixed lubrication. The solid bodies are not completely separated by the lubricant film, and there are some asperity contacts between the bodies. The hydrodynamic effects of the lubricant are more considerable in this mode. The load is, therefore, being carried by both asperities and the lubricant film.

c. Elastohydrodynamic lubrication (EHL)

This regime of lubrication is found in nonconforming surfaces and heavy load conditions. Due to these conditions, the elastic strain in the contact area changes the separation of the mating surfaces while the piezo-viscous nature of the lubricant causes the viscosity increases. In other words, the lubricant film thickness in EHL highly depends on a combination of elastic deformation of the solid surfaces and considerable viscosity augmentation through the high-pressure zone. In such conditions, asperity contacts are not completely eliminated but remain sparse.

d. Hydrodynamic lubrication

The main characteristic of hydrodynamic lubrication is that the load is entirely carried by the lubricant film while the mating surfaces are completely separated by the lubricant film. This lubrication regime prevents contacts between solid surfaces. As for the elastohydrodynamic regime, in hydrodynamic lubrication, the motion of the mating surfaces plays the main role in the lubricant flow.

In industry, most contacts are lubricated to control friction and wear. In real applications, such as cylinder liners, piston rings, rolls, and machine tools, contacts operate in a specific lubrication regime. To optimize the contact regarding friction, on the one hand, and lifetime, on the other hand, it is necessary to predict the lubrication regime in which such contacts operate (Gelinck & Schipper, 2000). In lubricated sliding, the friction coefficient during lubrication is potentially influenced by sliding speed, mean contact pressure or normal load, and dynamic viscosity. In the lubrication theory, these three quantities often appear in a single quantity called the Sommerfeld number ($\eta U/p$) where η, U, and p correspond to viscosity, velocity and pressure respectively (Gelinck & Schipper, 2000).

Experiments on the lubrication of material surfaces as a function of the Sommerfeld number often reduce to the Stribeck curve (Figure 0.2). Plotting the Stribeck curve is still a convenient method for examining the effect of important variables of sliding speed and normal load to indicate lubrication mechanisms and predict the lubrication regime. EHL friction, sometimes called traction, is important as it is directly associated with machine components performance, efficiency, and energy consumption. This thesis focuses on EHL condition.

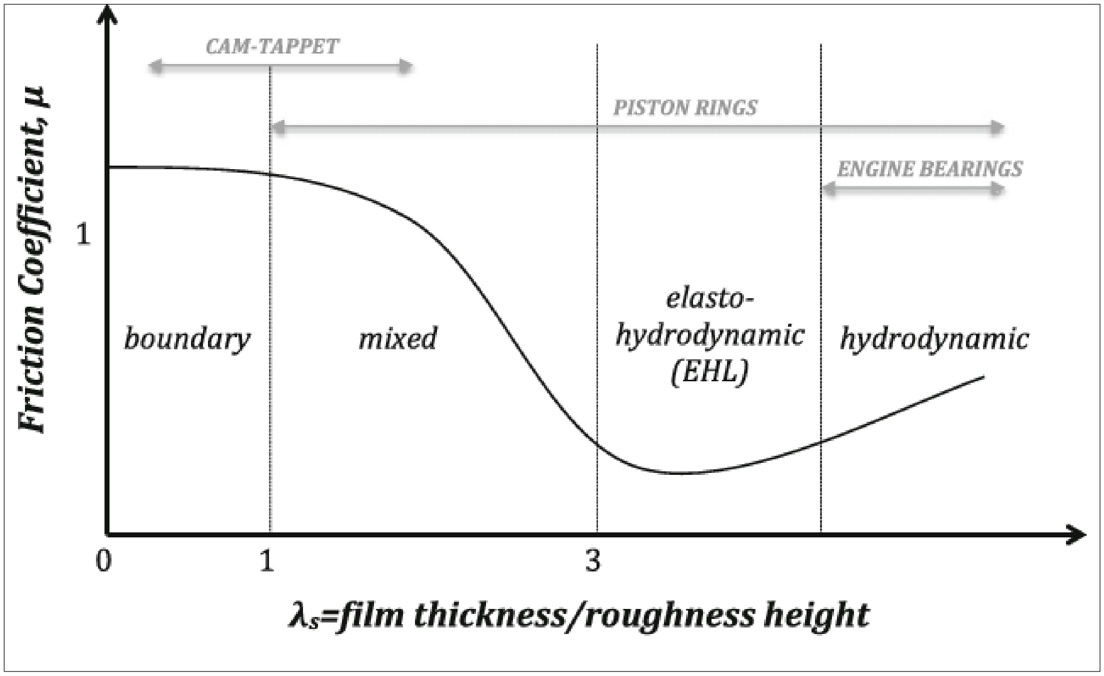

Figure 0.2 Stribeck curve demonstrating different lubrication regimes
Taken from (Chong & De La Cruz, 2014)

In the analysis of the interaction between mating surfaces, two types of contact can be observed, namely conforming contacts and nonconforming contacts. For the conformal case, the curvatures fit closely together, and the contact area is large before any deformation. On the other hand, in non-conformal contact, the curvatures of the surfaces do not match, and the contact area is small, and the contact pressure and stresses are therefore highly concentrated. (Figure 0.3) EHL mainly appears between nonconformal surfaces.

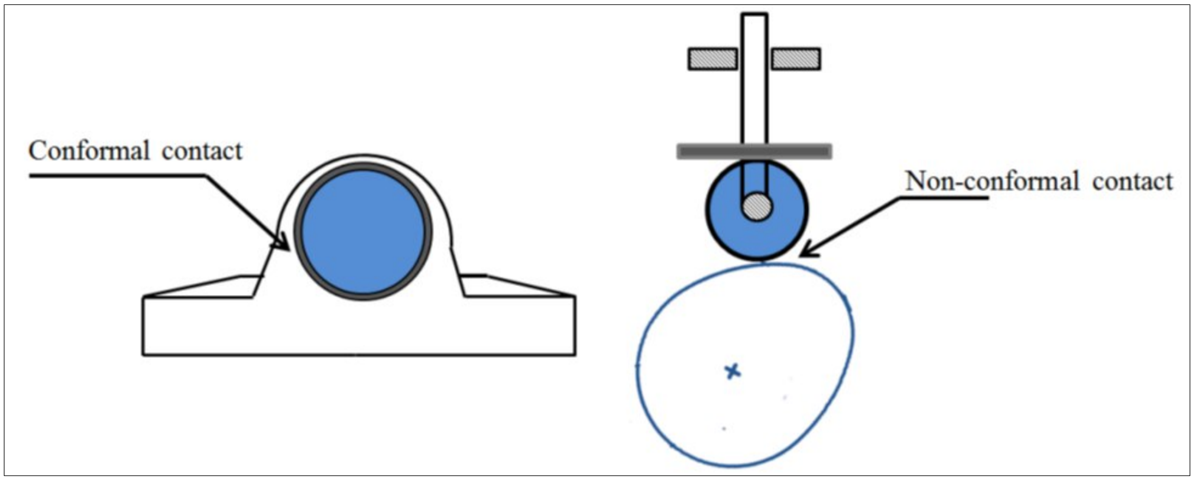

Figure 0.3 Schematic conformal and non-conformal mating surfaces
Taken from (Shirzadegan, 2016)

Although an efficient lubrication regime protects from adhesive and abrasive wear, contact fatigue remains inevitable. Contact fatigue results in micro-pitting and pitting (Guilbault & Lalonde, 2019). This mechanism takes place due to cyclic loadings. Figure 0.4 shows pitted gear surfaces. Based on the crack initiation location, this mode of failure is classified into two categories: surface pitting and subsurface pitting. Pits are formed in all rolling pairs but are particularly common in rolling bearings and gear transmission elements. In such cases, contact takes place under EHL conditions.

Surface defects like pitting can have deleterious effects on the efficiency of lubrication. The EHL theory is a proper method to study pitting failure and its effects. Pitting fatigue has been also studied in a few works over the years. Fatigue life calculation for the pitted surfaces is well studied in the literature. The experimental methods to model surface roughness in EHL conditions, such as light interferometry, have some limitations and difficulties, which is beyond the scope of this thesis. The numerical methods for simulating the topography both in dry contact and EHL conditions are, therefore, more popular. In dry contact condition, the friction between the mating objects plays the most important role in expediting the crack propagation. However, in EHL conditions, the lubricant may penetrate the crack and act as a wedge to form the pits (Datsyshyn & Panasyuk, 2001). In terms of surface pitting simulations, different models can be implemented. An artificial set of pits can be generated in the geometry using sinusoidal patterns (He, Ren, Zhu, & Wang, 2014). Also, a fast Fourier transform (FFT) can be employed to estimate the surface roughness and the pits (S. Liu, Wang, & Liu, 2000). To include more sophisticated patterns, some researchers tended to use two-dimensional (2D) models. Generally, modeling the line contact problem is a 2D problem. However, since the topography of the surface, i.e. the pits and cracks, is three-dimensional (3D), the whole formulation should be 3D to include the effect of the topography (Zhu, Wang, & Ren, 2009).

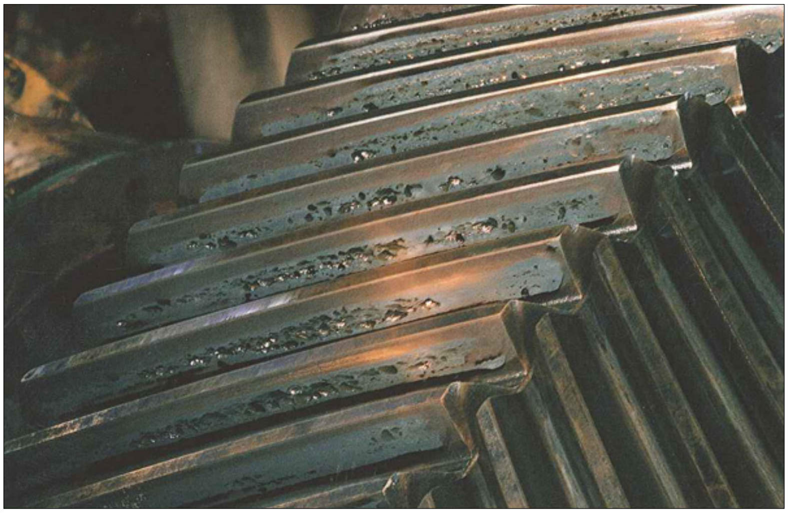

Figure 0.4 Pitting failure in a gear-Taken from ("Defects Treated (Gears) | Novexa," n.d.)

Literature review

During the years, several researchers have studied the EHL for different contact surfaces. As the pioneers, Grubin and Vinogradova (1949) investigated EHL theory by considering both elastic deformation and viscosity-pressure effect of the lubricant. Their model describes the mechanical behavior of the mating surfaces assuming that the elastic strain in the loaded region is equal to that of the dry contact problem. Dowson & Higginson (1967) presented a solution for highly loaded line contacts under EHL conditions by considering the film thickness as the dependent variable to the pressure distribution. Hamrock & Dowson (1975) investigated the EHL condition of elliptical contacts by comprehensively studying different loading conditions and material characteristics.

The EHL solution process couples Reynolds equation, elasticity equations, and piezo-viscous lubricant equation leading to numerically complicated problems. Many efforts have been made to find an efficient numerical solution of EHL problems. Different numerical approaches such as direct method, inverse method, quasi-inverse, and system approach methods have been reviewed by Hamrock and Tripp (1984). They presented the advantages and disadvantages of each approach. Okamura (1983) used the Newton-Raphson method to solve the system of finite element equations in the EHL problem. Their results mainly describe the lightly loaded EHL problems. Solutions for highly loaded cases were investigated by Houpert and Hamrock (1986) using adaptive non-uniform meshes to solve the EHL equations. In contrast to practical elements with a finite length such as gears and roller bearings, their solution was limited to infinite line contacts or point contact geometries. (KURODA, S., & ARAI, 1985) combined the finite difference and Newton-Raphson methods to solve the EHL problem for the finite cylindrical rollers. (Park & Kim, 1998) also provided a numerical solution of the EHL problem for the finite line condition. (Najjari & Guilbault, 2014) studied finite line thermal EHL problems for profiled rollers. They considered different roller profile corrections such as chamfered corners, rounded edges, and logarithmic profiles to investigate the edge contact effect on the pressure distribution and the lubricant film thickness.

In the case of experimental studies, (Wymer & Cameron, 1974) tested finite line contacts under the EHL condition. (Mostofi & Gohar, 1983) considered rollers with profiled edge under EHL conditions. Their investigations were, however, limited to low or moderate loads. (Masjedi & Khonsari, 2015) and (Olver & Dini, 2007) independently investigated the effect of surface properties such as roughness on the film thickness and pressure distribution. (Zhu, Ren, & Wang, 2009) used a 3D line contact EHL to predict the gear pitting fatigue life. Using the mixed EHL condition, (Li & Kahraman, 2013) studied the pitting failure modes. (Chue & Chung, 2000) investigated the mechanism of pitting caused by rolling contact using the fracture mechanics approach. They stated that the initial crack and its orientation, indentation force, friction, hydraulic pressure in the crack, and strained-hardened surface layer have critical effects on the pit formation. (Keer & Bryant, 1983) evaluated fatigue lives for rolling/sliding Hertzian contacts using a two-dimensional fracture mechanics approach. They assumed that the crack initiation life is small in comparison to the crack propagation life. (Fajdiga, Glodež, & Kramar, 2007) presented a computational model for the simulation of surface-initiated fatigue crack growth in contacting mechanical elements. As stated before, surface contact failures are very common and much effort has been made to investigate the problem, but progress has been limited due to the complexities in understanding the mechanism of surface pitting effects and the lack of effective ways to estimate friction. Hence, a comprehensive model to investigate the effects of such a surface failure on friction coefficient and contact pressures is needed.

Objectives of the research

As indicated above, this thesis focuses on EHL regime. It particularly concentrates on the influence of fatigue pits on the lubricant film formation. The first objective of the research pertains to developing a comprehensive numerical model to investigate the effects of surface pitting on contact pressures and friction coefficient under EHL conditions. According to this objective, the specific aims are defined as:

- Developing and validating a precise 3D EHL model which describes pitting influence on film thickness and pressure distribution under finite line contact condition
- Integration of free-boundary influence in EHL model
- Investigation of surface pitting impacts on contact pressures and friction coefficients

Thesis organization

This chapter presented an overview of the subject background. It also includes a definition of the research problem and objectives. The chapter also reviews the literature related to numerical modeling of the EHL problem along with the previous experimental studies. Chapter 1 covers the contact problem and dry contact condition and presents the governing system of equations. It also describes the adopted methodology (mirroring method, correction factor, and different types of body misalignments). The investigation results describe the pressure distributions predicted for different geometries. Chapter 2 covers the EHL model. It presents the governing equations for EHL conditions lubricant density and viscosity. This chapter also displays the film thickness and pressure distribution results predicted for selected systems. The dry contact and EHL models, used in chapters 1 and 2, have been previously introduced by other researchers, and we redeveloped and resolved the problem to make the foundation for modeling the pitting problem. Chapter 3 is dedicated to surface pitting in EHL condition. It describes the equations and models required to incorporate the effect of pitting in EHL as well as the friction coefficient equations. It finally shows the results obtained for various surfaces and operating conditions. The effect of pitting on the pressure distribution, film thickness profile, and the friction coefficient is concluded in the conclusion part. Finally, some future works are proposed in the recommendations section.

CHAPTER 1

DRY CONTACT

1.1 Introduction

Machinery elements consist of various contact systems that are transmitting forces and torques. Except for some specific applications such as pulley and belt systems in which friction is helpful, most of the contact surfaces are lubricated for enhancing the machine efficiency. To study the contact mechanics in lubricated surfaces, specifically in the EHL regime, the dry contact problem should be initially modeled. Our specific aim in this chapter is to derive the pressure distribution under dry contact conditions. This is the first of the essential steps in modeling the EHL contact problem.

1.2 Contact problem

The design and stress analysis of rolling elements is one of the most important topics of mechanical engineering. The lifetime of rolling systems is inversely proportional to the stresses within the contact surfaces. Gears, ball bearing, and roller bearing are some examples of the systems that their lifetime is related to the contact stresses.

As shown in Figure 1, there are two types of contact area between mating rolling surfaces under pre-pressed condition (zero loads):

1. Point contact: The contact between the two rolling solids initiate on a single point, e.g. ball bearings.
2. Line contact: Two solids initially touch along a straight or curved line, e.g. roller bearings.

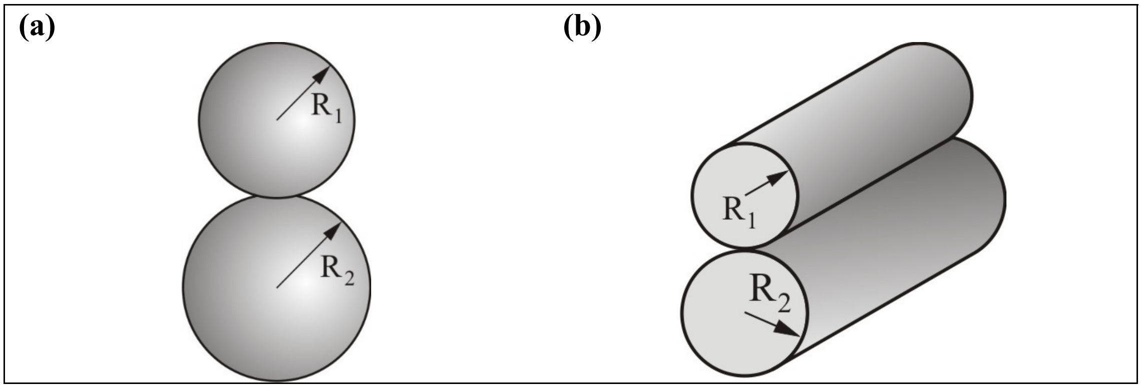

Figure 1.1 (a) Point contact between two spheres (b) Line contact between two cylinders

Before loading, the contact area is usually small in both principal directions (point contact condition), or at least in one direction (line contact). However, after applying the load, both types of contact areas change. As shown in Figure 1.2 the point contact expands to an elliptical area and the line contact expands to a rectangle.

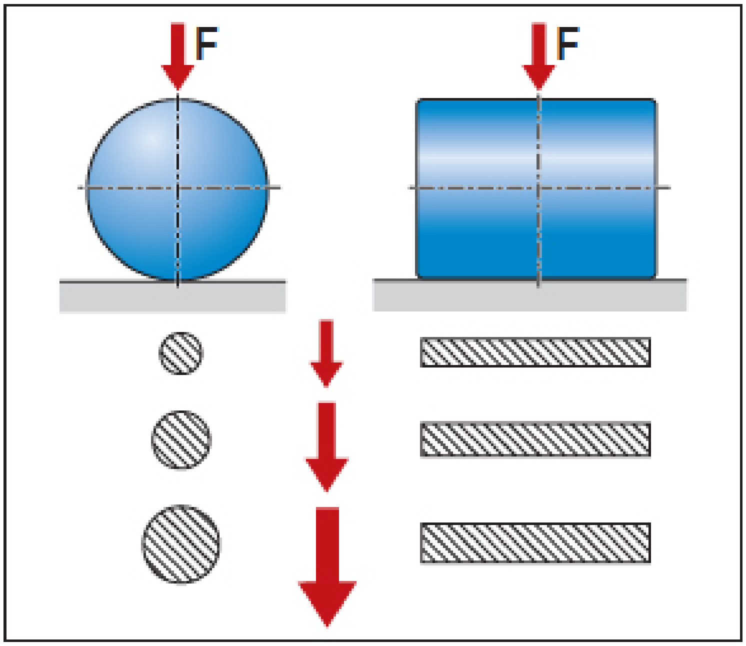

Figure 1.2 Contact area expansion during load application-Taken from (Collins, 2015)

The first analysis of elastic contact problems was presented by H. (Hertz, 1896). Many other researchers have tried to develop and extend his works to include more loading conditions. In this context, (Hartnett, 1980) presented a numerical procedure to solve the general dry contact problem.

The following describes the algorithm and procedure of Hartnett's solution. The results of a dry contact problem based on this method are presented. Hartnett considers a pair of three-dimensional nonconforming elastic bodies as the contact surfaces. A schematic of an elastic body contact problem is demonstrated in Figure 1.3.

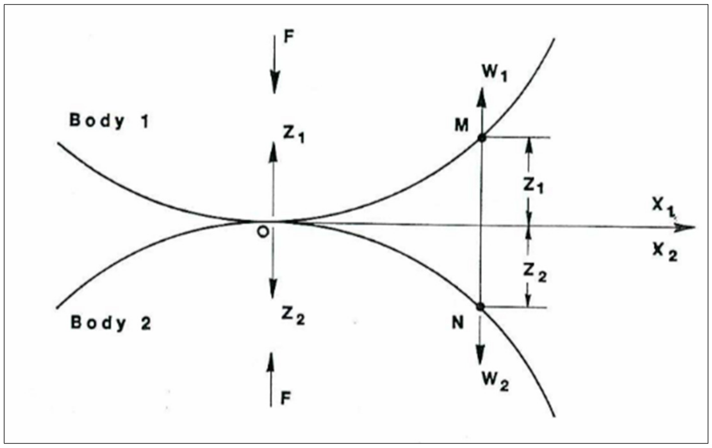

Figure 1.3 The contact of elastic bodies-Taken from (Hartnett, 1980)

For each object, an independent coordinate system is defined ($x_1y_1z_1$ and $x_2y_2z_2$), which have a common origin at the first point of contact. The rules governing the surface displacement is written as in equations (1.1) and (1.2).

$$w_1 + w_2 + z_1 + z_2 = \alpha' \quad \text{(inside the region of contact)} \tag{1.1}$$

$$w_1 + w_2 + z_1 + z_2 \geq \alpha' \quad \text{(outside the region of contact)} \tag{1.2}$$

Where z_1 and z_2 are the initial separations, of the bodies from the tangential plan, w_1 and w_2 represent the bodies' displacements and α' stands for the approach of body 1 toward body 2. While solving the equations, two conditions should be satisfied:

1. The pressure distribution in the contact area should result in a total force equal to the applied load.
2. There should be no negative pressure value in the contact zone.

Equations (1.3) and (1.4) formulate these two conditions.

$$\int_{\Omega} P(x', y')dx', dy' = F \tag{1.3}$$

$$P(x', y') \geq 0 \tag{1.4}$$

where P stands for the pressure, F is the applied load and (x', y') are the coordinates of a position on the contact plane. Eq. (1.3) is called the force balance equation and ensures the equilibrium over the solution domain **Ω**. In this numerical method, a combination of Boussinesq half-space force-displacement relations and a modified form of the flexibility method are employed. The Hartnett algorithm considers the contact zone as a half-space, and its surface is divided into a system of rectangular cells with piecewise constant contact pressures. Figure 1.4 depicts two arbitrarily shaped surfaces contacting over an area indicated by the shaded zone.

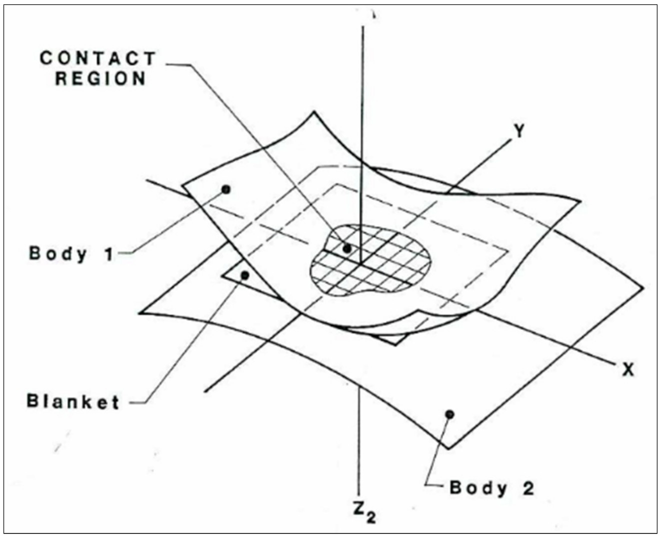

Figure 1.4 Contact of arbitrarily shaped indenters-
Taken from (Hartnett, 1980)

Solving the systems of linear algebraic equations provides the unknown pressure values. The governing equations are presented below.

$$w_{1_P} + w_{2_P} + z_{1_P} + z_{2_P} - \sum_{j=1}^{m} \sum_{k=1}^{n} \bar{P}_{kj} f_{kj,ip} (1 - \delta_{ik}) = \alpha' \tag{1.5}$$

The elastic deformation of the contact surfaces is $\delta\ (x, y)$.

$$\delta(x, y) = \frac{2}{\pi E'} \int \int \frac{p(x', y') dx' dy'}{\sqrt{(x - x')^2 + (y - y')^2}} \tag{1.6}$$

The discretized contact area into regular cells with uniform pressure results in the following format of the elastic deformation Eq. (1.7) (Najjari & Guilbault, 2014)

$$\delta(x,y) = \frac{2}{\pi E'} \sum_{k=1}^{n_x} \sum_{l=1}^{n_y} f_{ij,kl} p_{k,l} \tag{1.7}$$

$$\sum_{j=1}^{m} \bar{P}_{ij} f_{ij,ip} = \bar{D}_{ip} \tag{1.8}$$

$$\bar{D}_{ip} = \alpha' - z_{1_P} - z_{2_P} + \sum_{\mathrm{j}=1}^{m} \sum_{k=1}^{n} \bar{P}_{kj} f_{kj,ip} (1 - \delta_{ik}) \tag{1.9}$$

$$\bar{P}_{ij} \leq 0 \quad i = 1,2,\dots,n \;\; j = 1,2,\dots,n \tag{1.10}$$

where $\bar{P}$ is the constant pressure on a cell, f is the influence coefficient, and δ_{ik} is the Kronecker delta. Eq. (1.11) gives the influence coefficient.

$$\begin{aligned} f_{ij}(\bar{x},\bar{y}) = k\{(\bar{x}+b)\ln\left(\frac{(\bar{y}+a)+\sqrt{(\bar{y}+a)^2+(\bar{x}+b)^2}}{(\bar{y}-a)+\sqrt{(\bar{y}-a)^2+(\bar{x}+b)^2}}\right) \\ +(\bar{y}+a)\ln\left(\frac{(\bar{x}+b)+\sqrt{(\bar{y}+a)^2+(\bar{x}+b)^2}}{(\bar{x}-b)+\sqrt{(\bar{y}+a)^2+(\bar{x}-b)^2}}\right) \\ +(\bar{x}-b)\ln\left(\frac{(\bar{y}-a)+\sqrt{(\bar{y}-a)^2+(\bar{x}-b)^2}}{(\bar{y}+a)+\sqrt{(\bar{y}+a)^2+(\bar{x}-b)^2}}\right) \\ +(\bar{y}-a)\ln(\frac{(\bar{x}-b)+\sqrt{(\bar{y}-a)^2+(\bar{x}-b)^2}}{(\bar{x}+b)+\sqrt{(\bar{y}-a)^2+(\bar{x}+b)^2}})\} \end{aligned} \tag{1.11}$$

a and b represent the dimensions of the rectangular cell and $(\bar{x},\bar{y})$ are the local coordinate location of the center of cell j regarding the center of cell i, and k is defined as Eq. (1.12)

$$k = \frac{(1-{\nu_1}^2)}{\pi E_1} + \frac{(1-{\nu_2}^2)}{\pi E_2} \tag{1.12}$$

This method incorporates local and remote influence components. The local part is the displacement as the result of loading on the same cell, while the remote component is the displacement induced by the loading on the other cells. In this way, increasing the number of cells provides a proportional increase in the accuracy of the solution. Besides the pressure distribution, the procedure evaluates the contact area and approach of the two bodies.

1.3 Modeling

1.3.1 Dry Contact Problem

The contact area lays onto the plane tangent to the bodies at the initial point or line of contact. By attributing a Cartesian coordinate to this plane, the surface displacement of both bodies is referred to it. The surface is divided into a system of rectangular cells with constant pressure. The unknown pressure values can be determined by solving the system of linear algebraic equations. To initiate the numerical solution, the procedure guesses an initial contact area large enough to include completely the real contact area. (Figure 1.5)

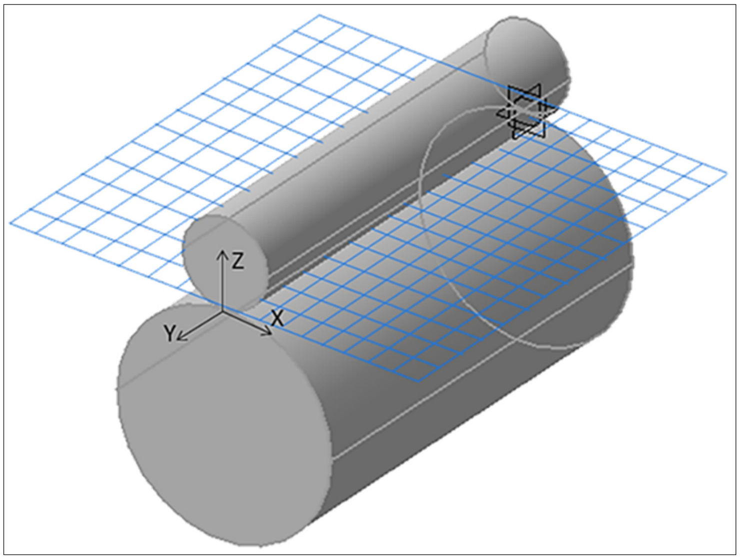

Figure 1.5 Numerical solution of dry contact problem

To illustrate the procedure, Figure 1.6 shows the pressure distribution in a contact problem, where two identical right circular cylinders are pressing each other by a contact force of 30 kN. The radius of each cylinder is 10 mm, and the axes of both cylinders are parallel. Table 1.1 shows the simulation parameters of dry contact model. In each cross-section, the maximum pressure occurs in the centerline of the contact area. The pressure values at the two longitudinal ends of the contact show visible rises. The next section discusses this effect.

Table 1.1 Dry contact simulation parameters

Elastic modulus (E)	200 Gpa	Rollers Radius ($R_1 = R_2$)	10 mm
Poisson's ratio (ν)	0.3	Equivalent radius of the rollers (R)	5 mm
Contact force (F)	30 kN	Rollers Length (L)	4 mm

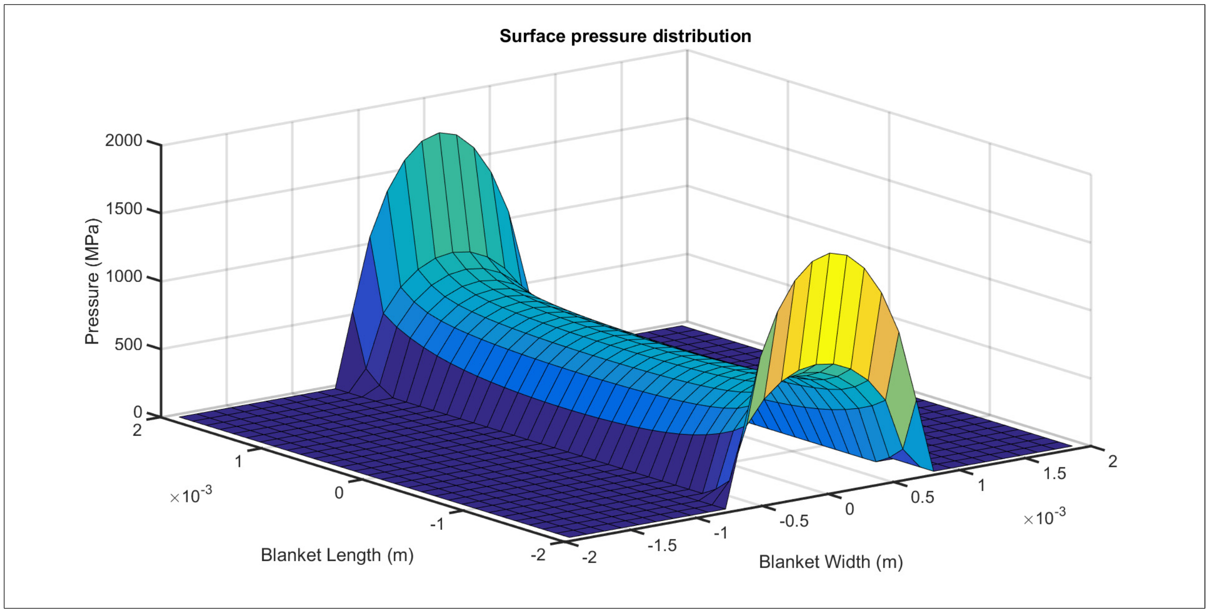

Figure 1.6 Surface Pressure Distribution-right circular cylinder

1.3.2 Mirroring Process

Figure 1.6 depicts high-stress concentrations at the edges of the contact area. This numerical phenomenon results from the finite dimensions of the contact bodies. In reality, the free surfaces at the cylinder ends should cause a pressure decrease close to the free edges. The Hartnett algorithm considers both solid bodies as half-space (de Mul, Kalker, & Fredriksson, 1986). The half-space theory introduces artificial shear and normal stress distributions on the free surfaces. These stresses increase the rigidity of the cylinder close to their limits. The half-space theory correlates the displacement to the surface tractions (Eqs. (1.7) and (1.9)). The pressure overestimation at the free edges also has a significant effect on the displacement field. To overcome this problem and eliminate the free-boundary artificial shear and normal stress distributions, some correction approaches should be considered. Elimination of normal stress requires computational effort. (de Mul et al., 1986) noted that the shear stress influence is dominant on the surface displacement compared to the normal component. They, therefore, proposed to eliminate the shear contribution.

Mirroring the pressure distribution field regarding the end planes can remove the shear stresses. Repeating this procedure on both sides of the object removes the shear stresses and, therefore, a finite-length solution is achieved. The mirroring process solely removes the shear stresses from the free surfaces. Also, this process doubles the normal stresses at the end planes. The mirroring process can be repeated two or three times until sufficient accuracy is achieved. Figure 1.7 and Figure 1.8 depict the first and the second steps of the mirroring process applied to the contact problem shown in Figure 1.6. The stress concentration at the edges is largely eliminated. Repeating the mirroring process for one more time leads to a minor reduction of the edge stress.

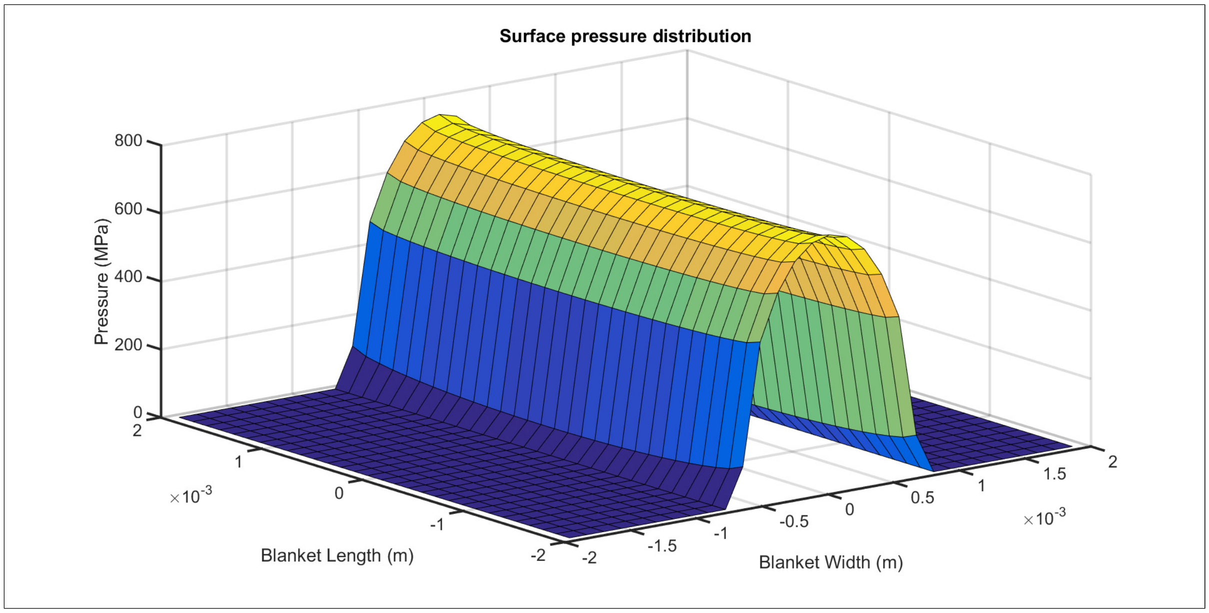

Figure 1.7 Surface Pressure Distribution-right circular cylinder - 1st step mirroring process

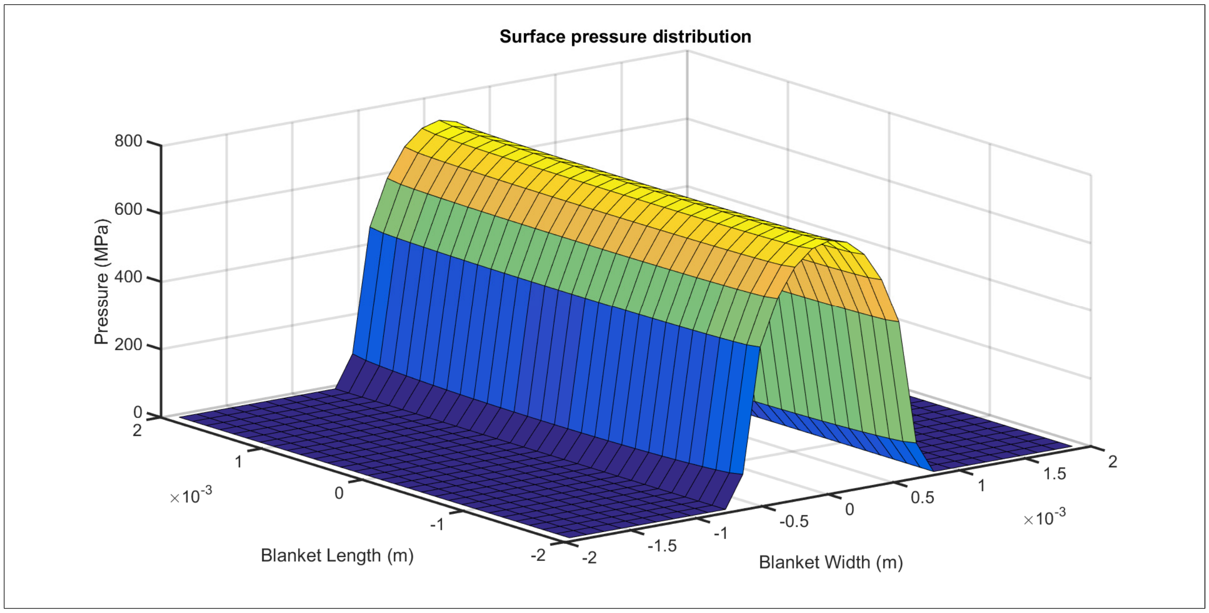

Figure 1.8 Surface Pressure Distribution-right circular cylinder - 2nd step mirroring process

1.3.3 Correction Factor

The previous section mentioned that the mirroring process could not remove the normal stresses acting on the free surfaces. (Guilbault, 2011) proposed a correction factor to modify the shear correction procedure to eliminate the normal stresses' influence on the displacements. To this end, the pressure value of each mirror cell should be multiplied by the Guilbault's correction factor given by Eq. (1.13), where P and P* are the initial and the mirror corrected pressures, respectively, and ν is the Poisson coefficient. Figure 1.9 Illustrates the quarter-plane free boundary correction operation.

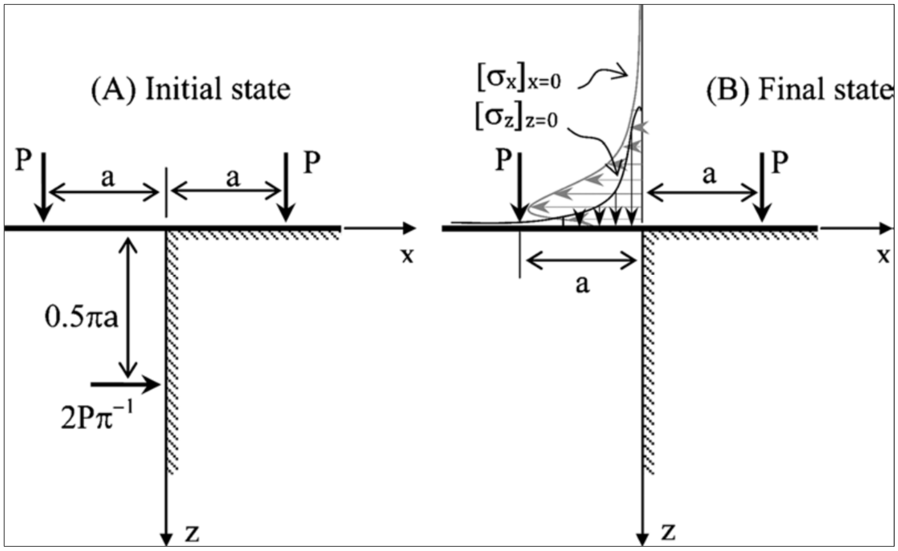

Figure 1.9 Correction process of quarter-plane free boundary-Taken from (Guilbault, 2011)

$$\psi = \frac{P^*}{P} = 1.29 - \frac{1}{(1-\nu)}[0.08 - 0.5\nu] \tag{1.13}$$

Applying this method results in a more accurate estimation and causes no modification of the calculation time. Figure 1.10 shows the influence of the correction factor on the previous contact problem. The plot in Figure 1.10 shows a more realistic distribution, where the contact pressure close to the contact ends shows slight decreases, caused the rigidity reduction associated with the free surfaces.

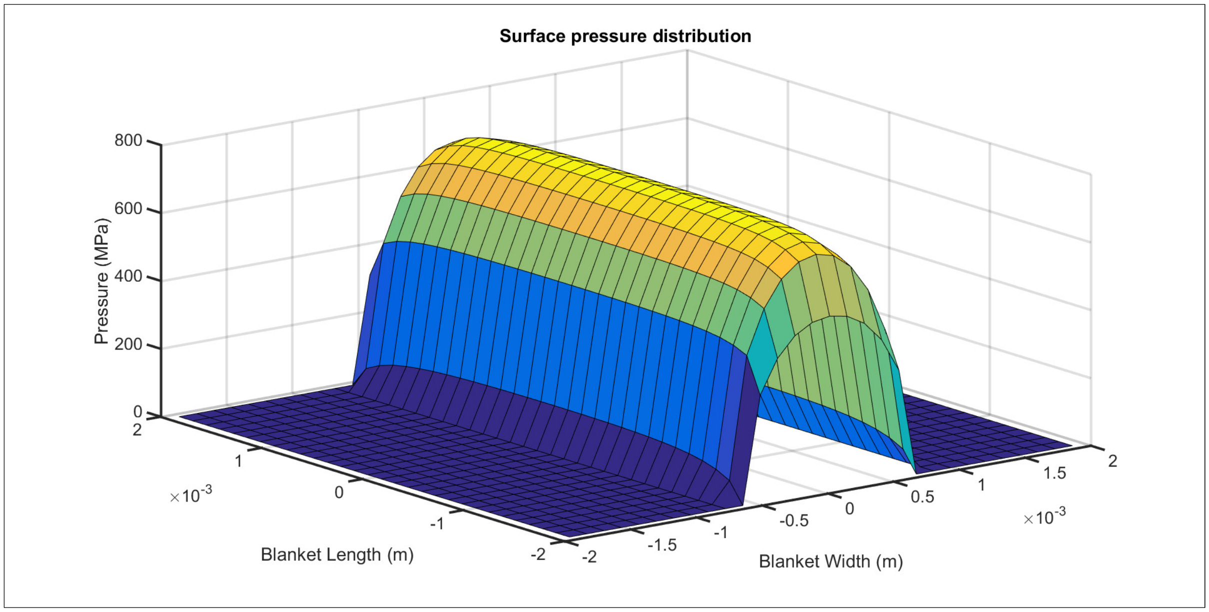

Figure 1.10 Surface Pressure Distribution-right circular cylinder-1st step mirroring process-Effect of the correction factor

Figure 1.11 compares the pressure distributions resulting from the different correction stages. Although the first mirroring step modifies the pressure distribution, increasing the mirroring steps does not have a remarkable effect. On the other hand, applying the correction factor (Eq. ((1.13)) demonstrates a significant influence.

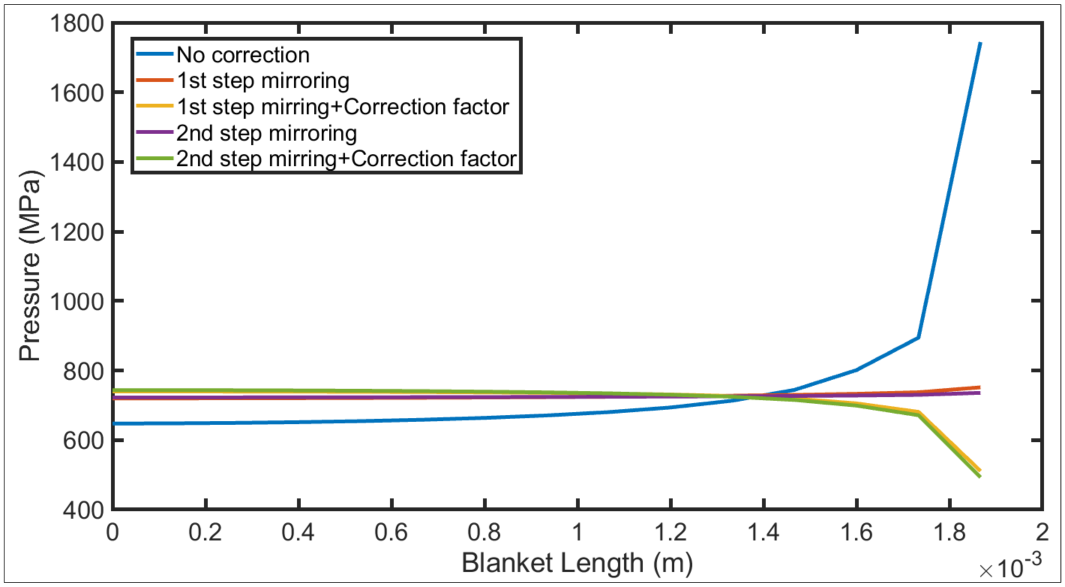

Figure 1.11 Comparison between different modification methods of pressure distribution correction

1.3.4 Misalignment

An ideal loading condition is defined when there is no misalignment between the bodies' axes. However, the bodies in contact are often subject to a different combination of forces and moments. In practical applications, axial misalignment is common. The mating cylinders may have various types of configurations. Different lengths, tilt, and angularly displacements are examples of cylindrical contact conditions (Figure 1.12). In this context, (Park, 2010) showed that small misalignments have considerable effects on the pressure distributions leading to asymmetric distributions. (Kushwaha, Rahnejat, & Gohar, 2002) studied the misalignment conditions and their influences on the contact between rollers and raceways.

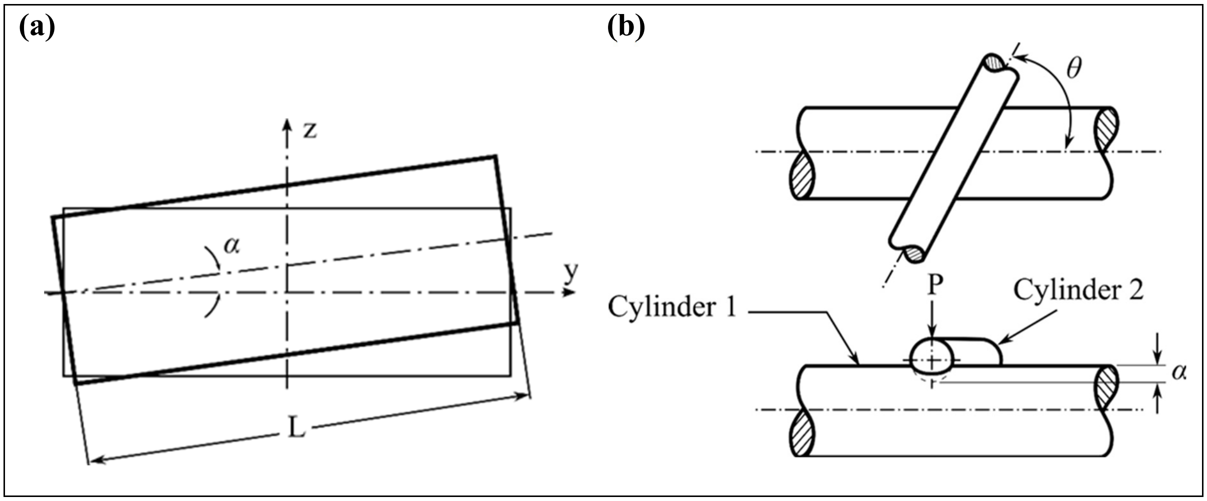

Figure 1.12 Two types of misalignments (a) Perpendicular to the contact plane, (b) In contact plane

Figure 1.13 displays the pressure distribution calculated for the previous contact problem with 0.05 rad angular misalignment perpendicular to the contact plane (condition (a) in Figure 1.11) when neglecting ψ (Eq.(1.13)). The pressure profile is highly influenced by a tiny tilting condition producing an asymmetric pressure distribution. Applying the Guilbault's factor to this misalignment problem modifies the pressure distribution at the traction-free edge (Figure 1.14).

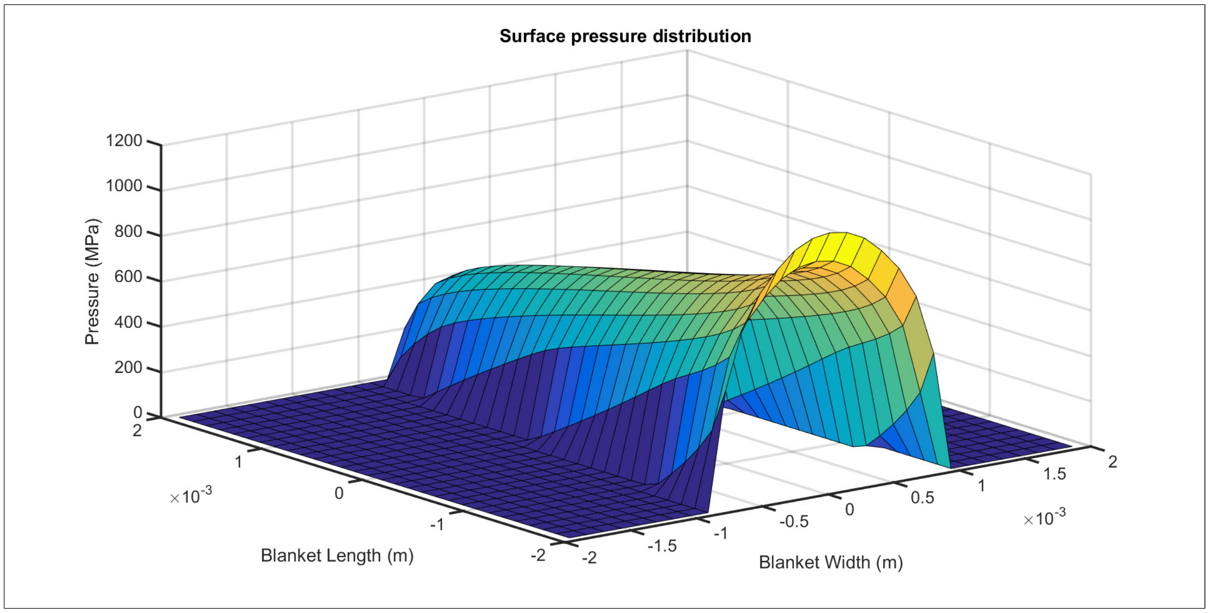

Figure 1.13 Surface Pressure Distribution-right circular cylinder-1st step mirroring process -0.05 radians misalignment

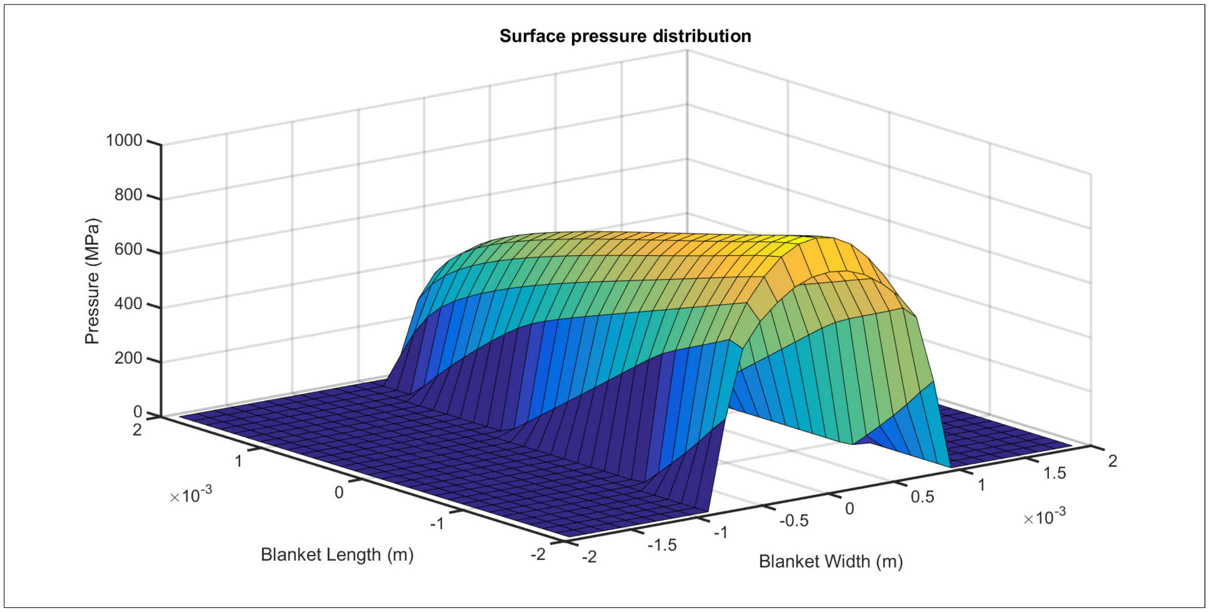

Figure 1.14 Surface Pressure Distribution-right circular cylinder-1st step mirroring process and correction factor- 0.05 radians misalignment

The pressure distribution related to contact of two cylinders with axes misalignment in contact plane (condition (b) in Figure 1.12) is shown in Figure 1.15 (a). The calculation included Guilbault's factor (Eq.(1.13)). Figure 1.15 (b) shows the top view of the contact area.

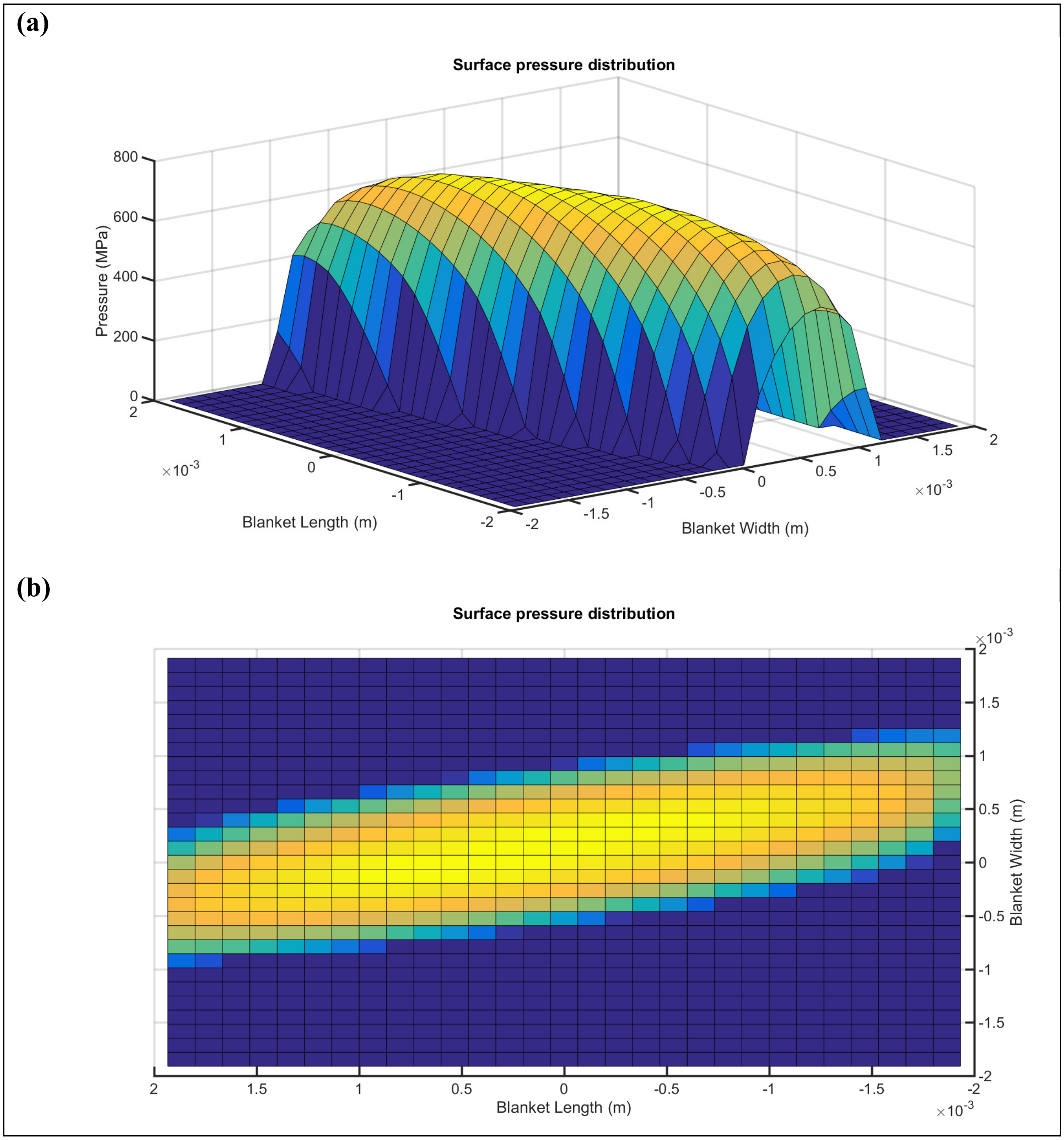

Figure 1.15 Surface Pressure Distribution-right circular cylinder-1st step mirroring process and correction factor - 0.5 radians in-plane misalignment (a) Symmetric view, (b) Top view

Figure 1.16 and Figure 1.17 show the pressure distribution for the contact of two cylinders with different radii. In these cases, the axes of both cylinders are parallel, and the radii of the cylinders are 10 mm and 20 mm. Since larger radii increase the contact area, the pressure values decrease compared to the previous case. The results in Figure 1.16 only include the first step of the mirroring process and neglect the ψ factor. On the other hand, Figure 1.17 shows the pressure distribution when applying the Guilbault's correction factor.

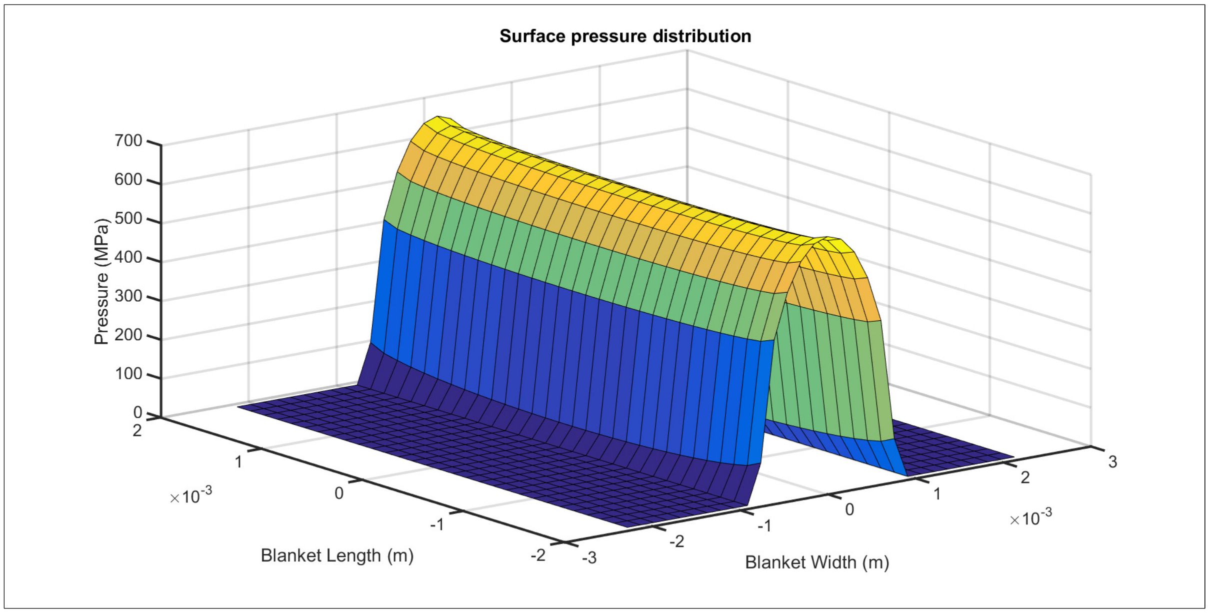

Figure 1.16 Surface Pressure Distribution-right circular cylinder-1st step mirroring process - effect of different radii

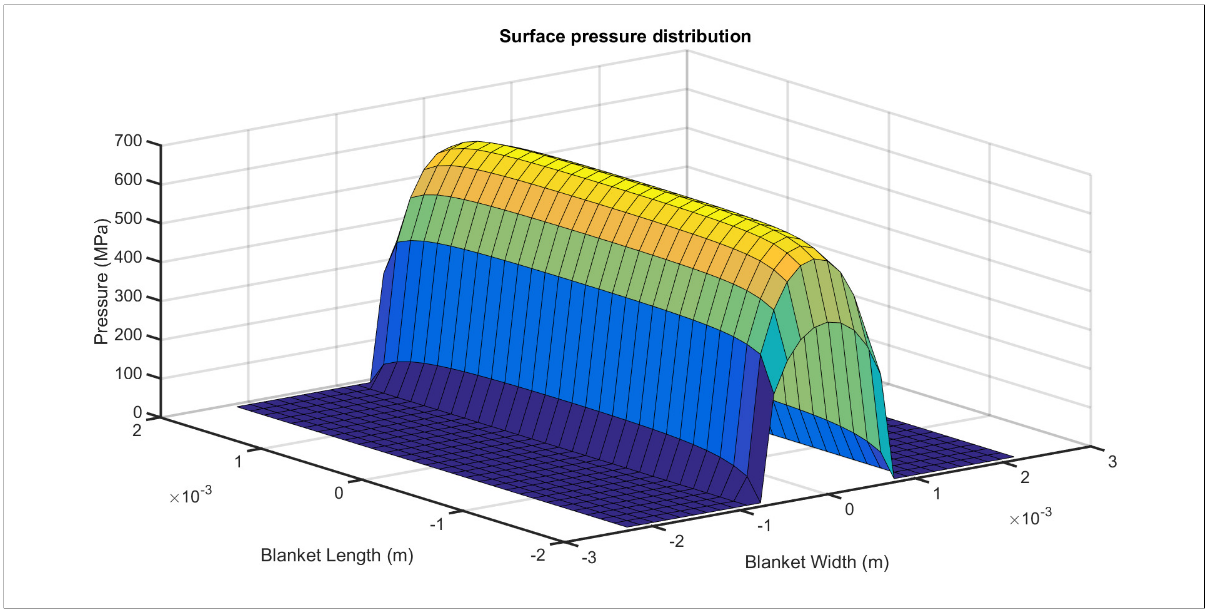

Figure 1.17 Surface Pressure Distribution-right circular cylinder-1st step mirroring process and correction factor - effect of different radii

1.4 Conclusion

This chapter showed that numerical methods based on the classic half-space theory are unable to predict the pressure profile of contact areas limited by free surfaces. Rollers of finite length belong to this group. The presented results also demonstrated that applying several steps of mirroring to eliminate the shear stress distribution generated on the free surfaces cannot fully solve this issue. On the other hand, adding the correction factor given by Eq.(1.13) provides precise 3D evaluations of pressure distributions generated between bodies of finite length. While presenting various test cases, this chapter does not include a systematic validation of the dry contact model, since the modeling approach was already fully validated in the reference paper (Guilbault, 2011). Dry contact pressure distributions will be used as the initial values for the EHL solution. The presented model will also establish the elastic deformations of the bodies during EHL simulations.

CHAPTER 2

EHL MODELING

2.1 Introduction

This chapter presents the EHL model prepared to predict lubricant film thicknesses generated between smooth surfaces. It provides the equations for evaluation of lubricant density and viscosity changes caused by pressure variations in lubricant film thickness generated under EHL conditions. The EHL model presented hereafter combines the Hartnett algorithm considering the correction factors discussed in chapter 1 to a finite-difference solution of the 3D Reynolds equation. The modeling strategy described in the following pages is entirely based on the model developed in (Najjari & Guilbault, 2014).

2.2 Reynolds Equation

The governing equations in fluid dynamics (Navier-Stokes and continuity equations) and elasticity equations should be combined to build up a numerical simulation for tribology problems. Accordingly, the Reynolds equation is derived from the 2D Navier-Stokes equation. This formulation includes the following hypotheses:

- The lubricant flow is laminar.
- There are no body forces.
- The film thickness is small compared to the dimensions of the contact.
- The lubricant is considered Newtonian with constant density and viscosity across the film thickness.
- A no-slip boundary condition is considered between the lubricant and the surfaces.
- The lubricant and the rotating bodies are in isothermal conditions.

Regarding the last assumption, note that the temperature change does not have a significant effect on the pressure and film thickness distributions, specifically when the bodies are rolling rather than sliding (Y. Liu, 2013). The most important effect of temperature is on the friction coefficient that will be discussed in the next chapter.

A pair of three-dimensional mating solid surfaces with surface velocities of $u_1$and u_2 in the flow direction should be considered. Since the film thickness is assumed to be thin, all derivatives regarding x and y directions are significantly smaller than their equivalents regarding the z-direction. As a result, those smaller terms can be removed to reduce the simulation cost. The Reynolds equation is derived by combining the 2D Navier-Stokes equations to the continuity equation. When neglecting the time derivative component, the Reynolds equation reduces to Eq.(2.1): (Najjari & Guilbault, 2014). Where p represents the pressure, η stands for the viscosity, ρ represents the density and $u_e = \frac{(u_2+u_1)}{2}$ is the velocity.

$$\frac{\partial}{\partial x}\left(\frac{\rho h^3}{\eta}\frac{\partial p}{\partial x}\right)+\frac{\partial}{\partial y}\left(\frac{\rho h^3}{\eta}\frac{\partial p}{\partial y}\right)=12u_e\frac{\partial(\rho h)}{\partial x} \qquad (2.1)$$

The Reynolds equation provides pressure distribution throughout the film thickness. The left side terms of this equation are known as “Poiseuille terms” and the right side is called as “Couette term”. Eq. (2.1) is the 3D Reynolds equation. Since we want to simulate the 3D pits and the effect of rollers’ edges, the Reynolds equation in 3D format is used throughout the modeling without any simplification to 2D equation.

It should be mentioned that in the derivation of the above equation the lower surface z_1 is chosen as the reference point. The boundary conditions are implemented as follows:

$$U = U_1 \quad @\, z = z_1$$
$$U = U_2 \quad @\, z = z_2$$

And the velocity profile is expressed as: (Shirzadegan, 2016)

$$u = \frac{1}{2\eta}\frac{\partial p}{\partial x}(z^2 - hz) + \frac{(u_2 - u_1)}{h}(z) + u_1 \qquad (2.2)$$

The velocity equation consists of two terms: the Poiseuille term which has a parabolic profile and the Couette term with a linear profile.

2.3 Film Thickness

The film thickness equation is given in Eq. (2.3) (Ghosh, 1985)

$$h(x,y) = h_0 + g(x,y) + \delta(x,y) \tag{2.3}$$

where h_0 is a constant corresponding to the minimal separation of the two surfaces, $g(x,y)$ is the initial separation due to the geometry of the undeformed solids, and $\delta(x,y)$ represents the elastic deformation of the rolling surfaces (calculated with the contact model introduced in Chapter 1). The initial separation of undeformed solids can be written as (Shirzadegan, 2016)

$$g(x,y) = \frac{x^2}{2R_x} + \frac{y^2}{2R_y} \tag{2.4}$$

Where R_x and R_y are the reduced radius of curvature in x and y directions depicted in Figure 2.1. (Ghosh, 1985)

$$\frac{1}{R_x} = \frac{1}{R_{1x}} + \frac{1}{R_{2x}} \tag{2.5}$$

$$\frac{1}{R_y} = \frac{1}{R_{1y}} + \frac{1}{R_{2y}} \tag{2.6}$$

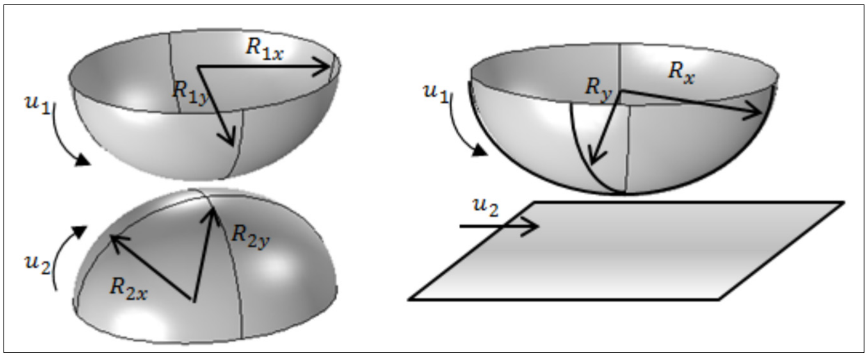

Figure 2.1 Equivalent contact for the point contact problem - Taken from (Shirzadegan, 2016)

In the case of two aligned rollers in line contact problems, the initial separation reduces to cylindrical-plane contact conditions equivalent to parabolic separations as given below. (Shirzadegan, 2016)

$$g(x, y) = \frac{x^2}{2R} \tag{2.7}$$

$$\frac{1}{R} = \frac{1}{R_1} + \frac{1}{R_2} \tag{2.8}$$

R represents the reduced curvature radius (Figure 2.2).

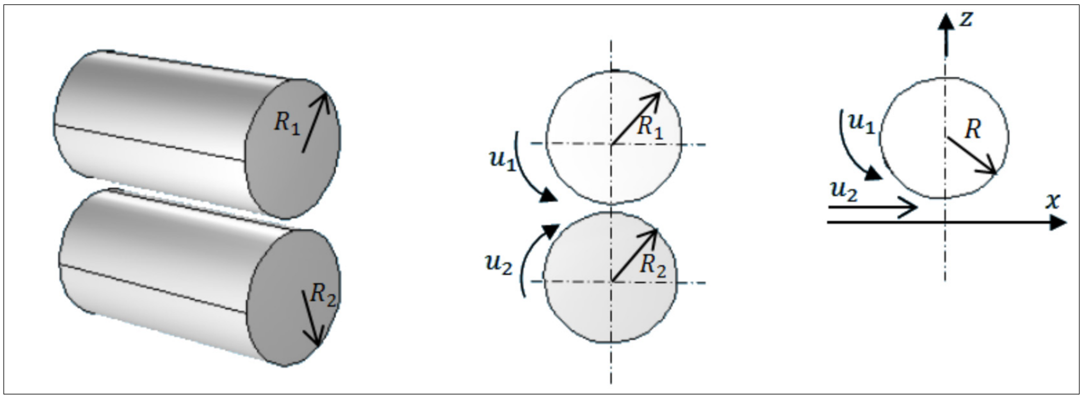

Figure 2.2 Equivalent contact for the line contact problem-Taken from (Shirzadegan, 2016)

The elastic deformation of the rolling surfaces $\delta(x,y)$ is established from the elastic model developed in Chapter 1 for the dry contact conditions.

2.4 Lubricant Properties

Because of the very high pressures involved in EHL contacts, to model those conditions with precision, the compressibility and piezo-viscosity responses of the lubricant should be included in the process.

2.4.1 Lubricant density

Under EHL contact conditions, the lubricant density demonstrates a nonlinear relation with pressure and temperature. A pressure rise causes an increase in the lubricant density. Different expressions formulating the pressure-density were published over the years. The Dowson and Higginson equation is among the most frequently used relations. It includes both the pressure and temperature influence on the lubricant density (Eq. (2.9) below) (Najjari & Guilbault, 2014).

$$\rho(p,T) = \rho_0[1 + \frac{0.59 \times 10^{-9} p}{1 + 1.17 \times 10^{-9} p}](1 - \beta(T - T_0)) \tag{2.9}$$

where $\beta, T, T_0, \rho, \rho_0$ are the density-temperature coefficient, temperature, ambient temperature, density, and density at ambient temperature, respectively. For constant temperatures, the equation becomes (Shirzadegan, 2016)

$$\rho(p) = \rho_0[\frac{0.59 \times 10^9 + 1.34 \times p}{0.59 \times 10^9 + p}] \tag{2.10}$$

2.4.2 Lubricant viscosity

The lubricant viscosity highly depends on pressure and temperature. In EHL contact, the lubricant undergoes intense loading. Therefore, compared to a no-load condition its viscosity may increase several orders of magnitude. This increase in viscosity allows generating lubricant layers sufficiently thick to prevent solid-to-solid contacts and reduce friction and wear. Several models have been proposed to describe the relationship between viscosity, pressure, and temperature. The pressure-viscosity-temperature relation presented by Roelands is probably more accurate. The relation is expressed as (Shirzadegan, 2016)

$$\eta(p,T) = \eta_0 \exp\{(\ln(\eta_0) + 9.67)[-1 + (1 + 5.1 \times 10^{-9}\mathrm{p})^{z_0}(\frac{T-138}{T_0-138})^{-S_0}]\} \tag{2.11}$$

$$z_0 = \frac{\alpha}{5.1 \times 10^{-9}(\ln(\eta_0) + 9.67)}$$

$$S_0 = \frac{\beta(T_0 - 138)}{\ln(\eta_0) + 9.67}$$

2.4.3 Carreau expression

Besides pressure and temperature, shear rates also significantly affect the lubricant viscosity. The relation between the shear stress, viscosity, and shear rate in Newtonian lubricant film can be written as (Shirzadegan, 2016)

$$\tau = \eta\dot{\gamma} \tag{2.12}$$

Furthermore, lubricants exhibit a limiting shear stress τ_l, over this critical stress, the lubricant shears at a constant stress. The limiting shear stress is linearly proportional to the pressure as written in Eq. (2.14) (Shirzadegan, 2016)

$$\tau = \begin{cases} \eta\dot{\gamma} & \tau < \tau_l \\ \tau_l & \tau > \tau_l \end{cases} \tag{2.13}$$

$$\tau_l = \Lambda p \tag{2.14}$$

where Λ is the limiting shear stress-pressure coefficient, which has a value of around 0.04-0.08. The rheological model of a non-Newtonian lubricant is thus obtained by implementing Eq. (2.14) into the Carreau expression as shown by Eq. (2.15) (Guilbault, 2013)

$$\eta = \min\left[\eta_1\left[1+\left(\frac{\eta_1}{G_f}\dot{\gamma}\right)^2\right]^{\frac{(n-1)}{2}}, \frac{\tau_l}{\dot{\gamma}}\right] \tag{2.15}$$

2.5 Numerical Simulation

To obtain an appropriate model for the EHL problem, several aspects should be considered. The elastic deformations of rolling surfaces, discretization of lubricant physical model, and finding a proper solution method are the critical steps in deriving the solution. The Reynolds equation is a nonlinear partial differential equation. Moreover, under EHL conditions this relation is coupled with viscosity changes defined by Eqs (2.9), (2.11), and (2.15). As a consequence, it takes some effort to find a stable solution. Actually, to find the pressure distribution and film thickness a system of equations composed of Eq. (2.3), the Reynolds equation, and the force balance must be solved simultaneously.

In this work, the governing equations were discretized along the lubricant film, and a recursive finite difference approach was employed to solve the coupled system of equations. Figure 2.3 presents a flowchart of the algorithm of the numerical solution.

Briefly, the dry contact solution is taken as the initial value for the pressure distribution and h_0 the minimum film thickness is guessed before entering the first loop. Based on these initial values, the material properties of the lubricant are calculated. The discretized Reynolds equation is then solved for the new set of pressures. In the internal loop, by using the newly calculated pressure set, the surface deformation, film thickness, and lubricant properties are updated. The internal loop should be repeated until the desired accuracy for the pressures is reached. The external loop is dedicated to checking the load balance. As mentioned before, the integration of the pressure value for all the cells in the contact zone should satisfy the equilibrium equation. By adjusting the value for h_0, one can simply change the load balance conditions. Once both conditions, pressure convergence, and the load balance, were met, the solution is finalized. The numerical modeling and solution were coded in C++. The error limits for pressure distribution and load balance were set to 10^{-4}, and the iteration loops were repeated until the calculated parameters falls below the limit of error. The duration of solution procedure was about 1 hour, depending on the total number of cells.

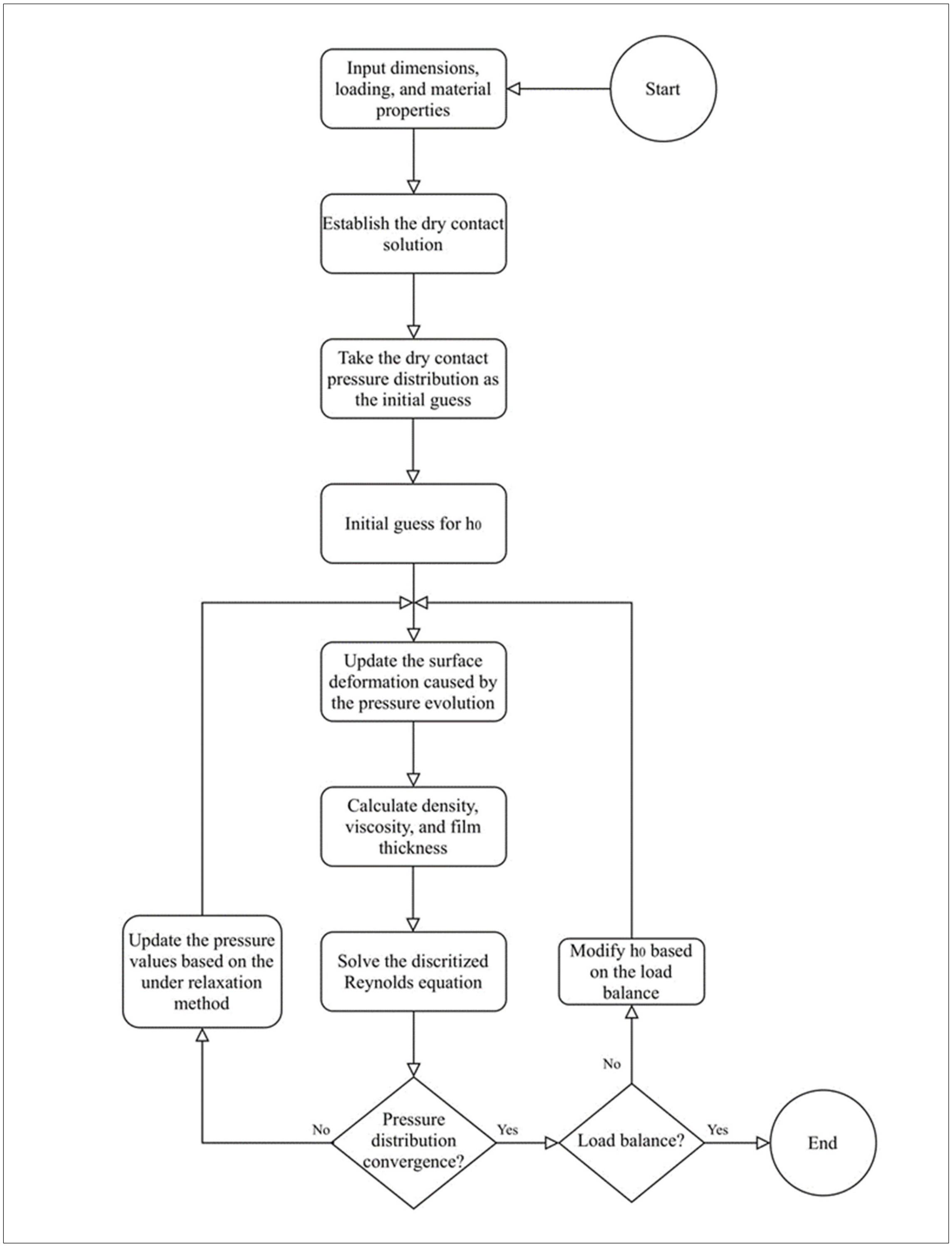
Start
Input dimensions, loading, and material properties
Establish the dry contact solution
Take the dry contact pressure distribution as the initial guess
Initial guess for h0
Update the surface deformation caused by the pressure evolution
Calculate density, viscosity, and film thickness
Solve the discritized Reynolds equation
Update the pressure values based on the under relaxation method
Modify h0 based on the load balance
No
Pressure distribution convergence?
Yes
Load balance?
No
Yes
End

Figure 2.3 Flowchart of the numerical solution

Figure 2.4 presents a 3D visualization of the surface pressure distribution describing the EHL solution obtained for two identical cylindrical rollers of radius 60 mm and parallel axes submitted to an external force of 6000 N and the average entrainment rolling speed of $u_e = 2.7\ \mathrm{m/s}$. The calculation includes one mirror level and the ψ factor to release completely the free surfaces at the roller ends. The visible EHL pressure rises close to the cylinder ends assure the mass continuity (in the axial direction) intrinsic to the Reynolds equation (Greenwood & Morales-Espejel, 1995).

To offer a better illustration and compare the results, Figure 2.5 juxtaposes the pressure distributions calculated along the flow direction at the axial central position (pressure cells in the center of the contact area) for both the dry contact and the EHL conditions. The EHL contact region extends toward the input region. The spike in the pressure distribution curve of the EHL maintains the mass continuity (in the flow direction) intrinsic to the Reynolds equation (Greenwood & Morales-Espejel, 1995). The film thickness slope also changes near the point that the spike occurs.

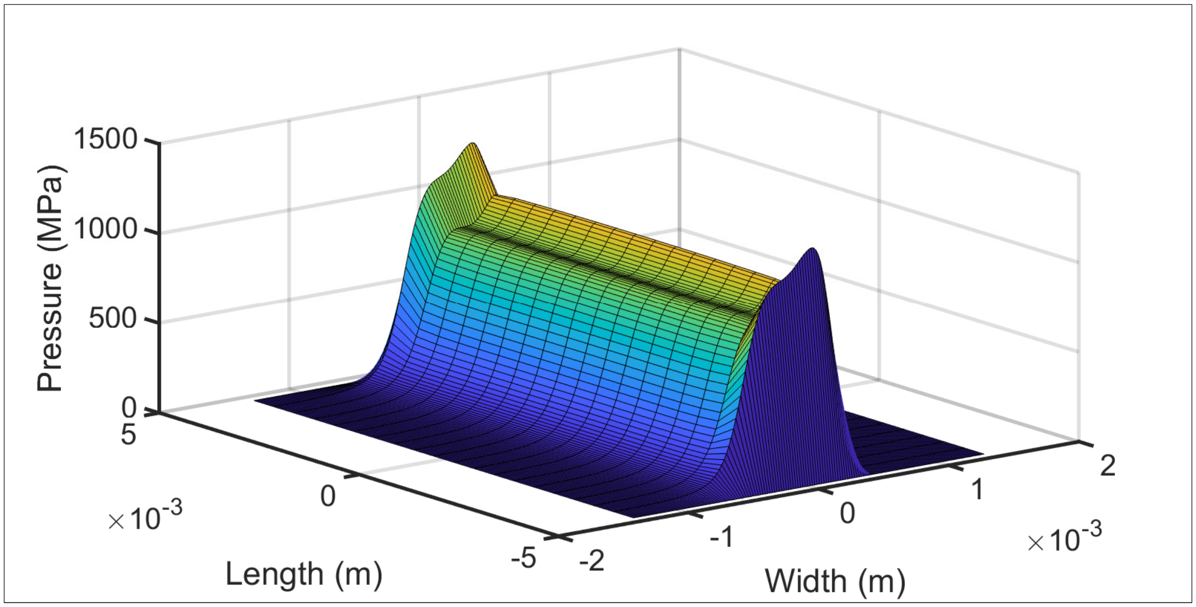

Figure 2.4 EHL pressure distribution ($\mathrm{F} = 6000\ \mathrm{N}$, $\mathrm{u_e} = 2.7\ \mathrm{m/s}$)

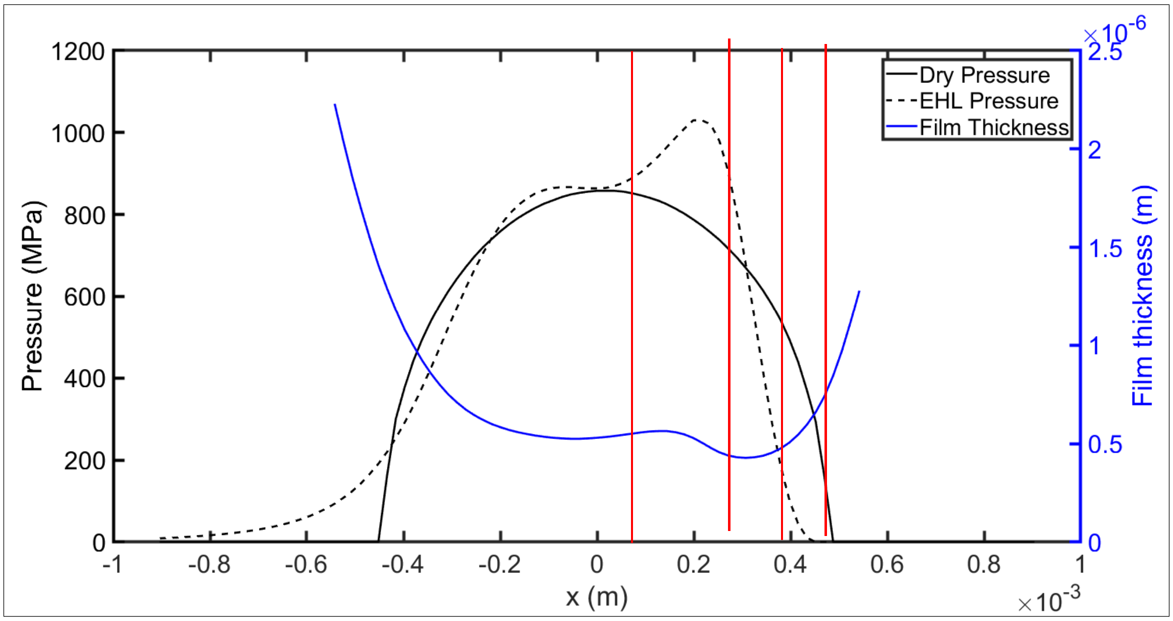

Figure 2.5 Comparison between dry contact and EHL solution along with the film thickness ($\mathrm{F} = 6000\ \mathrm{N}$, $\mathrm{u_e} = 2.7\ \mathrm{m/s}$)

To illustrate the effect of external loading on the pressure profile, the problem was modeled using different external forces. As shown in Figure 2.6, the pressure profile for lower forces is more uniform and the spike amplitudes are noticeably smaller. As the force increases, the irregularities in the shape of the pressure profile become more visible. (Elcoate, Evans, & Hughes, 1998) have also reported that when the loading is low, the pressure spike is not visible, and increasing the load generates the spikes. They showed that for very high loadings the spikes become smaller, and in the case of very heavy loadings the simulation gets unstable. The forces that we studied here are almost low loadings (between case 1 and case 2 of (Elcoate et al., 1998), and therefore, the trend is like their case studies. Figure 2.7 depicts the effect of rolling speed, u_e, on the pressure distribution. Increasing the value of u_e attenuates the spikes in the pressure profile. This trend is in good agreement with the previously reported results (Wolff, Nonaka, Kubo, & Matsuo, 1992).

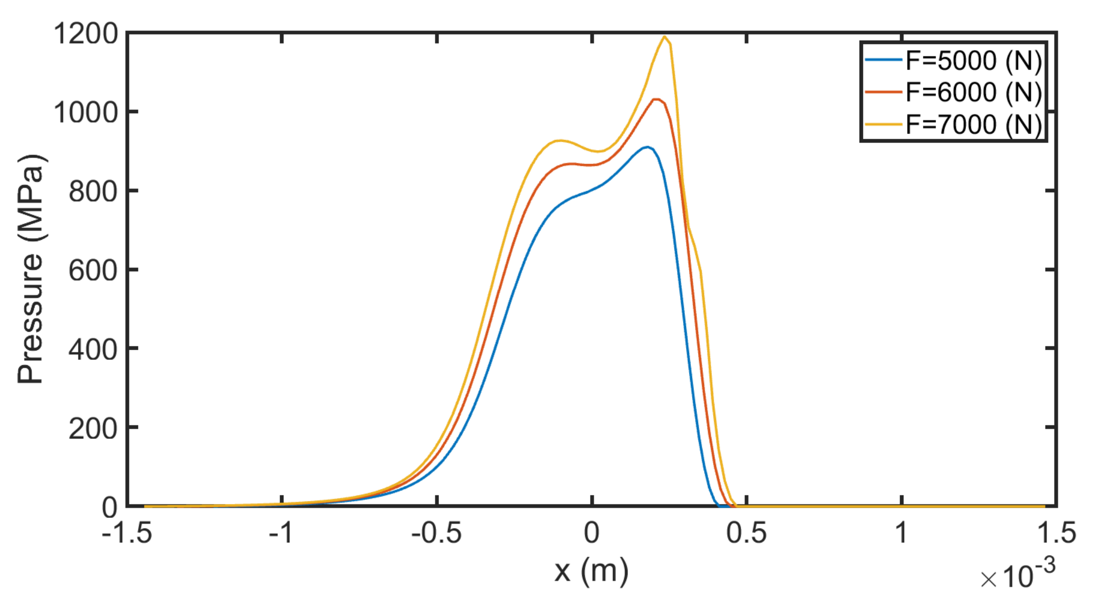

Figure 2.6 Pressure distribution at the midplane of EHL contact for different loads ($u_e = 2.7$ m/s)

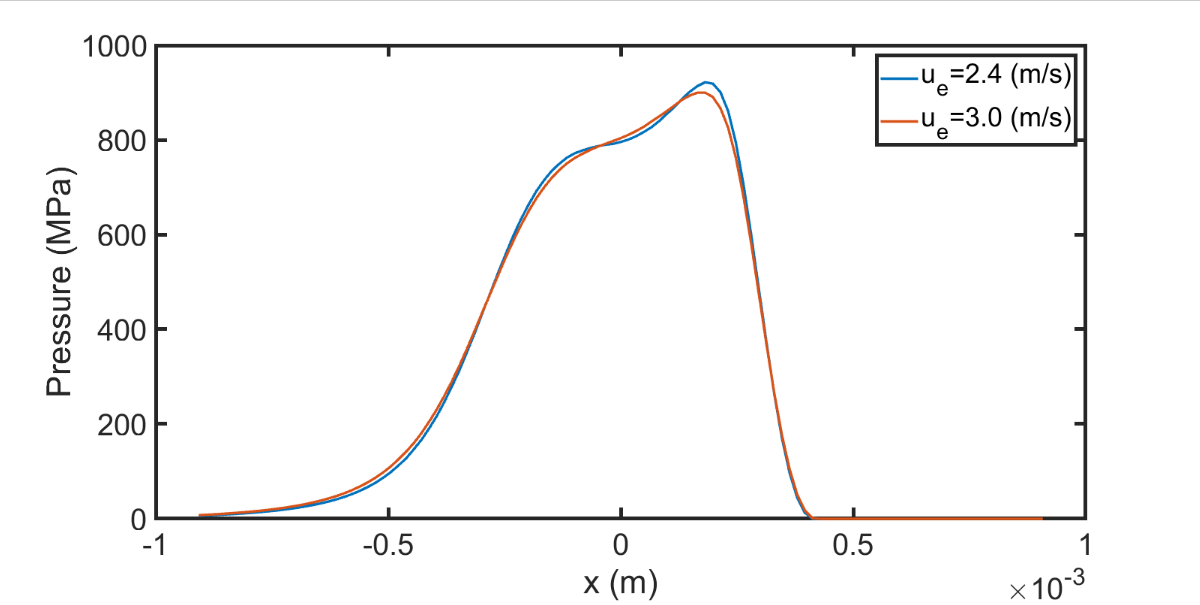

Figure 2.7 Pressure distribution at the midplane of EHL contact for different rolling speeds ($F = 5000$ N)

The most important parameter in EHL modeling is the lubricant film thickness. Figure 2.8 shows the lubricant film thickness profile. Figure 2.9 and Figure 2.10 show the effect of the external force and the relative rolling speed, respectively. As expected, increasing the external force causes a reduction of the lubricant film thickness; the bodies get closer to each other. On the other hand, augmenting the rolling speed increases the lubricant film thickness. Even if these results cannot be generalized, they indicate that the considered rolling speed increase has a more significant influence on the film thickness than the considered external force increase.

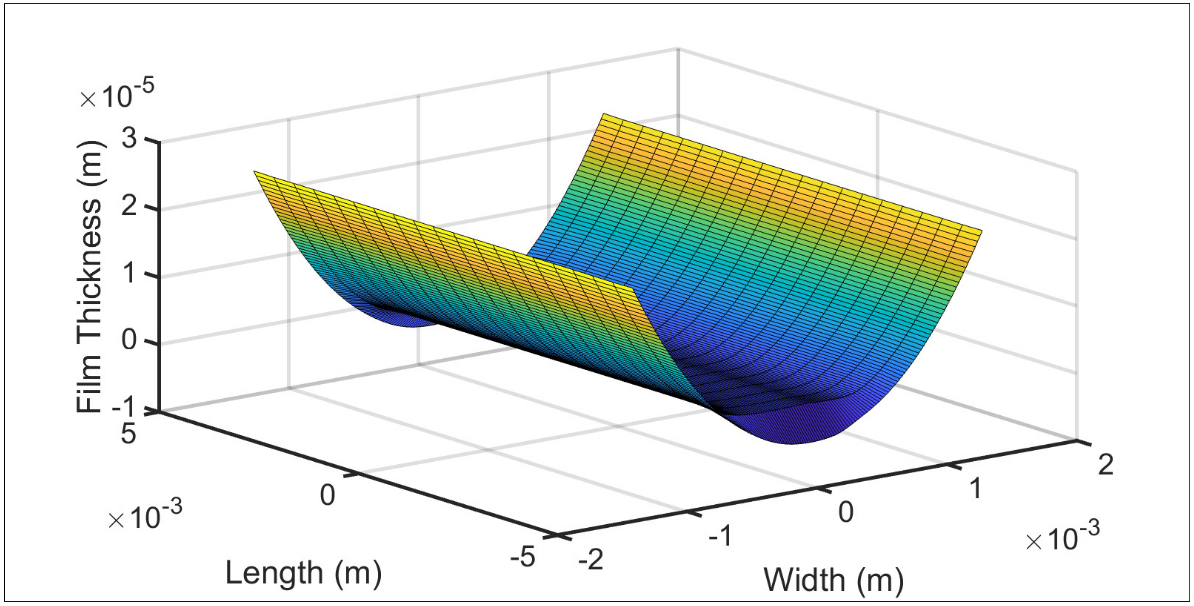

Figure 2.8 Lubricant film thickness ($F = 6000$ N, $u_e = 2.7$ m/s)

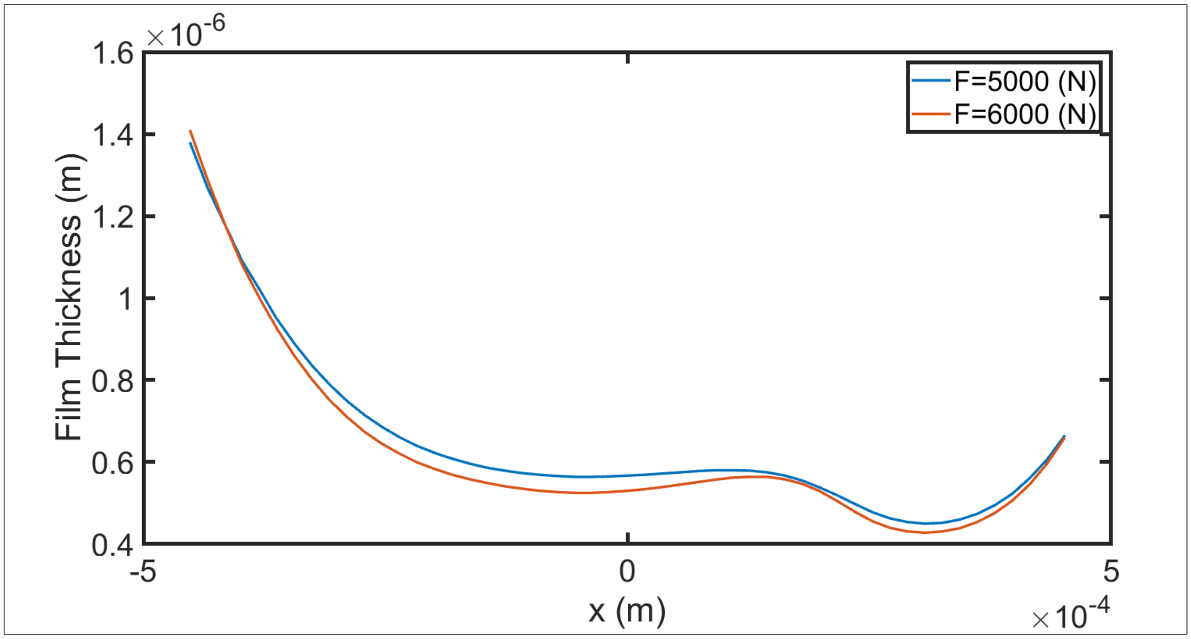

Figure 2.9 Film thickness at the midplane of EHL contact for different loads ($u_e = 2.7\ m/s$)

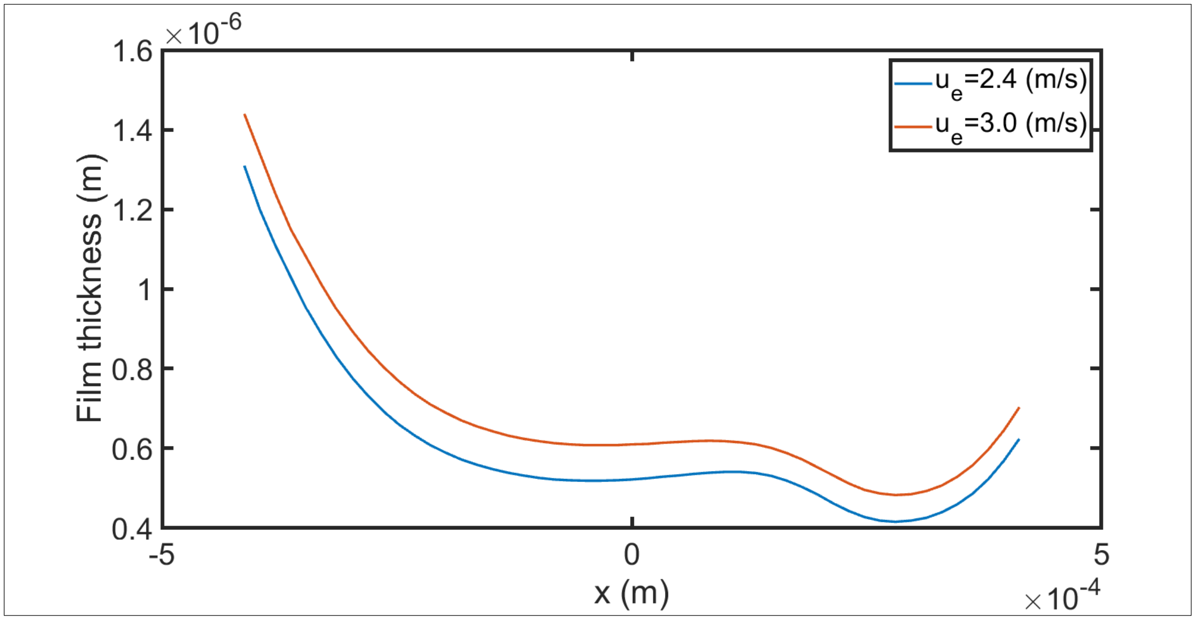

Figure 2.10 Film thickness at the midplane of EHL contact for different rolling speeds ($F = 5000N$)

As mentioned before, the lubricant density and viscosity are also affected by pressure changes. Figure 2.11 to Figure 2.14 show the effect of the external force and the rolling speed on these parameters. The viscosity and density profiles are similar to that of the pressure distribution. Augmenting the external force results in visible increases in the lubricant viscosity and density, mostly near the center of the contact zone. On the other hand, the rolling speed has a minimal effect on the lubricant properties.

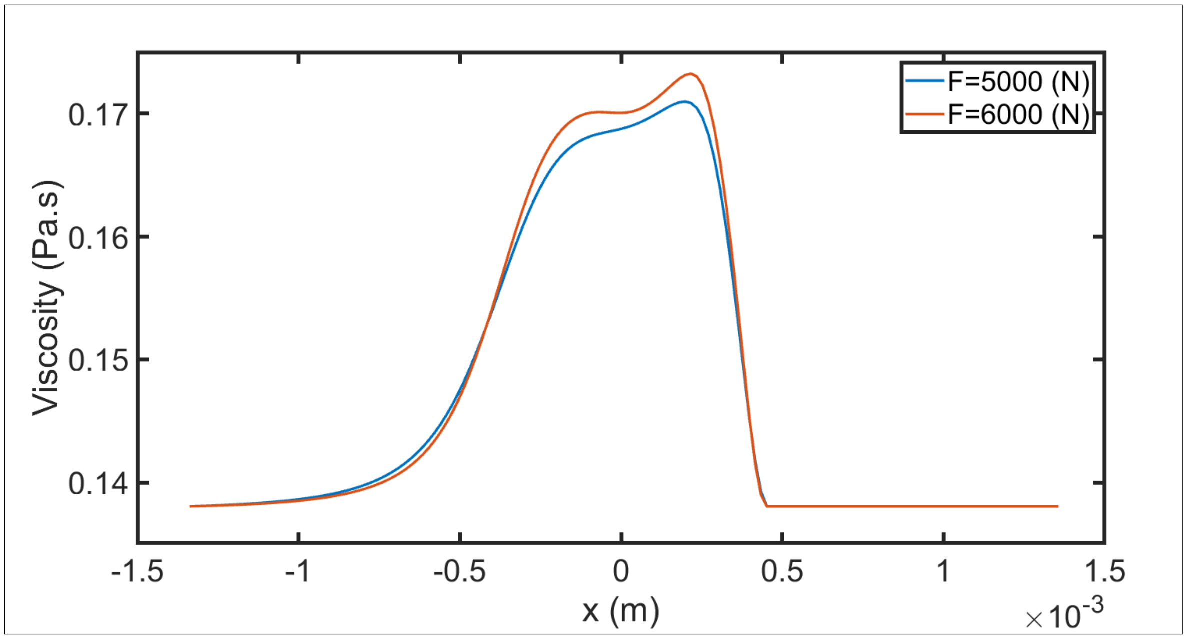

Figure 2.11 Lubricant viscosity at the midplane of EHL contact for different loads

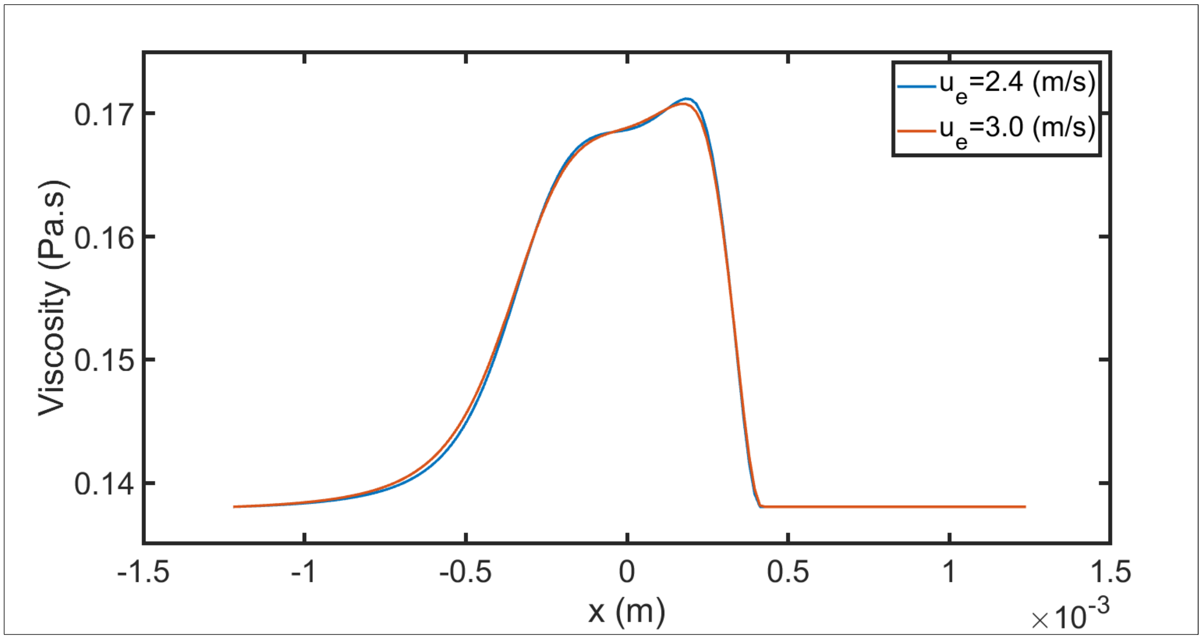

Figure 2.12 Lubricant viscosity at the midplane of EHL contact for different rolling speeds

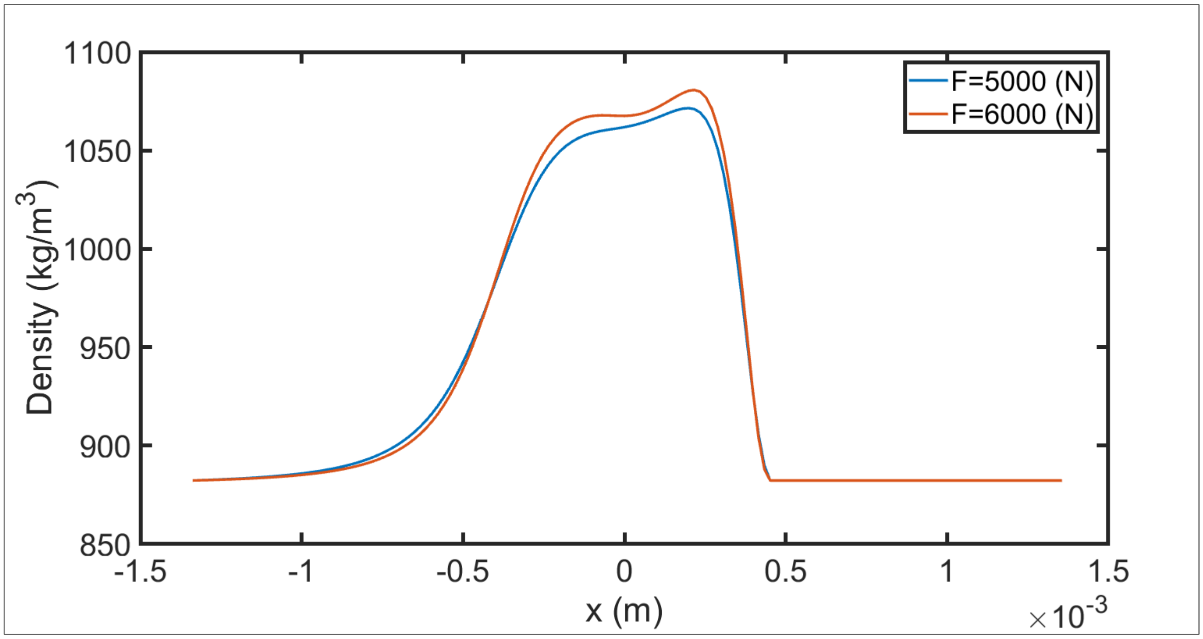

Figure 2.13 Lubricant density at the midplane of EHL contact for different loads

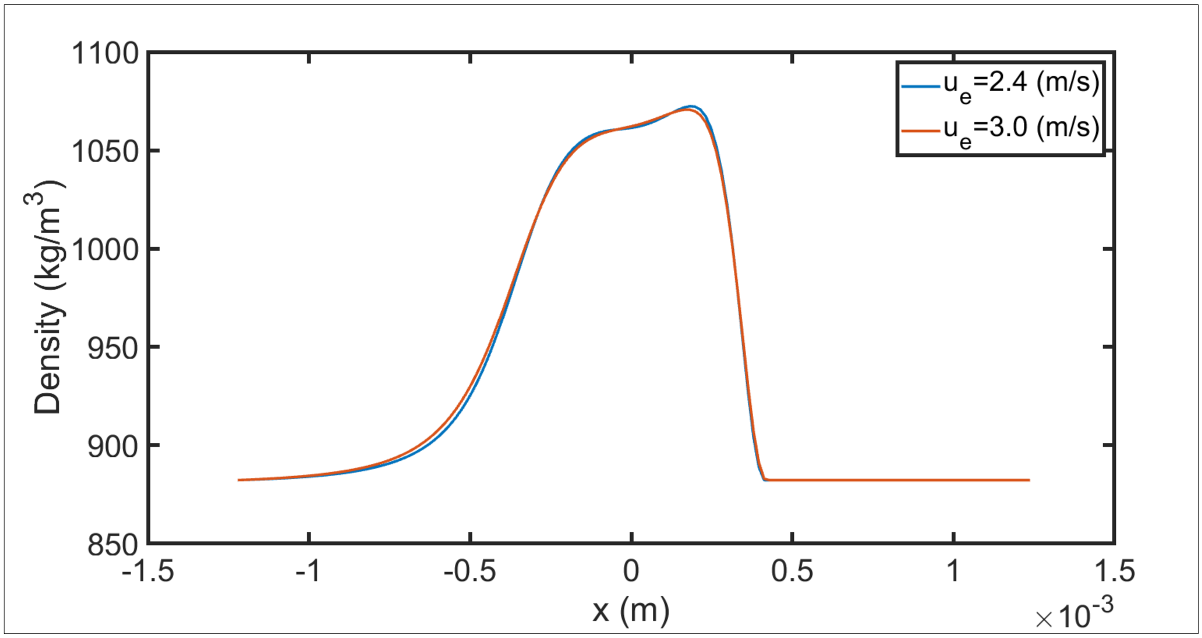

Figure 2.14 Lubricant density at the midplane of EHL contact for different rolling speeds

2.6 Conclusion

This chapter introduced the EHL calculations for smooth surfaces into the model. It particularly described the influence of external loads and relative rotational velocity on the EHL pressure distribution. The influence of these parameters on the film thickness was also examined. The calculation of the pressure distribution and film thickness presented in this chapter result from a modeling approach put forward in reference (Najjari & Guilbault, 2014). This numerical approach expands the Reynolds equation into its finite differences form over a 2D area representing the lubricated zone. Moreover, since it models smooth surfaces, the adopted form of the Reynolds equation neglects the time derivative term, and hence reduces the problem to a purely geometrical formulation. This solution can now be extended to rollers with pitted surfaces to investigate the effect of this common degradation on pressure distributions and film thickness. Therefore, the next chapter brings back the time derivative component into the solution of the Reynolds equation.

CHAPTER 3

EHL MODELING OF PITTED SURFACES

3.1 Introduction

Surface degradations in rolling contacts affect both the lubrication quality and system efficiency. Specifically, pitting, which is a common type of damage in rolling contact, can drastically alter the pressure distribution profile, the lubricant film thickness, the lubricant viscosity and density, and the coefficient of friction. This chapter adapts the model prepared in the previous chapters to give it the capacity of accounting for the pitting presence. The following investigation also examines the effects of surface pitting on pressure distributions, lubrication quality, and friction. This chapter describes the important contributions of the study, and thus responds to the objective set established in introduction chapter.

3.2 Surface pitting failure

Together with micro-pitting, pitting is one of the principal failure modes occurring in rolling contacts. Pitting is a 3D fatigue phenomenon controlled by the type of cycling contact, the extent of loading, the surface quality, the lubrication nature, the temperature, and the material microstructure. Pitting is generated when a crack is initiated and propagated due to cycling loadings (Fajdiga, Flašker, & Glodež, 2004). Depending on the conditions, pitting can be initiated at surface points or subsurface locations (Figure 3.1).

Under cycling loads, microcracks initiated at subsurface locations may propagate, join each other and reach the surface to form a subsurface initiated pit. Surface initiated microcracks also progress under cycling loadings. However, to propagate and form surface-initiated pits they require additional conditions governed by the lubricant presence and the friction direction. Therefore, only a fraction of microcracks initiated at surface points leads to the formation of debris. The contact fatigue process results in crater formation modifying the mechanical aspect of surfaces. Generally, craters formed by microcracks initiated below the surface are deeper than those caused by surface-initiated microcracks. The pit formation process is out of the scope of the present study.

The following investigation does not include any contact fatigue modeling or simulation. It instead considers the influence of already formed craters onto the lubrication conditions. The study introduces surface pits by local modifications of the rolling object geometry. In fact, the pitting zones are generated by adjusting the initial distances of the surfaces from the tangent plane at selected points. Combined with the rotational speed of the elements, these surface alterations generate time variations of h in Eq. (2.3) of chapter 2. The original $h(x, y)$ thus becomes $h(x, y, t)$, where $g(x, y)$ introduces the modification.

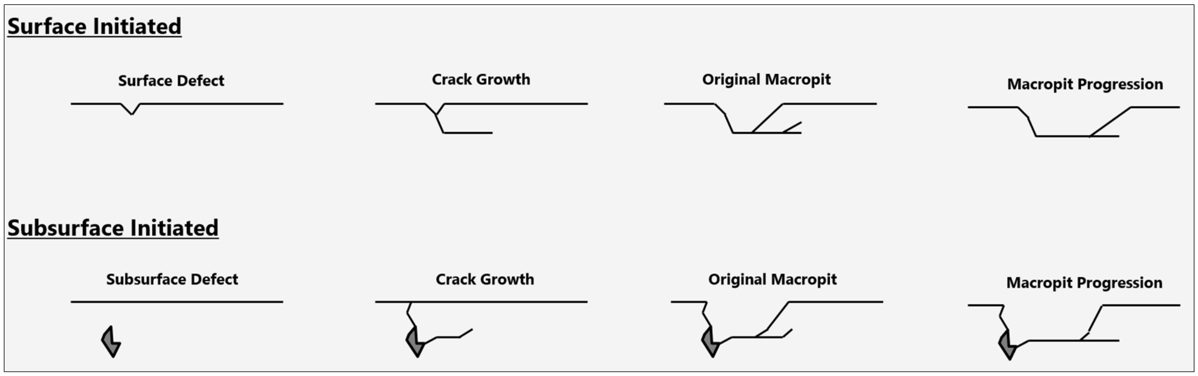
Surface Initiated
Surface Defect
Crack Growth
Original Macropit
Macropit Progression
Subsurface Initiated
Subsurface Defect
Crack Growth
Original Macropit
Macropit Progression

Figure 3.1 Crater formation for the two pitting types-("Polishing - Gear Failures - Failure Atlas - ONYX InSight," n.d.)

3.3 Surface pitting simulation

When ignoring time variations of the lubricant density (ρ), the Reynolds equation presented in chapter 2 (Eq. (2.1)) becomes for pitted surfaces,

$$\frac{\partial}{\partial x}\left(\frac{\rho h^3}{\eta}\frac{\partial p}{\partial x}\right)+\frac{\partial}{\partial y}\left(\frac{\rho h^3}{\eta}\frac{\partial p}{\partial y}\right)=12u_e\frac{\partial(\rho h)}{\partial x}+\rho\frac{\partial h}{\partial t} \tag{3.1}$$

The presence of the additional time term modifies the previous finite difference solution approach since the film thickness now evolves not only because of convergent and divergent zones associated with the smooth surfaces but also because of the passage of irregular surfaces in the contact zone. Under the conditions considered in chapter 2, the invariant nature of the surfaces reduced the role of the roller speeds to the generation of u_e, the fluid entraining speed, and thus practically reduced the problem to the solution of a spatial equation. To account for the time derivative term, the finite difference formulation given by Eq.(3.3) modifies the solution put forward in (Najjari & Guilbault, 2014). Figure 3.2 shows the pit shape considered in this simulation and illustrates the pit passing through the contact zone.

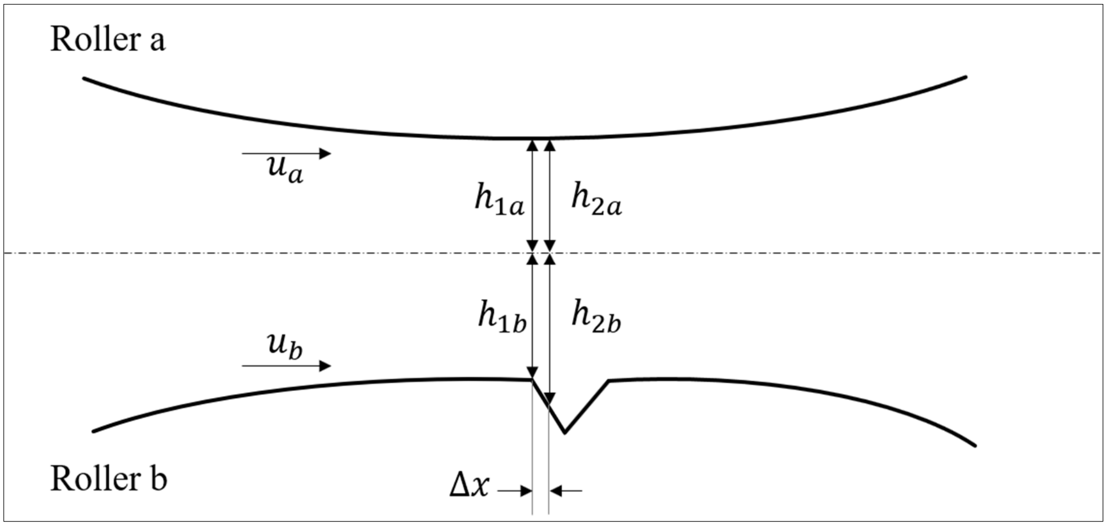

Figure 3.2 Schematic single pit passing through the contact zone

The parameters in Figure 3.2 are used in calculating the time derivative term of the Reynolds equation (Eq.(3.1)) The movement of the rollers between positions 1 and 2 leads to $\frac{\partial \mathrm{h}}{\partial \mathrm{t}} = \frac{\Delta \mathrm{h}}{\Delta \mathrm{t}}$. over the discretized domain. The time-variant term is thus determined as:

$$\rho \frac{\partial h}{\partial t} = \rho \left(\frac{h_2 - h_1}{2\Delta t} \right) = \rho \left(\frac{(h_{2a} + h_{2b}) - (h_{1a} + h_{1b})}{2\Delta t} \right) = \rho \left(\frac{\frac{\Delta h_a}{\Delta t} + \frac{\Delta h_b}{\Delta t}}{2} \right) \tag{3.2}$$

Replacing $\Delta t = \frac{\Delta x_a}{u_a} = \frac{\Delta x_b}{u_b}$ in Eq. (3.2), the time derivative term then becomes:

$$\rho \frac{\partial h}{\partial t} = \rho \frac{u_a \frac{\Delta h_a}{\Delta x_a} + u_b \frac{\Delta h_b}{\Delta x_b}}{2} \tag{3.3}$$

To consider the above time-variant term in the EHL solution, the solution algorithm requires an additional time loop. At the end of the loop, the location of the pit and the surface geometry are updated to account for the roller rotation. This approach incorporates the pit coming in, crossing, and exit of the contact region. Figure 3.3 shows the modified program flowchart.

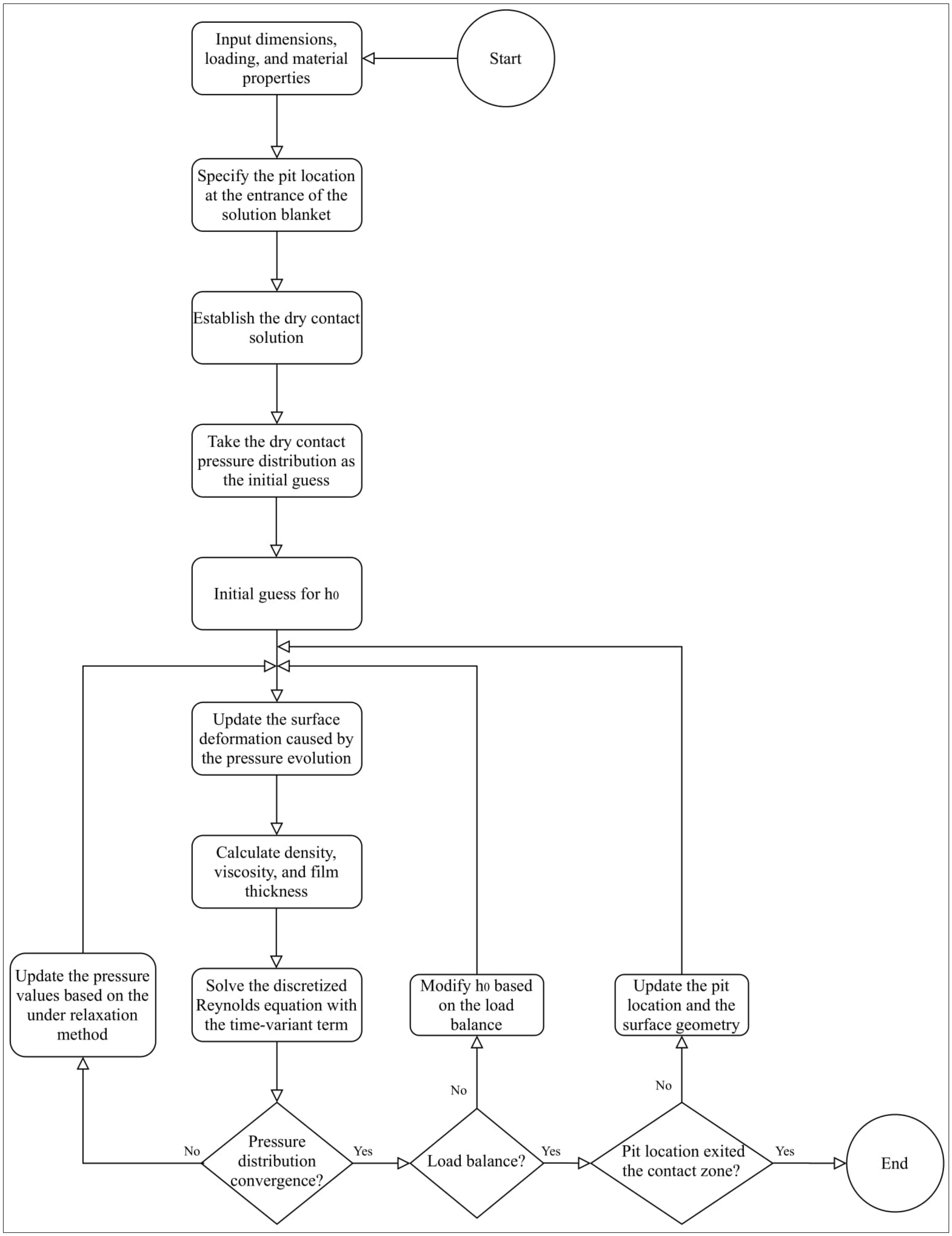
Start
Input dimensions, loading, and material properties
Specify the pit location at the entrance of the solution blanket
Establish the dry contact solution
Take the dry contact pressure distribution as the initial guess
Initial guess for h0
Update the surface deformation caused by the pressure evolution
Calculate density, viscosity, and film thickness
Solve the discretized Reynolds equation with the time-variant term
Pressure distribution convergence?
No
Update the pressure values based on the under relaxation method
Yes
Load balance?
No
Modify h0 based on the load balance
Yes
Pit location exited the contact zone?
No
Update the pit location and the surface geometry
Yes
End

Figure 3.3 Modified flowchart of the numerical solution

As mentioned before, surface pitting modifies the geometry of the rotating objects. Here, the surface pits are represented by notches on the cylinder surfaces. Figure 3.4 shows the pit movement. Figure 3.4 also includes the 2D pit dimensions: the pit width (P_w) and the pit depth (P_d). These parameters do not vary along the roller axial direction. Therefore, the pit length (P_l) completes the pit form definition. The model assumes that all pits on a surface are identical.

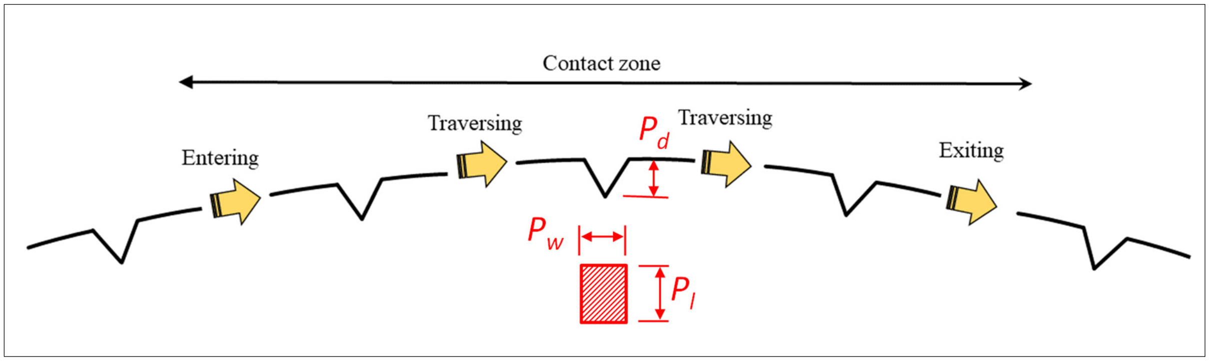

Figure 3.4 Pit passing through contact zones

3.4 Validation-Film thickness and pressure distribution

This section validates the proposed modeling strategy. It compares the model predictions to the results published in two reference works. (Warhadpande & Sadeghi, 2010) investigated the effect of surface defects on rolling contact fatigue life. This paper examines the fatigue life of rollers with surface dents. The 2D line contact model proposes in this reference is based on a Voronoi finite-element model. While the present model includes a 3D representation, the 2D dent shape considered in this reference is similar to the pit geometry defined in Figure 3.4. Table 3.2 gives the simulation parameters considered by the authors. These values were inputted into the present model.

Table 3.2 Simulation conditions and dent dimensions-Taken from (Warhadpande & Sadeghi, 2010)

Elastic modulus (E)	200 GPa	Dimensionless speed ($U = \frac{\eta_0(u_1+u_2)}{2E'R}$)	10^{-10}
Poisson's ratio (ν)	0.3	Dimensionless material parameter ($G = \alpha E'$)	3043
Maximum dry contact pressure (P_{Hz})	1 GPa	Dent width (d_w) here P_w	$30\mu m$
Dimensionless load ($W = \frac{w}{E'R^2}$)	1.3×10^{-4}	Dent depth (d_d) here P_d	$24\mu m$

The reference simulation considered a single dent. The results (Warhadpande & Sadeghi, 2010) show that when the dent is in the contact zone, the pressure rises at the edges and drops in the middle of it. Figure 3.5 compares the film thickness and the pressure distribution predicted by the present model to the reference results. Figure 3.5 integrates both the smooth surface and the dent cases. The graphs show for the two conditions that the film thickness and the pressure distribution profiles agree with the reference results. The two models predict significant effects of the pit/dent on the pressure profile as well as on the film thickness. The slight differences visible at the spikes may be attributed to the different viscosity and density representations integrated into the two EHL models.

To improve the evaluation precision, Table 3.3 compares the dimensionless pressure and film thickness predictions with the Warhadpande et al.'s values taken at three important positions close to the pit/dent location.

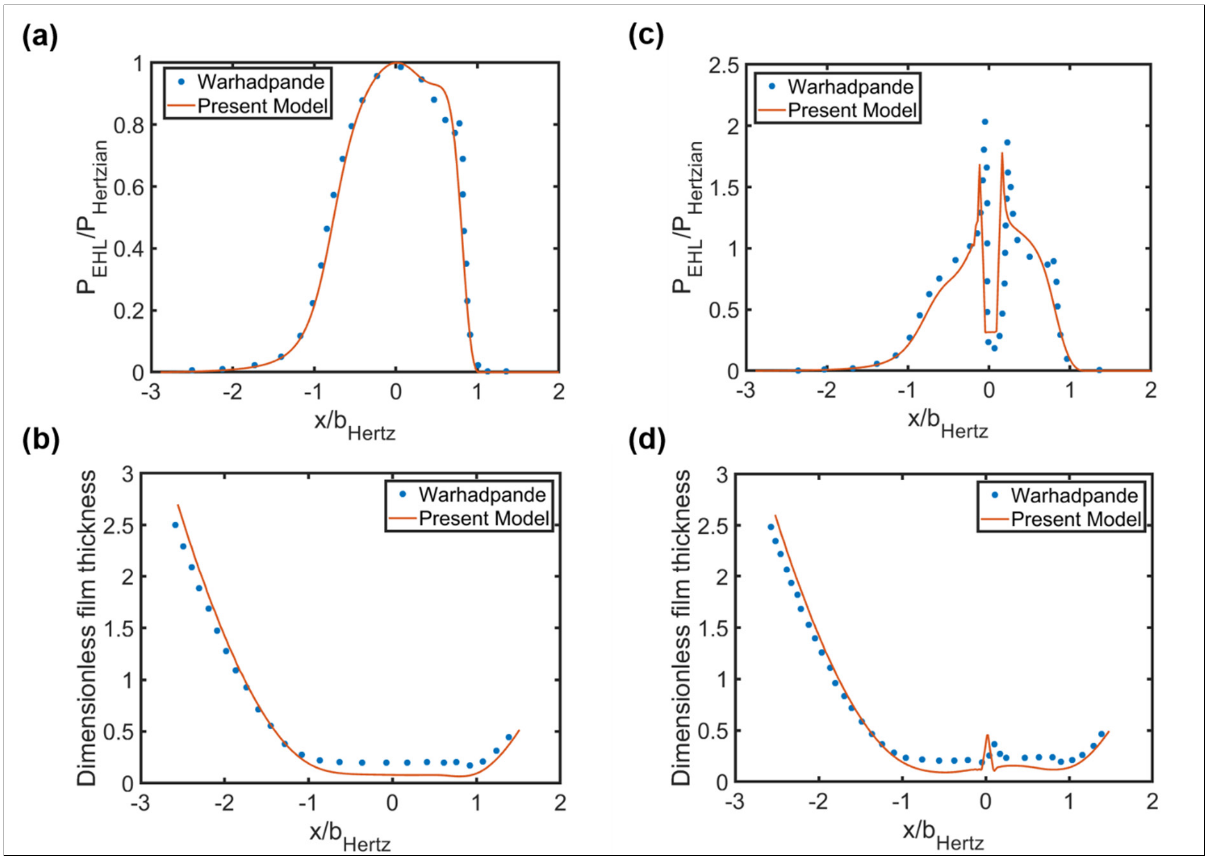

Figure 3.5 Result comparison (a) EHL pressure distribution for the smooth condition, (b) EHL film thickness profile for the smooth condition, (c) EHL pressure distribution for the pitted surface condition, and (d) EHL film thickness profile for the pitted surface condition.

Table 3.3 Comparison of the pressure profile and film thickness extremums for the two numerical models

	Reference (Warhadpande & Sadeghi, 2010)	Present model
Maximum dimensionless pressure at the edge of the pit/dent	2.03	1.79
Minimum dimensionless pressure at the middle of the pit/dent	0.24	0.31
Maximum dimensionless film thickness at the pit/dent	0.37	0.45

To complete the validation, the following compares the model predictions to the experimental measurements published by (Höhn, Michaelis, & Kreil, 2006). In this reference, the authors considered various surface textures and investigated their effects on the pressure distributions and the lubricant film thickness. They tested transverse textures generated on cylindrical surfaces in contact with smooth cylindrical surfaces. The texture shape is reproduced in Figure 3.6. Since the texture form was maintained constant along the roller axis, the reference experimental measurements allow 2D comparisons.

While the texture form presents flat valleys, the proposed EHL model can easily reproduce the surface profile (see Figure 3.6). Table 3.4 indicates the test parameters considered by (Höhn et al., 2006) as well as the simulation parameters when there is a difference. Moreover, since (Höhn et al., 2006) only indicates the ISO VG of the tested lubricant and does not mention its properties, the following values were considered during the simulations: the density (ρ = 888 kg/m^3), the viscosity at 40 °C (ν = 100 cSt), the viscosity-pressure coefficient ($\alpha = 20\,\mathrm{GPa}^{-1}$), the slope factor ($n_{313K} = 0.57$ and $n_{373K} = 0.993$) and the Modulus (G_{f313K}=4.5 MPa).

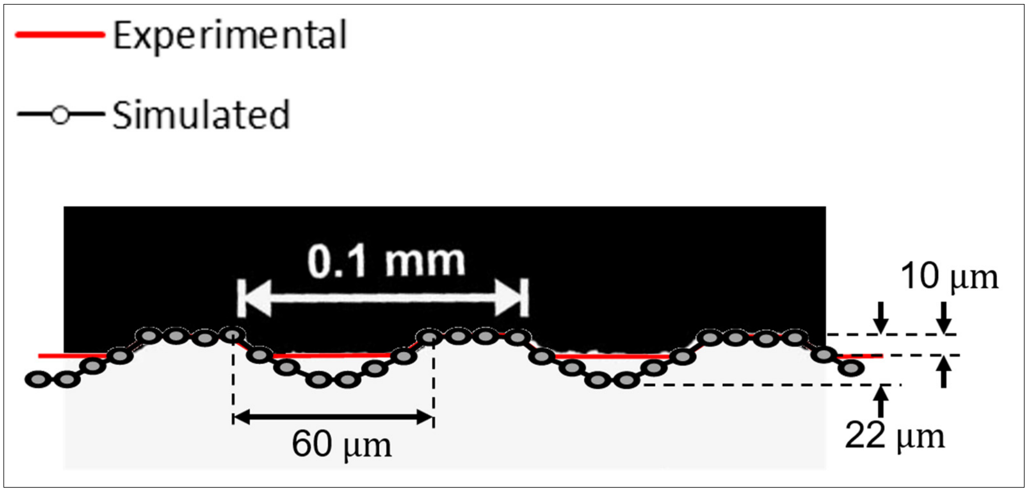

Figure 3.6 Transverse surface texture shape study in (Höhn et al., 2006)

Table 3.4 Experimental (Taken from (Höhn et al., 2006)) and simulation parameters

Elastic modulus (E)	200 GPa	Summation of speeds $(u_1 + u_2)$	$8\ m/s$
Poisson's ratio (ν)	0.3	EHL dimensionless material parameter $(G = \alpha E')$	4396
Equivalent radius of the rollers (R)	3 mm		
Maximum dry contact pressure (P_{Hz})	600 MPa	Texture width modeled as P_w	$60\ \mu m$
Slip ratio $(100 * (u_1 - u_2)/u_1)$	30%	Texture depth (modeled P_d)	$10\ \mu m$ $(22\ \mu m)$
Lubricant ISO VG	100	Lubricant Inlet temperature	22 ℃

The authors of the reference indicate that the peaks and valleys of the textured surface directly influenced the pressure profile. In fact, at the peaks, which correspond to the edge of the pit in the present model, the pressure rises, while the pressure decreases over the valleys. Figure 3.7 shows that the present model predicts the reported experimental results quite well. Overall, the experimental pressure distribution is slightly smoother than the model predictions. This smoothing effect may be attributed to the inevitable edge blunting generated by the fabrication process. Table 3.5 compares the dimensionless pressure predictions to the reference experimental values taken at the peak edge and the center of the valley. While the graph in Figure 3.6 shows that the model produces accurate predictions of the contact width and overall pressure response, this last comparison demonstrates that the model also provides high precision levels of the pressure distribution minima.

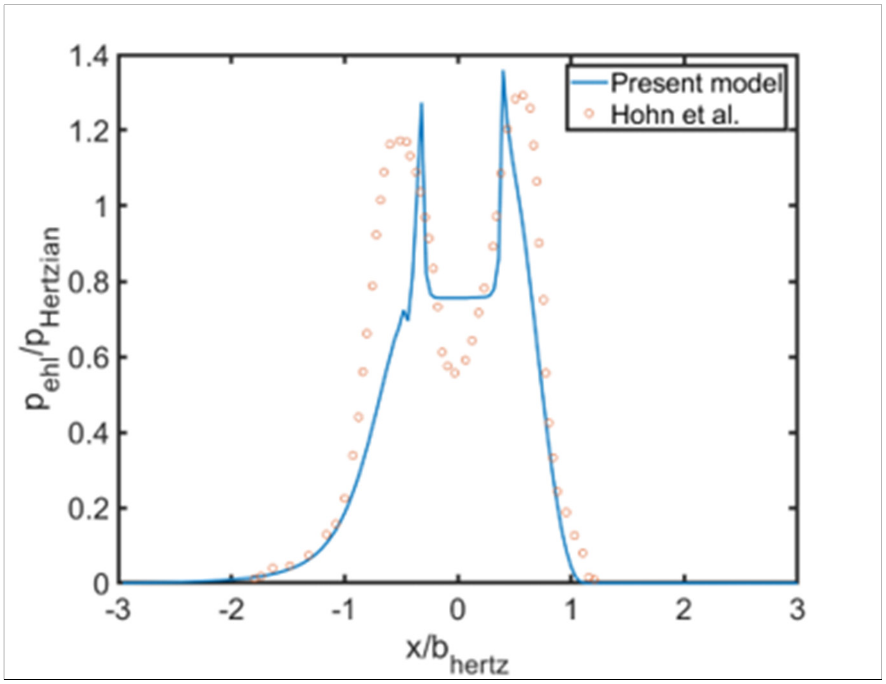

Figure 3.7 Comparing the experimental pressure distribution in (Höhn et al., 2006) with present model

Table 3.5 Comparison of the pressure distribution and film thickness extremums for the experimental measurements and the present model

	Experiment (Höhn et al., 2006)	Present model
Maximum dimensionless pressure at the edge of the pit (peak)	1.3	1.36
Minimum dimensionless pressure at the middle of the pit (valley)	0.56	0.76

3.5 Single pit simulation

Following the above 2D validation, this section examines the 3D response of selected case studies. The first EHL contact problem involves two rollers with a single pit. Table 3.6 shows the simulation parameters defining the tested conditions.

Table 3.6 Material parameters and problem conditions for single pit simulation

Elastic modulus (E)	200 GPa	Dimensionless speed $(U = \frac{\eta_0(u_1+u_2)}{2RE'})$	1.3×10^{-10}
Poisson's ratio (ν)	0.3	Dimensionless load parameter $(W = \frac{w}{RE'})$	1.36×10^{-4}
Equivalent radius R	30 mm	Dimensionless material parameter $(G = \alpha E')$	1470
Maximum dry pressure (P_{Hz})	1.05 GPa	Pit width P_w	0.38 mm
Pit length P_l	0.5 mm	Pit depth P_d	2.5×10^{-2} µm

Figure 3.8 to Figure 3.13 present the 3D EHL pressure distributions calculated at six different locations (x_p) during the pit onward movement. The x_p positions are measured from the initial contact line. Thus, the negative values correspond to positions before the initial contact line whereas the positive ones indicate behind positions. As the pit traverses through the contact region, a visible pressure rise is generated on the leading-edge side (see Figure 3.10) and moves with the pit. This pressure rise reaches its maximum value at the center of the contact zone. Approaching this position, a second pressure increase also appears on the trailing edge side (see Figure 3.11). This pressure distribution corresponds to the descriptions presented before during the validation process. After the central position, the pressure jump amplitude starts to reduce (see Figure 3.12). However, when almost completely out of the pressure zone, the trailing edge of the pit causes a second pressure upsurge. This pressure rise occurs to avoid any flow rise or drainage of the contact area when the pit position causes an augmentation of the fluid passage area; the pressure surge prevents the violation of the continuity equation incorporated in the Reynolds equation (see Figure 3.13). Finally, a few time steps after the pit leaves the contact region, the pitting effect vanishes, and the EHL pressure distribution resulting from smooth surfaces is restored.

To complete the analysis, Figure 3.14 displays the 2D pressure and film thickness distributions established at the central axial position for the pit locations considered in Figure 3.8 to

Figure 3.13. The plots in Figure 3.14 reveal that the pit impact on the film thickness profile is proportionally more important than on the pressure distribution: the film thickness demonstrates major augmentations over the pit area. Moreover, these charts also indicate that, while the local repercussions at the pit location are intense, the changes at the remaining sections of the profile are of lesser amplitude. In fact, the surface pit acts as a leakage point; the lubricant is accumulated in the pit. Therefore, the presence of pits may be beneficial in the case of severely starved contacts (Dumont, Lugt, & Tripp, 2002).

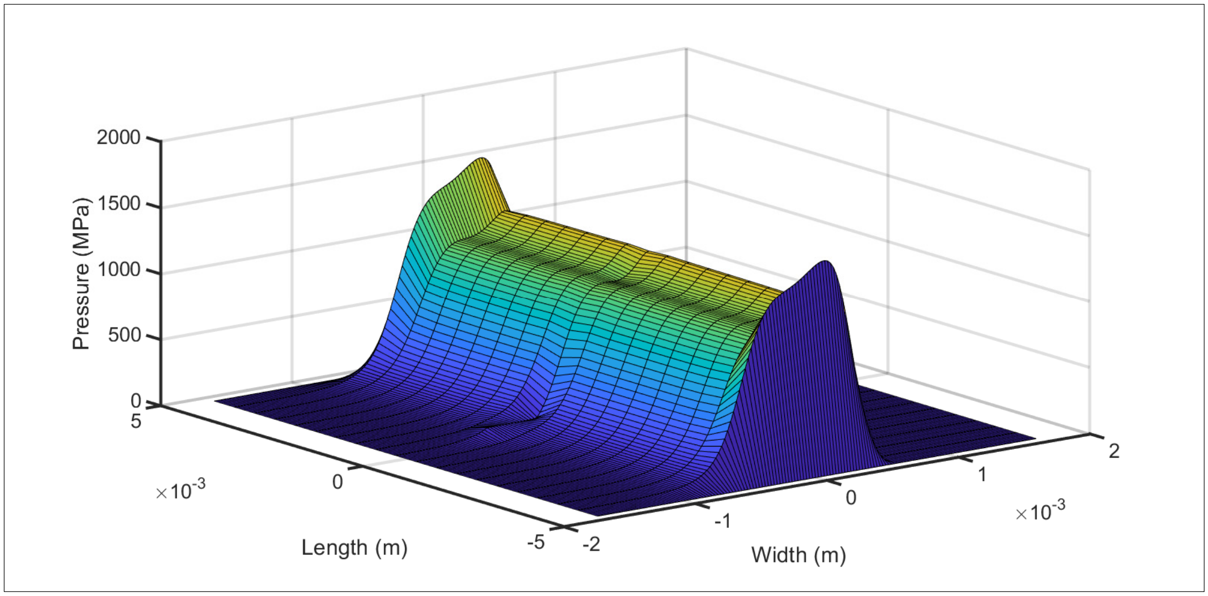

Figure 3.8 3D EHL pressure distribution when the pit position $x_p = -0.78\ mm$

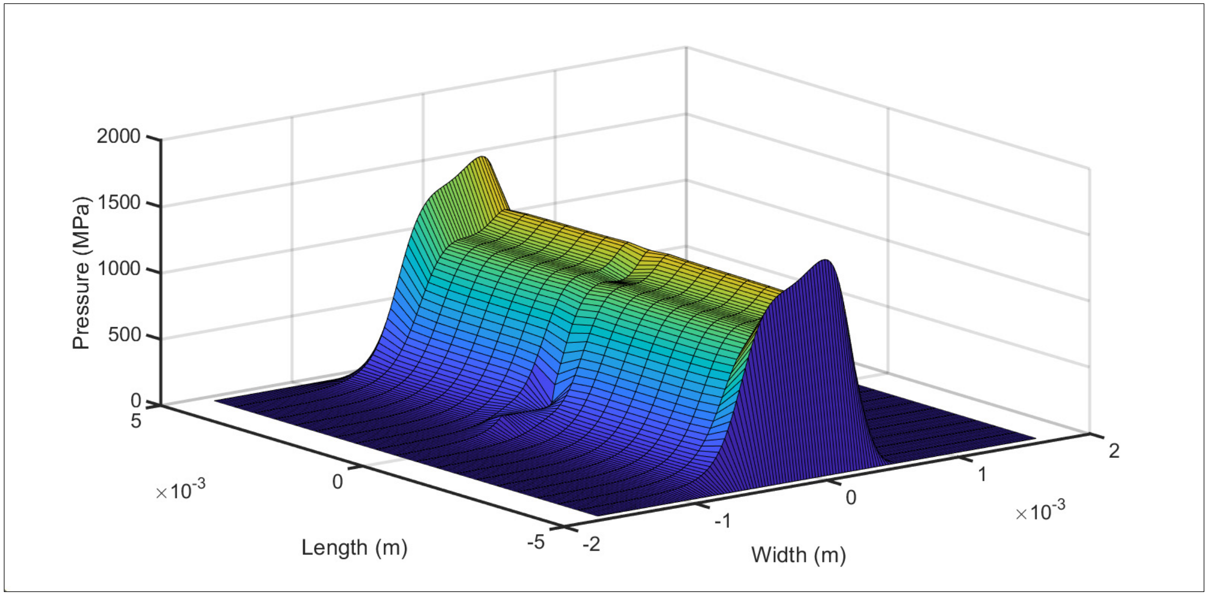

Figure 3.9 3D EHL pressure distribution when the pit position $x_p = -0.67\ mm$

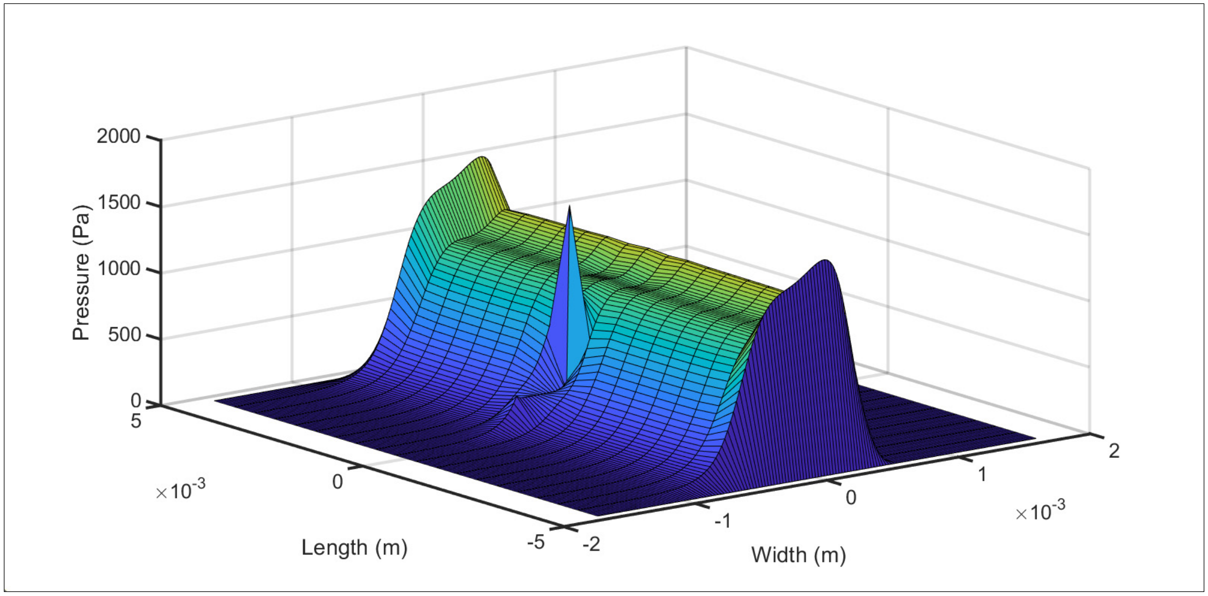

Figure 3.10 3D EHL pressure distribution when the pit position $x_p = -0.56\ mm$

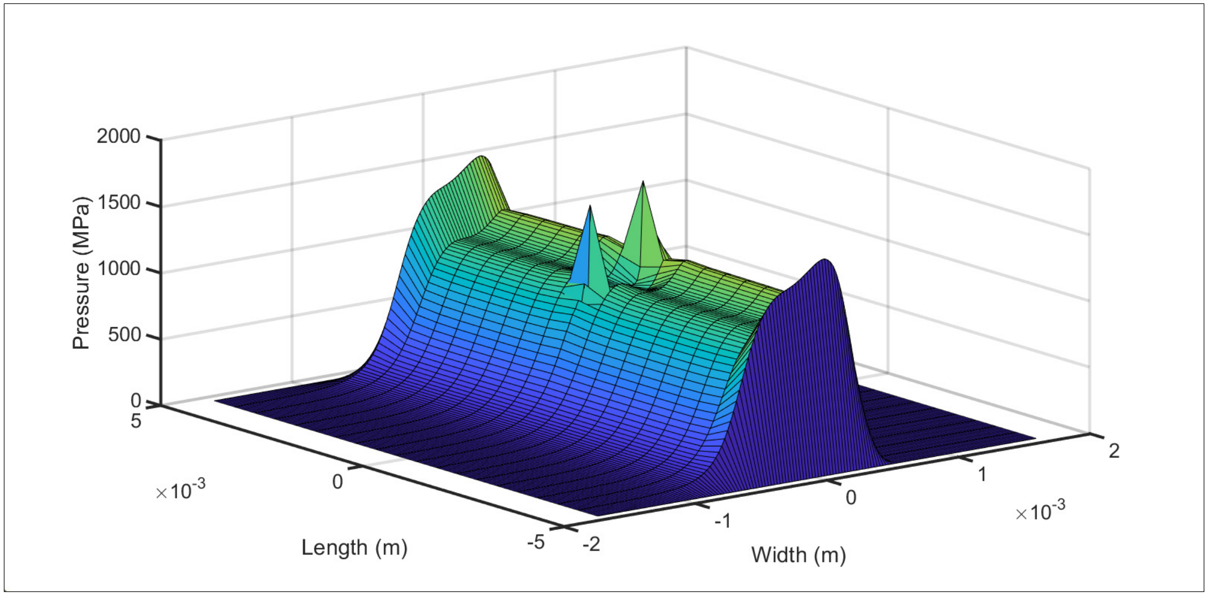

Figure 3.11 3D EHL pressure distribution when the pit position $x_p = 0$

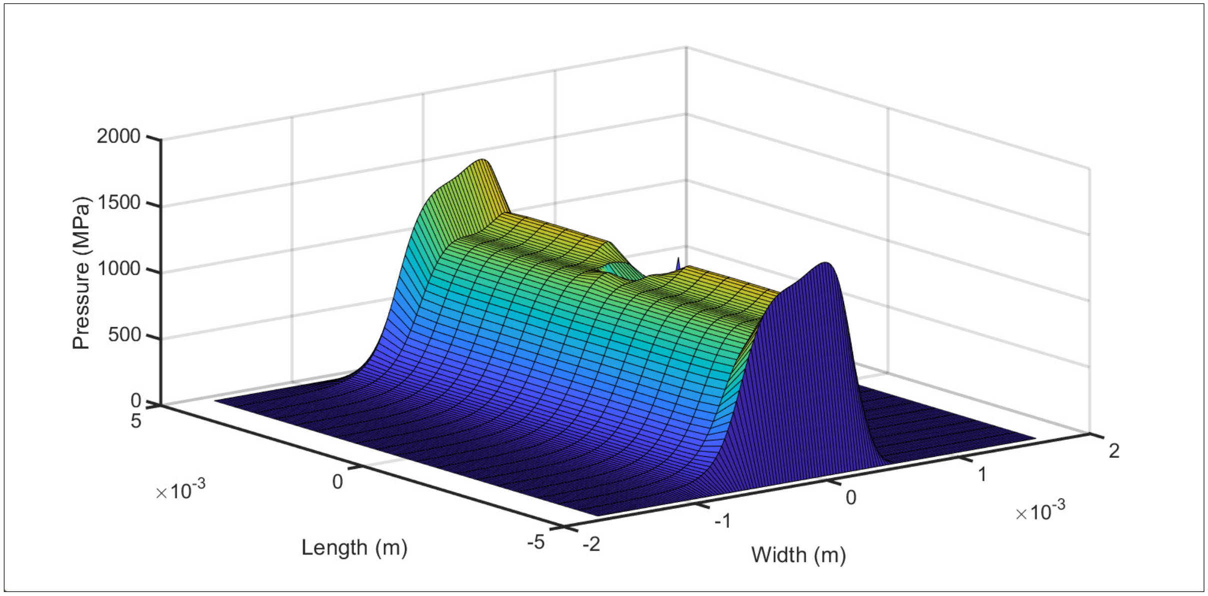

Figure 3.12 3D EHL pressure distribution when the pit position $x_p = 0.27\ mm$

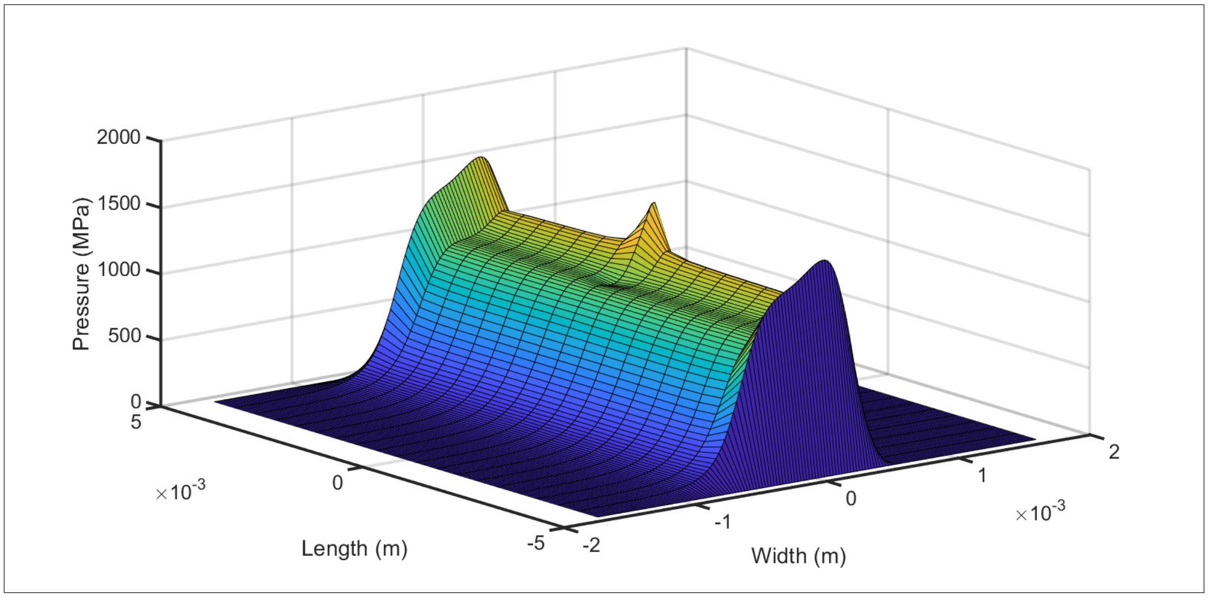

Figure 3.13 3D EHL pressure distribution when the pit position $x_p = 0.56\ mm$

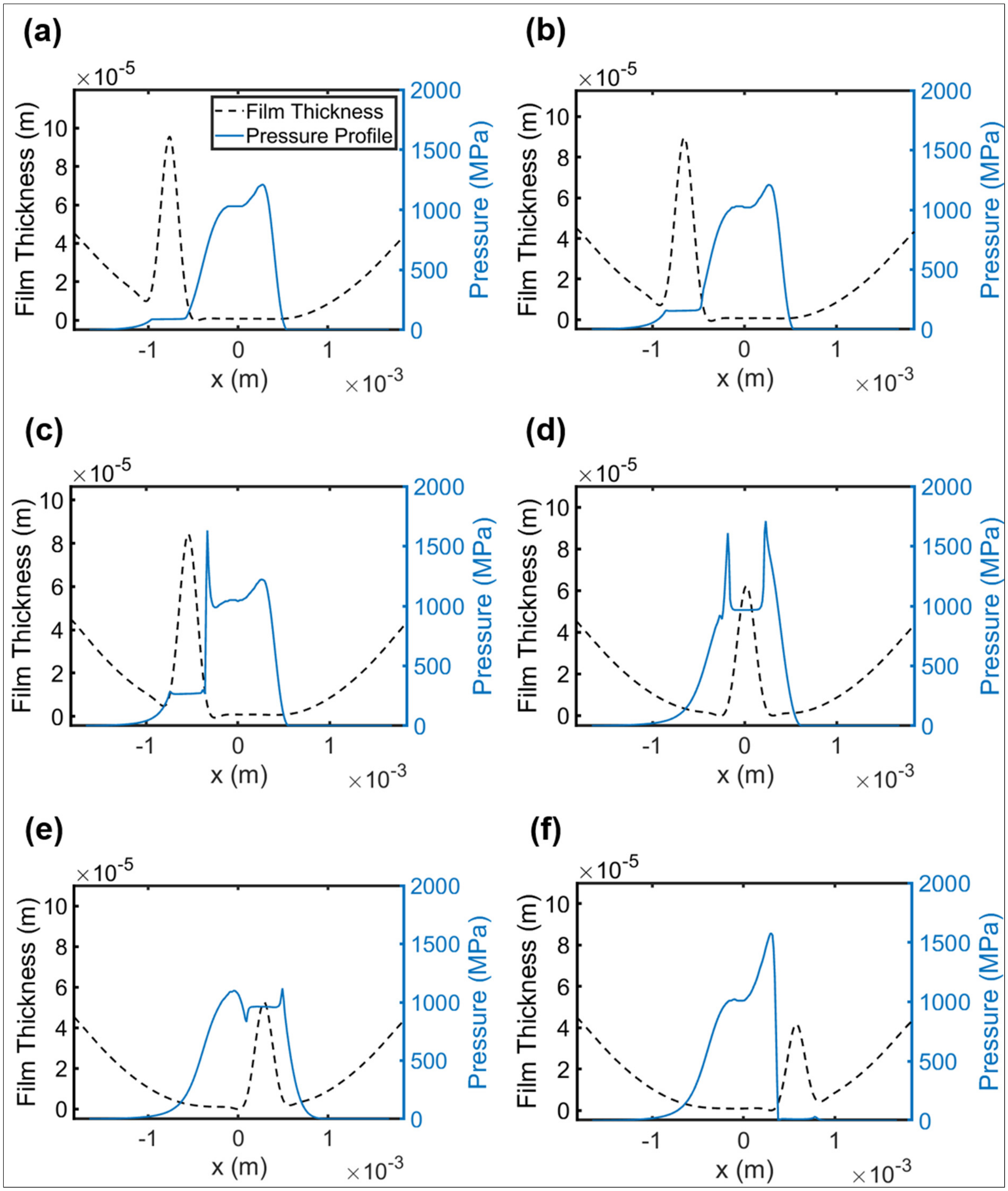

Figure 3.14 2D EHL pressure distributions at the central axial position of the rollers for the pit locations (a) $x_p = -0.78\ mm$, (b) $x_p = -0.67\ mm$, (c) $x_p = -0.56\ mm$, (d) $x_p = 0$, (e) $x_p = 0.27\ mm$, (f) $x_p = 0.56\ mm$

Figure 3.15 presents the longitudinal EHL pressure distributions calculated along the initial contact line for the pit positions considered in Figure 3.8 to Figure 3.13. As soon as the pit enters the pressure area, the longitudinal pressure distribution deviates from the uniform distribution. The more important pressure drop occurs when the pit leaves the contact region.

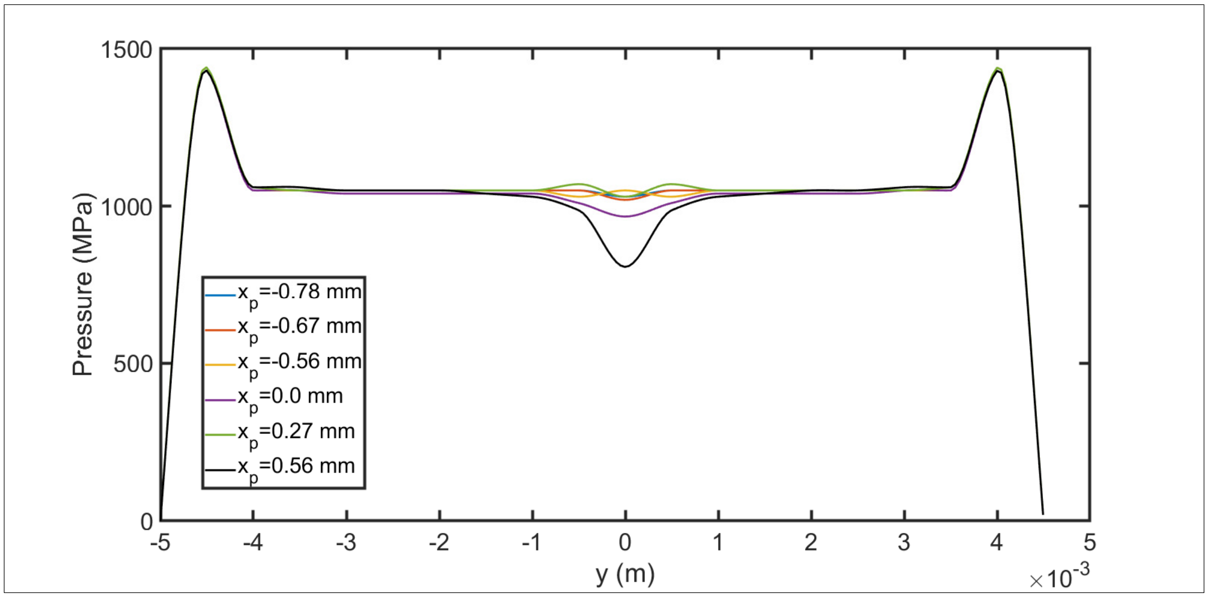

Figure 3.15 Longitudinal pressure distribution in the presence of a single pit passing through the contact zone

3.6 Effect of pit depth

To study the effect of pit severity, this section reproduces the simulations presented in section 3.5 with a pit depth (P_d) of 1.25e^{-2} µm or half of the initial value. Figure 3.16 juxtaposes the 2D EHL pressure distributions calculated for the two pit depths at the pit positions examined before.

While the general behavior of the pressure profiles remains similar for both pit sizes, meaning that the pressure rises happen at the pit edges, decreasing the depth reduces the perturbation engendered by the pit presence. This reduction effect is particularly visible at the pit positions x_p = -0.56 and 0 mm. This initial conclusion is logical, since reducing the pit depth bring the surface closer to a smooth condition. Moreover, the lubricant reserve accumulated in a pit should also decrease with a depth reduction. Therefore, while this aspect was not investigated in the present study, a detailed evaluation of the optimal pit depth remains pertinent, since depending on their size, surface cavities may help or degrade the lubrication quality (Dumont et al., 2002).

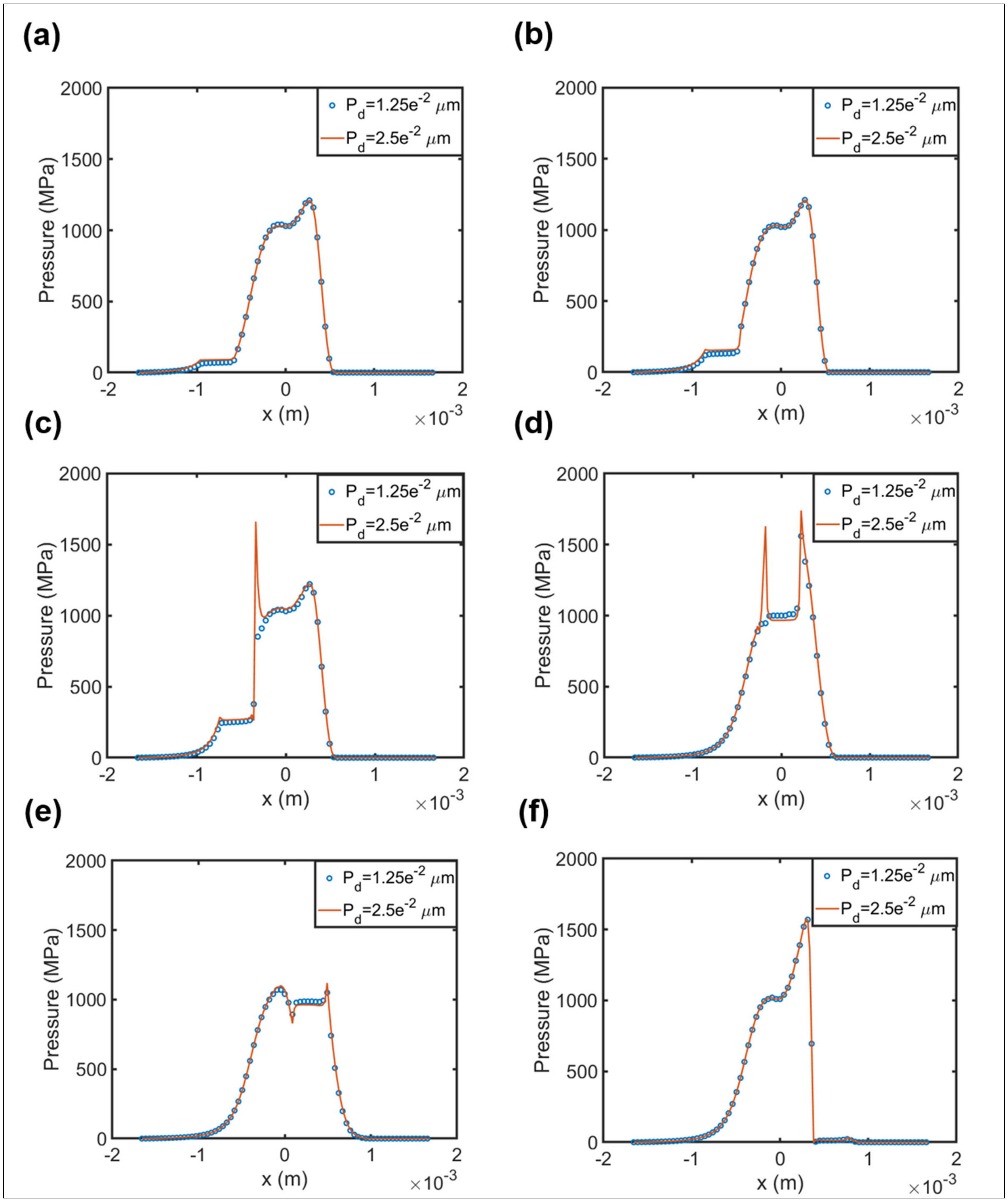

Figure 3.16 Effect of pit depth-2D EHL pressure distributions at the central axial position of the rollers for the pit locations (a) $x_p = -0.78\ mm$, (b) $x_p = -0.67\ mm$, (c) $x_p = -0.56\ mm$, (d) $x_p = 0$, (e) $x_p = 0.27\ mm$, (f) $x_p = 0.56\ mm$

3.7 Effect of pit arrangement

This section examines the influence of multiple pits on EHL pressure and film thickness distributions. The analysis includes two pit configurations: the first one comprises 3 identical pits aligned lengthwise along one of the rollers; the second configuration includes 3 rows of 3 identical pits aligned lengthwise along one of the roller lengths. The roller dimensions are the length $L = 9.5$ mm and the radius $r = 60$ mm. The two cylindrical rollers are of the same size. For both configurations, the separation between two consecutive pits is $l_{lp} = 2$ mm, while the distances from the two cylinder ends are uneven and equal to $l_{l1} = 2.75$ mm and $l_{l2} = 2.25$ mm, respectively. For the second configuration, the circumferential row separation is $l_c = 0.2$ mm. The pit dimensions are $P_w = 0.38$ mm, $P_l = 0.5$ mm, and $P_d = 2.5\times10^{-2}$ µm. Figure 3.17 depicts the pit arrangements. The operating conditions are those described in Table 3.6.

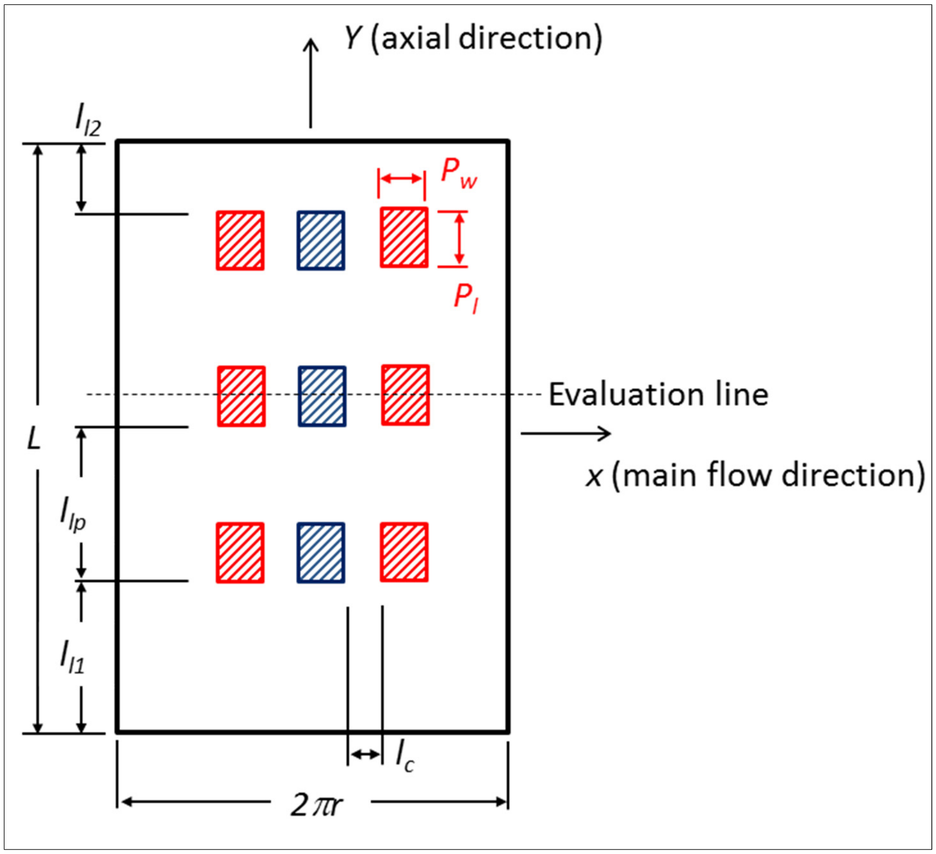

Figure 3.17 Multiple pit arrangements

Figure 3.18 presents the 3D EHL pressure distribution calculated for the 3-pit configuration when the pits are located at the initial contact line position. Figure 3.19 displays the pressure distributions established for the 9-pit configuration when the central pit row is located at the initial contact line position. Figure 3.20 and Figure 3.21 presents the 3D form of the film thickness predicted for the two pit configurations.

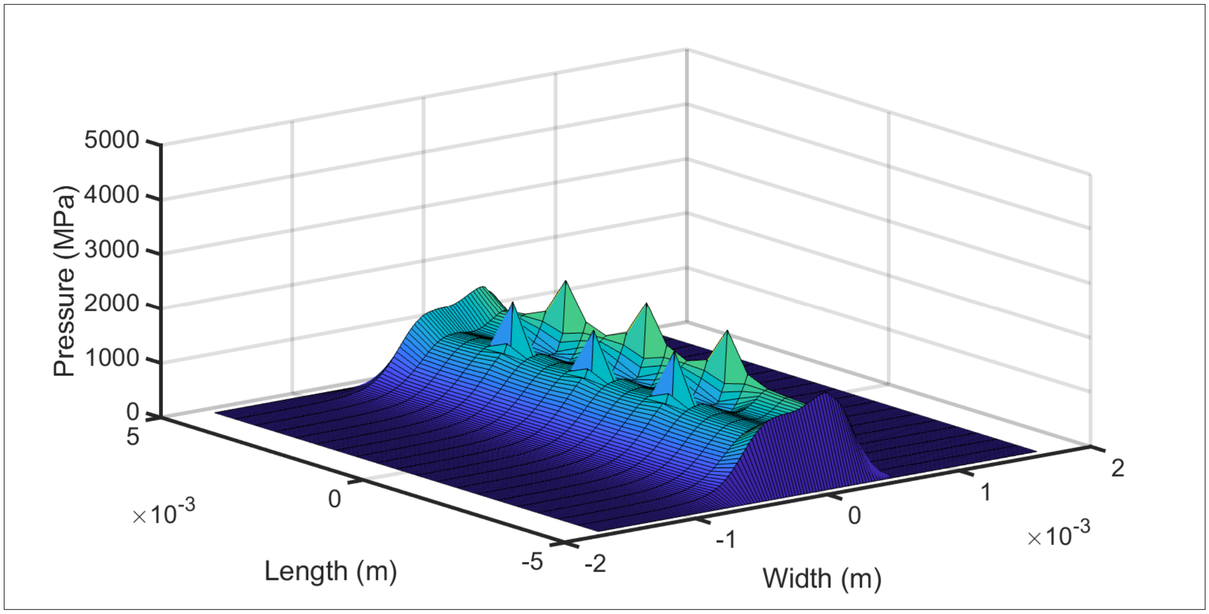

Figure 3.18 3D EHL pressure distribution for the 3-pit configuration

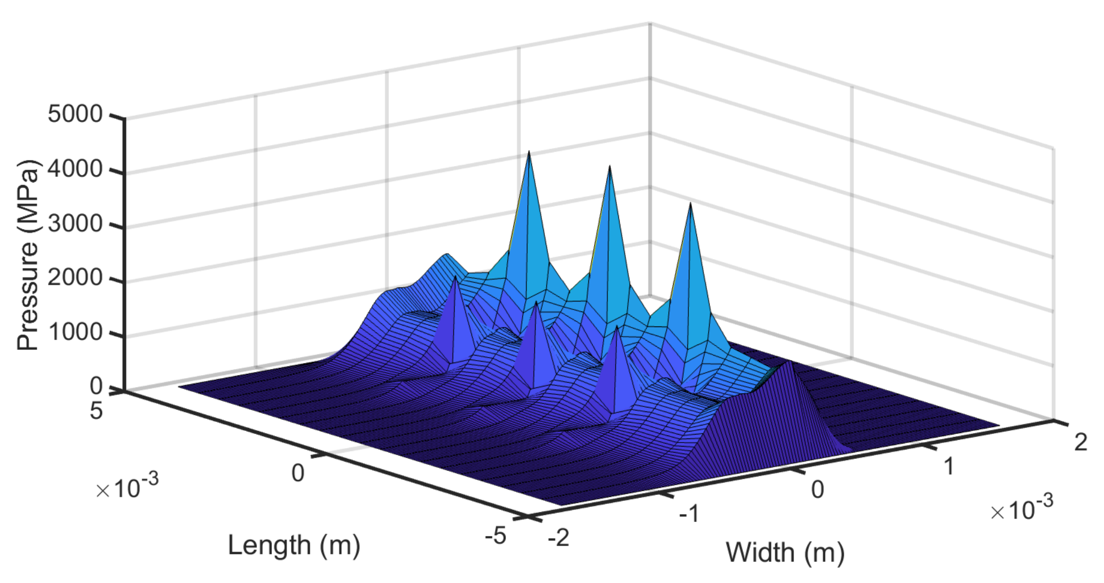

Figure 3.19 3D EHL pressure distribution for the 9-pit configuration

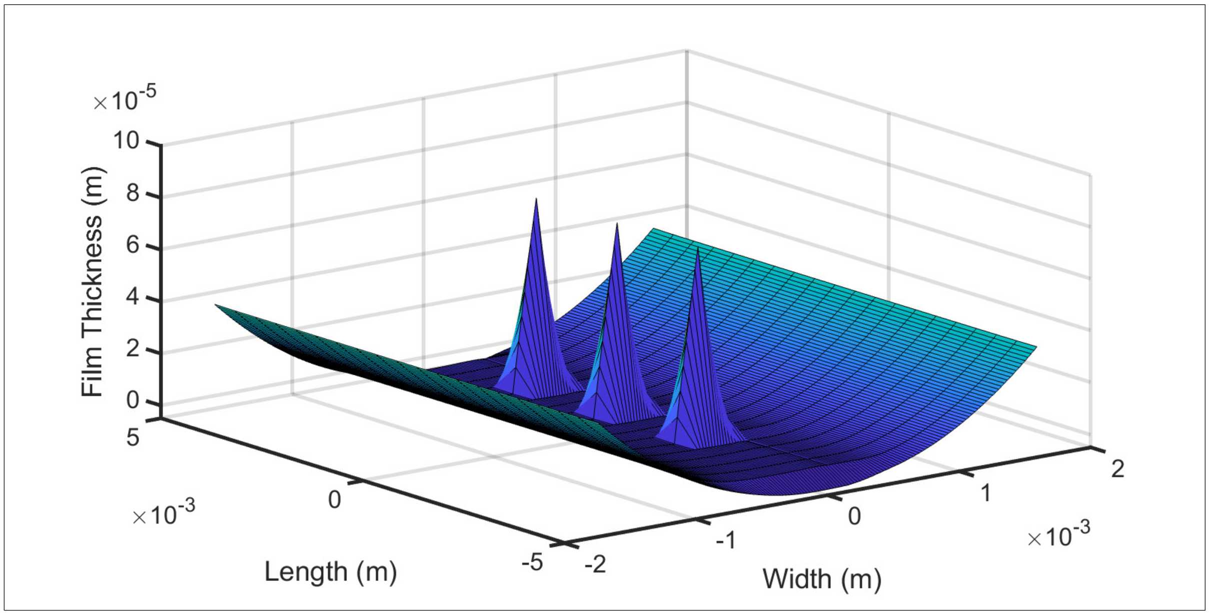

Figure 3.20 3D EHL Film thickness profile for the 3-pit configuration

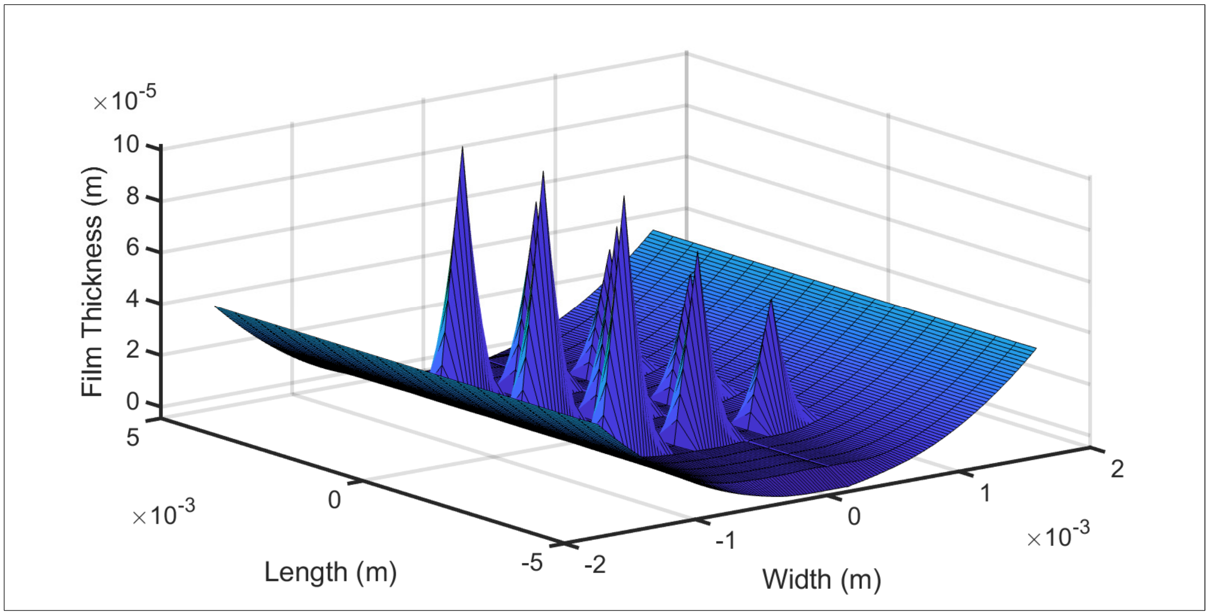

Figure 3.21 3D EHL Film thickness profile for the 9-pit configuration

To complete the analysis and better illustrate the multipit configuration effects, Figure 3.22 displays the 2D pressure distributions and film thickness profiles established at the axial position crossing the central pit (see Figure 3.17) of the configurations depicted in Figure 3.18 to Figure 3.21. The plots also include the smooth surface and the single pit conditions. The pressure distributions associated with these conditions were presented in Figure 3.14 (d).

The pressure chart demonstrates an obvious influence of the pit number and arrangement: comparing the single pit condition with the 3-pit configuration shows a maximum pressure increase from 1612 MPa for the single pit to 2100 MPa for the 3-pit configuration, while the smooth surface causes a maximum outlet pressure spike of 1210 MPa. In other words, the single pit causes a pressure increase at the spike position of 33.2% whereas the pressure spike rises of 73.6% with the 3 aligned pits. This observation clearly indicates the interaction existing between cavities aligned along the roller axis. It, therefore, reveals the potential loss of information with 2D simulations and evidences the need for 3D representations. Introducing two additional pit rows pushes the maximum pressure spike to 4000 MPa, which compared to the smooth condition corresponds to an augmentation of 230.6%. In clear, the pit influence results not only from longitudinal interactions among cavities on the same row but also from circumferential interactions among cavities situated at equal axial positions.

Pressure increases correspond to contact fatigue acceleration. Precise evaluations of the pressure distributions are thus crucial. On the other hand, the presence of cavities also affects the film thickness profiles. The plots in Figure 3.22 (b) indicate that the single pit condition and the 3-pit configuration provoke a reduction of the minimum film thickness from 0.71 μm for the smooth surface condition to 0.69 μm and 0.67 μm for the single pit and the 3 pit configurations, respectively. In other words, the single pit causes a minimum film thickness reduction at the pressure spike position of 2.8%, whereas the thickness reduction is of 5.6% with the 3 aligned pits. Again, this observation brings to light the interaction existing between cavities aligned along the roller axis and again underlines the potential loss of information with 2D simulations. The need for precise 3D representations similar to the present model is thus evident. Moreover, these results suggest that the presence of surface degradation has a stronger influence on pressure than on film thickness. It is hence logical to conjecture that once the surface cavity occurrence started, the contact fatigue process should accelerate, while the surface wear should demonstrate lower acceleration. The surface degradation certainly depends on the cavity size and density. Therefore, this description, which is solely based on the studied conditions, obviously calls for further analyses. This higher level of investigation is unfortunately out of the scope of the present thesis. Nevertheless, the addition of two pit rows tends to support this preliminary analysis, since it reduces the minimum film thickness to 0.51 μm, which compared to the smooth case correspond to a 28.1% decrease, whereas the pressure increases more than 230%.

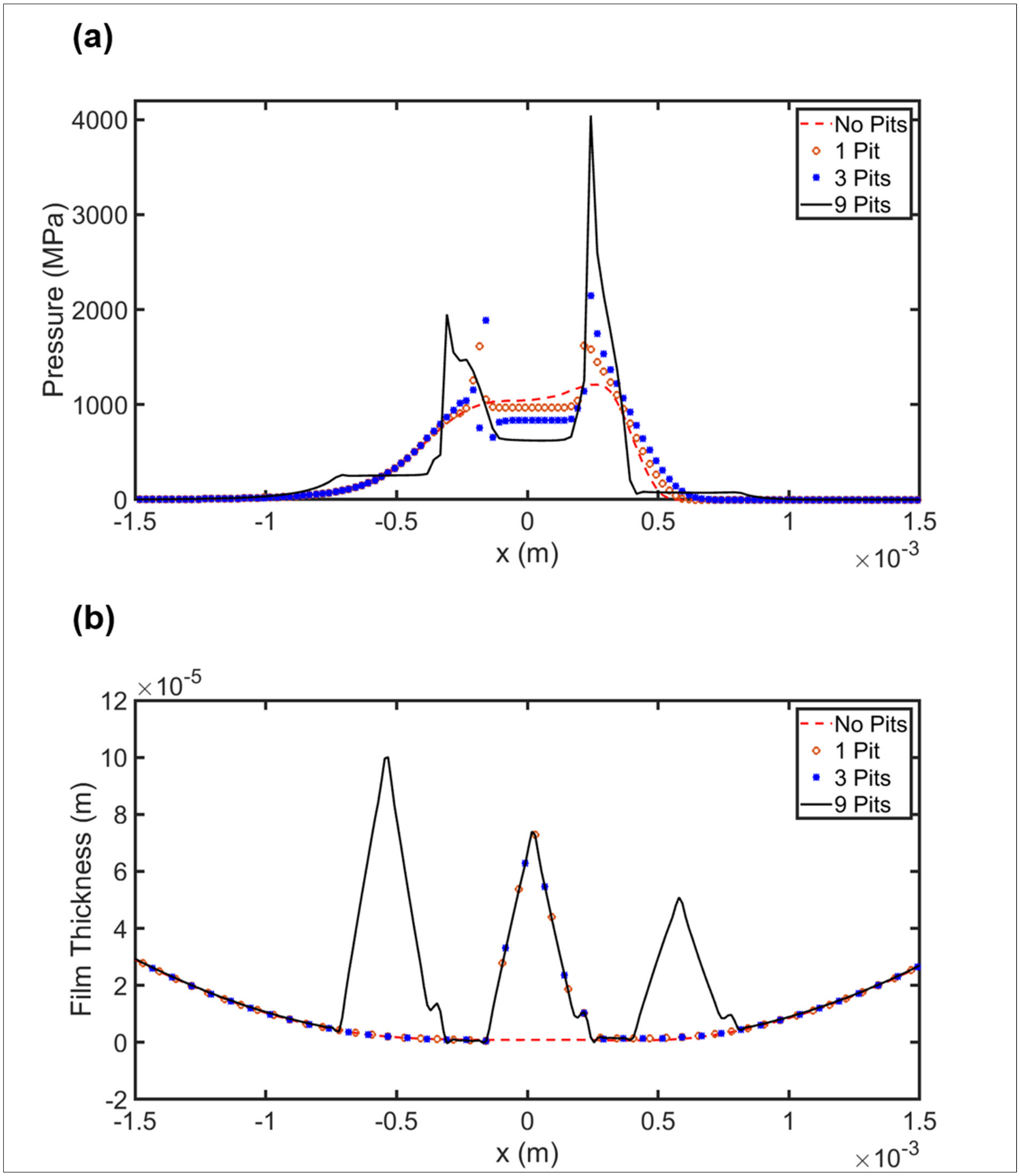

Figure 3.22 2D effect of pit configuration at the axial position crossing the central pit - (a) 2D EHL pressure distributions and (b) EHL film thickness profiles

Finally, Figure 3.23 presents the pressure and film thickness profiles along the length of the cylinders (at $x = 0$ mm). The previous analysis concentrated on the results evaluated at the position of the pressure spike. Now, this additional presentation of the results focuses on the longitudinal position traversing the contact area along the pit centers of the middle row. Figure 3.23 (a) presents the pressure distribution, while Figure 3.23 (b) displays the associated film thickness profile. The graphs also include a smooth condition.

Figure 3.23 (a) shows that compared to the smooth case, the cavity presence globally reduces the pressure. The plot also shows pressure drops at the pit position associated with pressure increases at the pit edges. However, these increases do not exceed the pressure evaluated at the end of the pit row, which means that the local stress concentration at the pit edge is negligible, and the pressure remains below that of the smooth condition. Compared to the 3-pit configuration, the 9-pit configuration leads to a significantly lower average pressure, which demonstrates the interaction among the pit rows. Moreover, the pressure spikes occurring at the roller ends required to control the longitudinal lubricant flow and avoid the violation of the continuity equation demonstrate reduced amplitudes with the pit numbers. The unequal separations between the pit row and the roller ends show that the studied distances cause no significant effect.

Because the pressure and film thickness are parameters with opposed responses, Figure 3.23 (b) shows that compared to the smooth case, the cavity presence globally increases the film thickness. Indeed, all pressure reductions are associated with film thickness augmentations. In fact, such responses are beneficial for both contact fatigue and wear lives. Nevertheless, since Figure 3.23 indicates that the longitudinal gains are associated with the worsening of the conditions in the circumferential direction, it gives the impression that there are probably optimal arrangements leading to overall gains. Actually, it seems unlikely that a degradation process would lead to a beneficial surface texturing and stop its evolution at this advantageous state. On the other hand, a performant texture might be generated onto the surface during the fabrication stage. Numerous papers have studied the influence of surface texturing in lubricated systems. The following references belong to the list ((Vrbka et al., 2010), (Taee, Torabi, Akbarzadeh, Khonsari, & Badrossamay, 2017), (Checo et al., 2014)). While in general, they do not consider line contact conditions, these studies demonstrate that the right balance between the cavity size and density remains difficult to establish. Therefore, while it is out of the scope of the present study, combining the proposed model with an optimization algorithm would probably identify potentially performant configurations. Such a simulation tool would be useful at the design stage of systems.

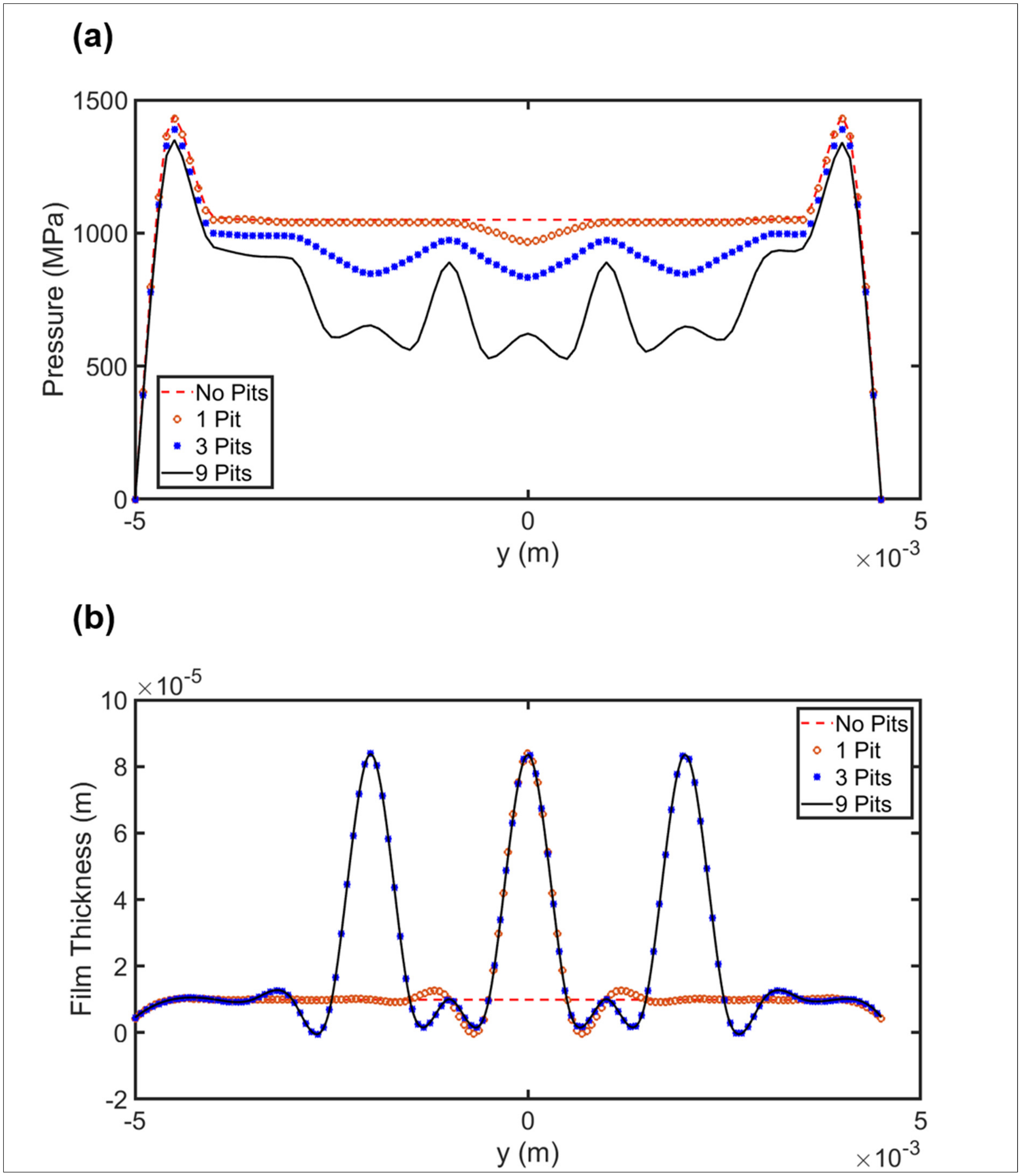

Figure 3.23 Longitudinal pressure distributions calculated along the x = 0 for two multipit configurations

So far, the study has focused on the effects of pitting on pressure distributions and lubricant film thickness profiles. However, friction remains another important aspect of the problem, which might be impacted by surface pitting (or desired surface texturing); the coefficient of friction between mating rollers depends on viscosity, slip ratio, and film thickness. The next section integrates the friction calculations into the model and investigates the consequences of surface irregularities on the friction response of a contact system.

3.8 Friction

The friction aspect plays an important role in the efficiency of systems such as gears, where the loads are transmitted through dynamic contacts. Experimental studies on EHL show that when the shear stress exceeds a critical value, calculated friction coefficients are far from experimental data (Evans, 2013). This shear stress limit is a property of each lubricant. The concept was previously defined in chapter 2. When accounting for the shear stress limit, numerical calculations of friction coefficients caused by viscous shearing provide precise predictions. Under EHL conditions sliding is the main cause of friction. Sliding between rollers is quantified by the slide to roll ratio (SRR) (Evans, 2013):

$$SRR = \frac{u_1 - u_2}{\left(\frac{u_1 + u_2}{2}\right)} \tag{3.4}$$

where u_1 and u_2 are the rolling speed of rollers 1 and 2, respectively. The friction force (F_f) is determined by integrating the shear stress (τ) over the contact area, as follows (Akchurin, Bosman, Lugt, & Van Drogen, 2015):

$$F_f = \int_A \tau dA \tag{3.5}$$

The classical expression given by Eq.(3.6) relates the shear stress to the viscosity and the flow velocity gradient through the film thickness (Evans, 2013). Eq. (3.7) formulates the flow velocity.

$$\tau = \eta \frac{\partial u}{\partial z} \tag{3.6}$$

$$u = \frac{1}{2\eta}\frac{\partial P}{\partial x}(z^2 - zh) + \left(1 - \frac{z}{h}\right)u_1 + \frac{z}{h}u_2 \tag{3.7}$$

Introducing Eq. (3.7) into Eq. (3.6) leads to the following expression for τ at the surface where $z = h$,

$$\tau = \frac{h}{2}\frac{\partial P}{\partial x} + \frac{\eta}{h}(u_1 - u_2) \tag{3.8}$$

For a contact region divided into $m \times n$ contact cells (of constant pressure as defined in chapter 1), the integral in Eq. (3.5) is written in a numerical form as:

$$F_f = \sum_{i=1}^{n-1}\sum_{j=1}^{m}\left[\frac{h_{i,j}}{2}\frac{\left(P_{i,j} - P_{i+1,j}\right)}{\Delta x} + \frac{\eta_{i,j}}{h_{i,j}}(u_1 - u_2)\right] \tag{3.9}$$

Eq. (3.9) clearly expresses the influence of the local pressure, viscosity, and film thickness values. Finally, the friction coefficient (*f*f_c) results from the ratio between the friction force and the external load (*F*).

$$f_c = \frac{F_f}{F} \tag{3.10}$$

After the calculation of the 3D pressure and film thickness distributions, Eqs. (3.9) and (3.10) provide a precise evaluation of f_c. The following sections describe the pit influence on f_c. In particular, they consider the pit configurations defined earlier. First, Section 3.8.1 validates the model via a comparison to values of friction coefficients published in (Najjari & Guilbault, 2014).

3.8.1 Validation-Calculation of friction coefficients

As indicated in chapter 2, the model involves an isothermal formulation. While under normal operating conditions, this simplification does not affect the precision of the film thickness and pressure distribution predictions, under significant heat generation this assumption will have a noticeable impact, especially on friction. To assess the precision of the model on friction predictions, this section reproduces the simulations presented by (Najjari & Guilbault, 2014) and compares the obtained results to the published values. Table 3.7 lists the simulation parameters taken from (Najjari & Guilbault, 2014). Figure 3.24 compares the friction coefficients predicted by the present model to those of the reference (Najjari & Guilbault, 2014). $f_c - SRR$ curves may be divided into two parts: the first describes the low SRR region, while the second corresponds to the high SRR values. In the low SRR section, friction coefficients increase linearly with SRR and reach a maximum amount around $SRR = 0.05$. On the other hand, in the second section ($SRR > 0.05$) friction coefficients decay with SRR increases.

The chart in Figure 3.24 indicates that the present model provides high precision levels on the friction coefficients calculated for SRR values below 0.05, which corresponds to a linear region. Conversely, for $SRR > 0.05$ the predicted friction coefficients deviate from the results reported by (Najjari & Guilbault, 2014). In fact, the high SRR value section is associated with high shear stresses. The shear stress reduces the lubricant viscosity. The Carreau's expression defined in chapter 2 introduces this relationship into the model. The high SRR section is also associated with high energy dissipation levels, and thus with important thermal effects and temperature increases; the temperature-dependent properties of the lubricant then demonstrate significant changes affecting the friction conditions (Evans, 2013). The isothermal simplification integrated into the developed model thus limits its application to the low SRR section. Actually, integrating the heat equation solution into the simulations does not represent a real challenge. Therefore, since the present research focuses on surface degradation integration into the Reynolds equation solution, it was estimated that putting the heat equation aside during the model development would allow isolating the degradation influence; the addition of the heat equation to the model might be realized in developments following the present thesis. Finally, since the f_c values obtained for high SRR are not valid, the following sections restrict the investigation to friction coefficients calculated in the low SRR region ($SRR \leq 0.05$), where the isothermal solution is valid.

Table 3.7 Rollers and lubricant properties Taken from (Najjari & Guilbault, 2014)

Elastic modulus (E)	200 GPa	Dimensionless speed ($U = \frac{\eta_0(u_1+u_2)}{2RE'}$)	7.3×10^{-11} 5.5×10^{-11} 3.6×10^{-11}
Poisson's ratio (ν)	0.3	Dimensionless load parameter ($W = \frac{w}{RE'}$)	1.3×10^{-4}
Equivalent radius R	20 mm	Dimensionless material parameter ($G = \alpha E'$)	3500
Ambient temperature T_0	313 K	Viscosity-pressure coefficient α	15.9 GPa^{-1}
Viscosity at T_0	0.04 Pa.s	Lubricant density ρ	846 kg/m^3
Modulus G_{f313K}	4.5 MPa	Slope factor n_{313K}	0.57
Modulus G_{f373K}	4.5 MPa	Slope factor n_{373K}	0.993

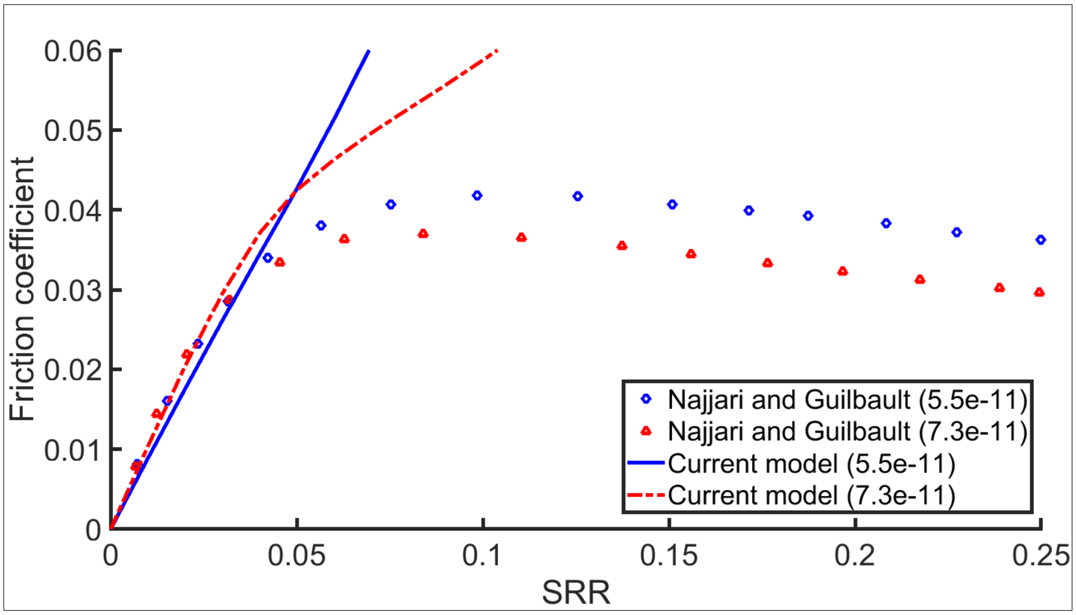

Figure 3.24 Comparing friction coefficient derived from the current model and reference (Najjari & Guilbault, 2014)

3.8.2 Single pit simulation

As mentioned before, the passage of pits through a contact zone affects the pressure distribution, the film thickness profile, as well as the associated friction coefficient. Figure 3.25 (a) compares the fluctuation of f_c caused by the movement of a single pit along the rolling direction with the smooth surface condition. These simulations consider a constant $SRR = 0.02$. The problem conditions are those described in Table 3.6. Besides, the G modulus and the slope factor η required for the Carreau's equation are: at 313 K, G_{f313} = 4.5 MPa, and η_{313} = 0.57 and at 373 K, G_{f373} = 4.5 MPa and η_{373} = 0.993.

Before the pit enters the contact region, the f_c values calculated for the pitted surface correspond to those of the smooth surfaces; the pressure distributions and the film thickness profiles predicted for the two conditions remain identical. When the pit enters the contact zone (pit location $x_p = -0.44 \times 10^{-3}\text{m}$) f_c attains its maximum. At this position, the lubricant accumulation in the pit causes a starvation condition in the lubricated contact. This starvation condition affects the pressure distribution causing a reduction similar to that calculated with

$SRR = 0$ and visible in Figure 3.14 (c). At the pit location ($x_p = 0$), the pit reaches the second half of the contact zone; the accumulated lubricant thus flows out of the pit and f_c drastically decreases. Finally, when the pit leaves the contact zone (pit location $x_p = 0.69 \times 10^{-3}$m), f_c merges with the values predicted for the smooth surfaces.

Figure 3.25 (b) compares the friction coefficients calculated for the single pit configuration to predictions made for the smooth surfaces over different SRR values of the low SRR region. The calculations consider a unique pit position corresponding to the center of the contact zone ($x_p = 0$). For both cases, when SRR increases from 0.01 to 0.05, f_c increases linearly. Overall, when compared to the f_c values established for the smooth conditions, the coefficient predicted for the single-pit case shows an increase of 8.55%. It goes without saying that the amplitude of the obtained results largely depends on the considered conditions (pit size, load and speed conditions, and lubricant), and corresponds to a given problem definition.

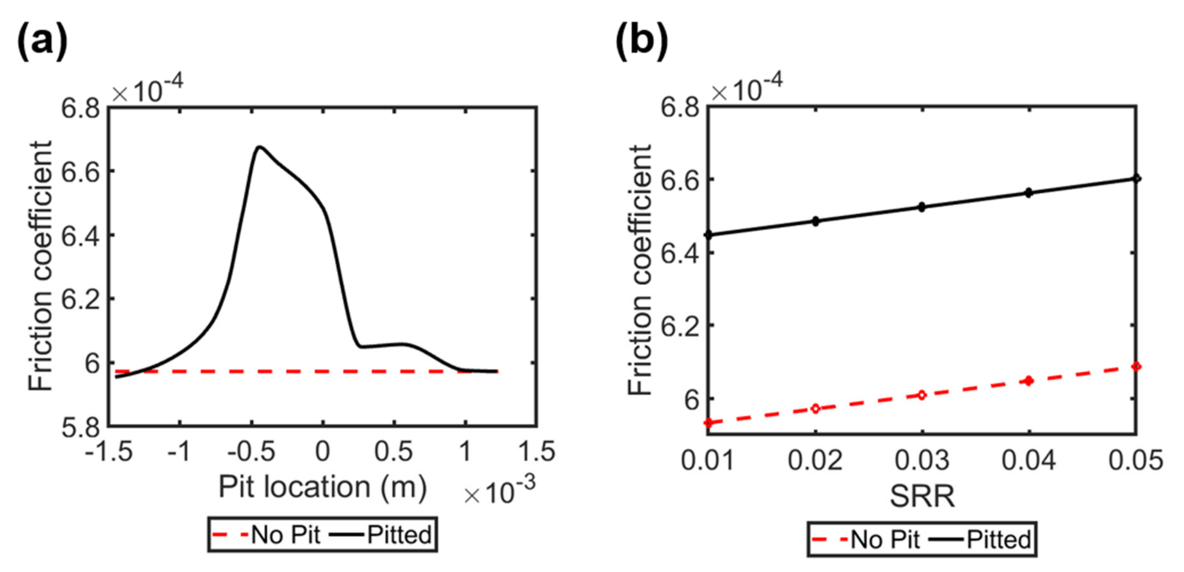

Figure 3.25 Effect of a single pit on the friction coefficient (a) Changes in friction coefficient with pit location in the contact zone when $\mathrm{SRR} = 0.02$, (b) Effect of SRR on friction coefficients calculated for the single pit and the smooth surface conditions.

3.8.3 Effect of pit depth

The pit depth is among the parameters affecting the friction response of pitted surfaces. Section 3.6 examined two pit depths. The following analysis establishes the friction coefficients for the same configurations. Figure 3.26 (a) shows the f_c variations during the passage of the two single-pit configurations (different depths) across the contact region, when the systems undergo an $SRR = 0.02$. The chart shows that increasing the depth amplifies the pit effects; while the two configurations demonstrate similar responses, compared to the smooth surface condition, the f_c augmentation is more intense with the larger pit depth.

Figure 3.26 (b) compares the friction response f_c obtained for the two pit depths with the smooth surface response over a range of SRR. As before, the friction amplitude linearly increases with SRR. Besides, compared to the smooth conditions, reducing the pit depth from 2.5×10^{-2} µm to 1.25×10^{-2} µm reduces the friction augmentation from 8.55% to 3.29%. It thus seems that the depth influence on f_c is not proportional to its amplitude. These preliminary results indicate that a deeper investigation is required to define the pit depth/friction coefficient relationship with more precision.

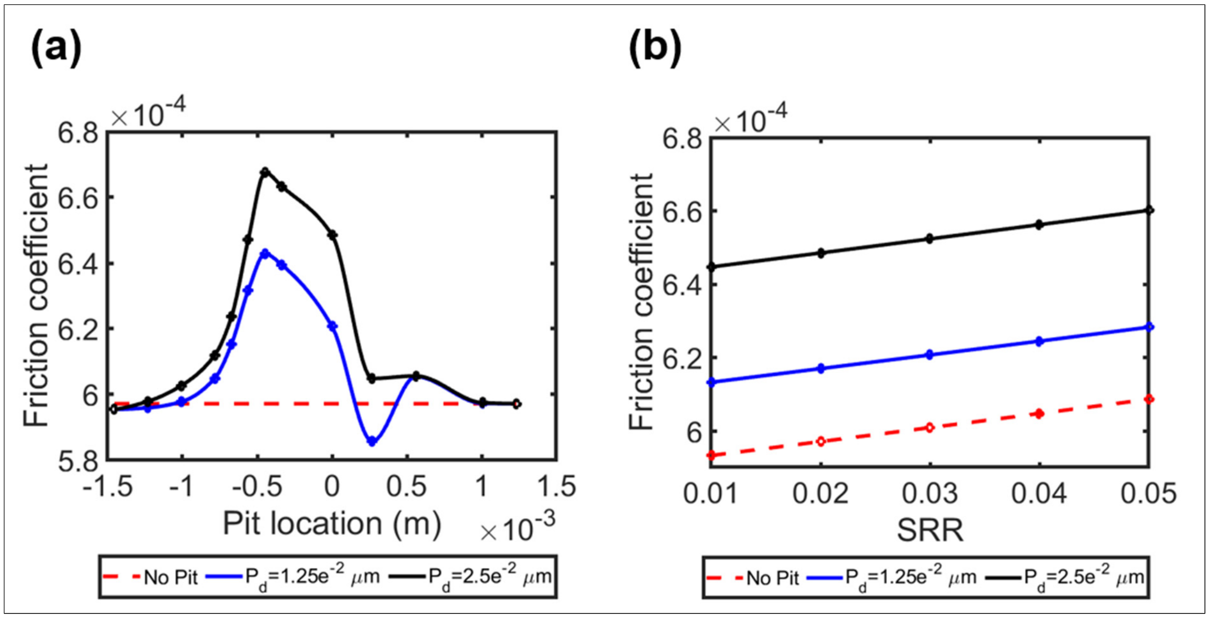

Figure 3.26 Effect of single pit depth on the friction coefficient (a) Changes in friction coefficient with pit location in the contact zone when $SRR = 0.02$, (b) Effect of SRR on friction coefficients calculated for single-pit configurations with different depths

3.8.4 Effect of pit arrangement

Section 3.7 demonstrated that the pit arrangement also significantly modifies the elastohydrodynamic response of a system. In this previous section, we derived the film thickness and pressure distributions for 9-pit and 3-pit arrangements. The following analysis examines the friction coefficients established for the same configurations when operating under SRR = 0.02. Figure 3.27 (a) shows the friction coefficients calculated for these two cases and compares the predicted responses with the single pit and the smooth-surface conditions. The lengthwise addition (along the y axis) of 2 pits to the single-pit case remarkably increases the f_c amplitude. However, since the pit arrangement in the flow direction (x) remains unaltered, the curve shape remains similar to that of the single-pit case. On the other hand, the 9-pit arrangement introduces two additional rows of 3 axial pits, which modifies the roller surface in both the axial and the flow directions (see Figure 3.17). In this case, the pit location axis in Figure 3.27 (a) describes the central pit row position. The graph displays significant impacts on both the shape and amplitude of the f_c distribution. The analysis of the single-pit case indicated that the moment a pit comes into a contact zone causes a starvation condition resulting in friction increase. The 9-pit configuration generates similar consequences each time a pit row enters the contact zone. The first f_c peak at the pit location $x_p = -1.0 \times 10^{-3}m$ is thus generated by the first pit-row (preceding the central pit row, at the right position in Figure 3.17), the second peak at the pit location $x_p = -0.45 \times 10^{-3}m$ results from the central row coming into the pressure zone, and finally the last peak on the right (at the pit location $x_p = 0$) develops when the last pit-row (at the left position in Figure 3.17) enters the contact area. The distance between the peaks is equal to the pit spacing (l_c+P_w=0.58 mm). The plateau at the pit location $x_p = 0.56 \times 10^{-3}m$ occurs when the last row exits the contact. The graph indicates that while the peak heights are comparable, the 3 rows have interconnected effects; the friction increase reduces from the first peak at the left position to the last on the right.

Figure 3.27 (b) shows the friction coefficient values calculated for the different configurations over the low *SRR* range. The chart displays the results obtained when the pit or the central pit-row is located at $x_p = 0$. Figure 3.27 (a) already revealed that at this position the single pit and the 3-pit row configurations practically produce equal coefficients of friction. On the other hand, the same graph indicates that at this position the 9-pit arrangement engenders a coefficient value 1.93 times higher. This substantial difference is a consequence of the last pit row entering the contact zone at that position. Figure 3.27 (b) shows for the considered range that the *SRR* amplitude lightly alters this proportion; the f_c linear rises demonstrated by the different configurations for *SRR* increases display slightly different slopes. Indeed the friction coefficient associated with the 9-pit arrangement tends to rise more rapidly than the other cases. As for the analyses presented before, these conclusions are dependent on the chosen conditions. For example, changing the selected pit location $x_p = 0$ for $x_p = 0.5 \times 10^{-3}m$ would have led to results with different proportions. Even though it is out of the scope of the present work, this observation again underlines the pertinence of deepening the investigation. The developed model would then represent a powerful tool.

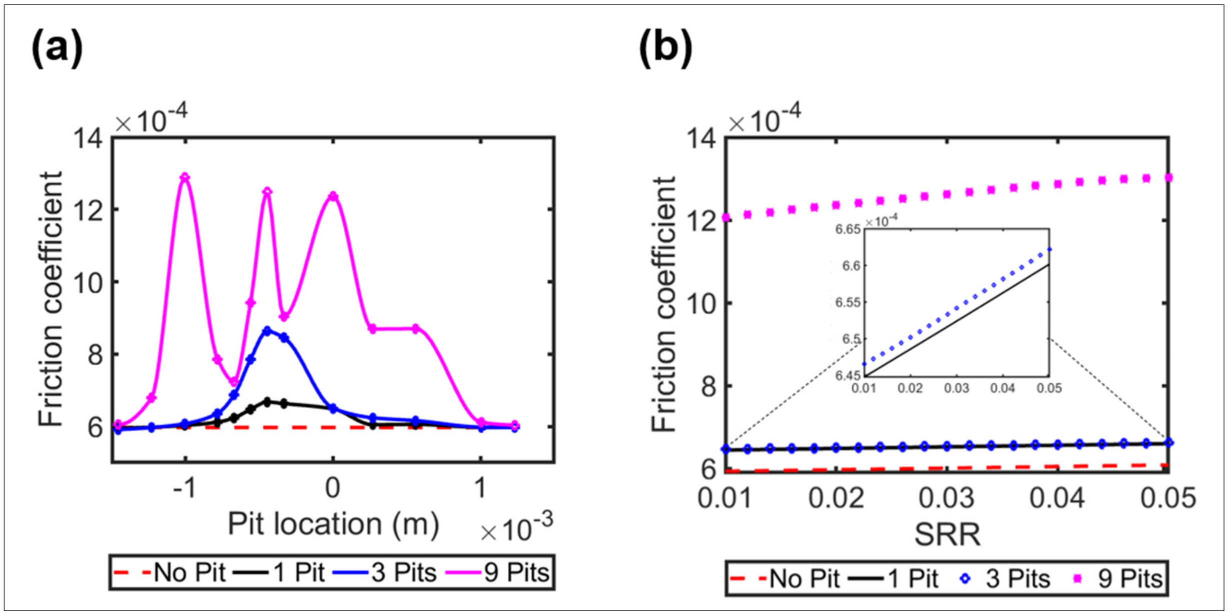

Figure 3.27 Effect of pits arrangement on the friction coefficient (a) Changes in friction coefficient with pit location in the contact zone when $SRR = 0.02$, (b) Effect of SRR on friction coefficients calculated for different pit arrangements

3.9 Conclusion

In this chapter, we modified the numerical formulation of the Reynolds equation to account for its time-variant term. The rotation of the rollers allows defining the pit position over its travel through the contact zone: entering, traversing, and exiting. Section 3.4 validated the developed model via a comparison with published numerical and experimental studies. Those reference papers detailed the effect of physical dents or dimples on the EHL mechanism. They demonstrate that the introduction of surface pits significantly affects the lubrication response. The validation process showed that the model prepared in this thesis precisely predicts the effects of surface irregularities on both pressure and film thickness distributions. After that, the simulation capacities provided by the model allowed describing the 3D consequences of various surface damages: pit depth, pit number, and arrangement.

The proposed approach includes Carreau's equation which allows the model to account for the non-Newtonian nature of lubricants. The prepared model only put the heat equation aside. It, therefore, provides isothermal simulations. Since the addition of this equation to the representation is not a real challenge, and because it may have a big impact on the results obtained under severe sliding conditions, to isolate the model ability to predict the surface irregularity role, it was decided not to include the heat solution in the version of the model developed in the present study; the heat equation may be integrated into the model after it is completely validated for isothermal problems involving degraded surfaces. Consequently, the presented model is valid only for the low amplitude of the slide-to-roll ratio.

The friction predictions obtained with the model were also validated via a comparison with results available in the literature. The proposed isothermal model offers precise predictions of f_c in the linear portion of the $f_c - SRR$ responses or when $SRR \leq 0.05$.

Since the research primary aim was the model preparation, the present thesis only includes preliminary descriptions of the consequences of some surface damages on friction response. Friction coefficients vary with pit location, size, and number. The presented simulations showed for the considered conditions that:

- The maximum f_c amplitude occurs when pits are in the inlet side of a contact zone.
- Pit depth increases cause f_c augmentations. However, the depth influence on f_c is not proportional to its amplitude.
- Increasing the pit number in the direction perpendicular to the flow causes an augmentation of the f_c amplitude but does not modify the friction response shape during the contact travel.
- Increasing the pit number in both the flow and the perpendicular directions significantly amplify the friction losses with an augmentation of the f_c amplitude and a modification of the f_c response shape over the contact travel.

CONCLUSION

In this dissertation, we extended the classic elastohydrodynamic lubrication solution to factor in surface defects such as pitting. The prepared model simulates the movement of two cylindrical rollers sustaining an external load. It predicts the 3D pressure distribution and lubricant film thickness, as well as the associated coefficient of friction. While the approach put forward is general, the present work concentrated on finite line contacts. These contacts include free surfaces at the roller ends, which result in more severe conditions and thus are way more difficult to model with precision.

To concentrate on the main objective of the research, which targeted the 3D solution of the Reynolds equation over irregular surfaces, it was decided not to include the heat equation in the first version of the model prepared in this thesis; the incorporation of the heat into the solution would later represent an easy step. The model is hence isothermal. Consequently, even though it incorporates the non-Newtonian nature of lubricants, the proposed modeling approach remains limited to running conditions involving low amplitude slide-to-roll ratios. The thesis chapters present the research developments through a systematic step-by-step procedure.

Chapter 1 presented the solution approach adopted for the dry contact problem. The model follows the method introduced by Hartnett. In order to eliminate the stress distributions on the free ends of the rollers inherited from the classic half-space theory, the final contact model completes the original Hartnett method: a pressure mirroring process eliminates the shear stress, while an additional correction factor removes the normal stress influence. The obtained predictions of the pressure distributions then take into account the exact plane stress condition at the roller limits and guarantee an accurate model of the finite contact length. Different in-plane and out-of-plane misalignments were studied to illustrate model precision and flexibility. This model establishes the elastic deformations of the bodies during the EHL simulation procedure presented in Chapter 2.

Chapter 2 describes the EHL model prepared to solve the Reynolds equation under isothermal conditions. Since this initial procedure is designed to model smooth surfaces, the adopted form of the Reynolds equation neglects the time derivative term, and hence reduces the problem to a purely geometrical formulation.

Although dry contact pressure distributions follow the Hertzian theory, the presence of lubricant extends the contact zone and engenders local pressure spikes. These spikes occur to maintain the mass continuity in the flow direction for the 2D simplification of the problem and in both the flow and axial directions (at the rollers ends) for the real 3D problem.

The EHL simulation procedure presented in Chapter 2 is time-independent and provides a steady-state solution. However, in the presence of damaged surfaces, the rotational movement introduces surface definitions that are time-dependent. Chapter 3 extended the model to rollers with pitted surfaces. Under this surface condition, which is common in machine elements, the time derivative term of the Reynolds equation can no longer be ignored and was therefore incorporated in the numerical solution.

Since the research primary aim was the model preparation, the present thesis only includes preliminary descriptions of the consequences of some surface damages. The studied cases examined the influence of the pit depth, the pit number, and the effects of multipit configurations. The obtained results demonstrated that the introduction of surface pits significantly affects both the pressure distributions and the film thickness profiles. The associated friction coefficients are also greatly impacted. The limited number of the studied cases showed that the friction coefficients vary with the pit location, size, and number. In summary, the considered conditions indicated that:

- Increases in friction coefficients are maximal when the pits are in the inlet zone of lubricated contacts.
- Friction coefficients increase with the pit depth.
- Pit number augmentation increases the friction losses.

RECOMMENDATIONS

Since the investigation presented in the thesis remains at a preliminary level, the studied cases underlined numerous elements calling for comprehensive investigations. However, the first aspect which has to be considered is the integration of the heat equation into the solution procedure. It is actually the sole limitation of the proposed model. Considering the heat equation will allow modeling contact conditions defined by high *SRR*.

Chapter 3 showed that the presence of cavities may potentially increase the film thickness, which is beneficial for both contact fatigue and wear lives. Therefore, it is reasonable to believe that a performant texture might be generated onto surfaces at the fabrication stage. However, the presented calculations showed that the longitudinal gains seem to be associated with worsening of the conditions in the circumferential direction. Moreover, the current literature demonstrates that the right balance between the cavity size and density in an optimal texture pattern remains difficult to establish. Thus, we may imagine that combining the proposed model with an optimization algorithm would potentially define performant configurations. This addition to the model certainly belongs to the near future works list.

Actually, the studied conditions suggested that the presence of surface degradation tends to provoke local increases in both the pressure and the film thickness. Moreover, the impact on the pressure appears to be larger than on the film thickness. In other words, while an optimal surface texturing might be beneficial, surface pits and holes normally promote the surface deterioration. Pressure increases exceeding the material fatigue strength will accelerate the contact fatigue process, whereas film thickness augmentations will reduce surface wear. The exact consequences on surface degradation certainly depend on the cavity size and density. In clear, the limited extent of the conditions examined in the present study could not clarify the real relationship existing between the interacting factors, but instead strongly calls for further analyses. As a matter of fact, the questions raised by the presented case studies are not limited to the pressure and film thickness aspects, but also concern the friction facet; deeper investigations are required to define with more precision the pit size, depth, and density relationship with friction. The developed model should then be seen as a helpful tool for those future investigations. This model should thus be considered as the main contribution of the thesis.

LIST OF BIBLIOGRAPHICAL REFERENCES

Akchurin, A., Bosman, R., Lugt, P. M., & Van Drogen, M. (2015). On a model for the prediction of the friction coefficient in mixed lubrication based on a load-sharing concept with measured surface roughness. *Tribology Letters*, *59*(1), 1–11. https://doi.org/10.1007/s11249-015-0536-z

Bolander, N. W., & Sadeghi, F. (2006). Surface modification for piston ring and liner. *Solid Mechanics and Its Applications*, *134*, 271–283. https://doi.org/10.1007/1-4020-4533-6_19

Checo, H. M., Ausas, R. F., Jai, M., Cadalen, J. P., Choukroun, F., & Buscaglia, G. C. (2014). Moving textures: Simulation of a ring sliding on a textured liner. *Tribology International*, *72*, 131–142. https://doi.org/10.1016/j.triboint.2013.12.013

Chong, W. W. F., & De La Cruz, M. (2014). Elastoplastic contact of rough surfaces: A line contact model for boundary regime of lubrication. *Meccanica*, *49*(5), 1177–1191. https://doi.org/10.1007/s11012-013-9861-1

Chue, C. H., & Chung, H. H. (2000). Pitting formation under rolling contact. *Theoretical and Applied Fracture Mechanics*, *34*(1), 1–9. https://doi.org/10.1016/S0167-8442(00)00019-7

Collins, D. (2015). Roller rail guides: Three reasons why you should use them. Retrieved May 7, 2020, from https://www.linearmotiontips.com/three-reasons-use-roller-rail-guides/

Datsyshyn, O. P., & Panasyuk, V. V. (2001). Pitting of the rolling bodies contact surface. *Wear*, *250–251*(PART 2), 1347–1355. https://doi.org/10.1016/s0043-1648(01)00771-2

de Mul, J. M., Kalker, J. J., & Fredriksson, B. (1986). The contact between arbitrarily curved bodies of finite dimensions. *Journal of Tribology*, *108*(1), 140–148. https://doi.org/10.1115/1.3261134

Defects treated (gears) | Novexa. (n.d.). Retrieved May 7, 2020, from https://www.novexa.com/defects-treated/?lang=en

Dowson, D., & Higginson, G. (1967). Book: Elasto-hydrodynamic lubrication: The fundamentals of roller and gear lubrication. *Wear*, *10*(3), 246. https://doi.org/10.1016/0043-1648(67)90018-x

Dumont, M. L., Lugt, P. M., & Tripp, J. H. (2002). Surface feature effects in starved circular EHL contacts. *Journal of Tribology*, *124*(2), 358–366. https://doi.org/10.1115/1.1403457

Elcoate, C. D., Evans, H. P., & Hughes, T. G. (1998). On the coupling of the elastohydrodynamic problem. *Proceedings of the Institution of Mechanical Engineers, Part C: Journal of Mechanical Engineering Science*, *212*(4), 307–318. https://doi.org/10.1243/0954406981521240

Evans, R. D. (2013). Traction (Definition and Measurement). In *Encyclopedia of Tribology* (pp. 3713–3718). https://doi.org/10.1007/978-0-387-92897-5_220

Fajdiga, G., Flašker, J., & Glodež, S. (2004). The influence of different parameters on surface pitting of contacting mechanical elements. *Engineering Fracture Mechanics*, *71*(4–6), 747–758. https://doi.org/10.1016/S0013-7944(03)00022-5

Fajdiga, G., Glodež, S., & Kramar, J. (2007). Pitting formation due to surface and subsurface initiated fatigue crack growth in contacting mechanical elements. *Wear*, *262*(9–10), 1217–1224. https://doi.org/10.1016/j.wear.2006.11.016

Gelinck, E. R. M., & Schipper, D. J. (2000). Calculation of Stribeck curves for line contacts. *Tribology International*, *33*(3–4), 175–181. https://doi.org/10.1016/S0301-679X(00)00024-4

Ghosh, M. k. (1985). Thermal elastohydrodynamic lubrication of line contacts. *ASLE Transactions*, *28*(2), 159–171. https://doi.org/10.1080/05698198508981608

Greenwood, J. A., & Morales-Espejel, G. E. (1995). Pressure Spikes in EHL. *Tribology Series*, *30*(C), 555–564. https://doi.org/10.1016/S0167-8922(08)70660-6

Grubin, A. N., & Vinogradova, I. E. (1949). Fundamentals of the hydrodynamic theory of lubrication of heavily loaded cylindrical surfaces. *Investigation of the Contact Machine Components*, (30), 115–166. Retrieved from https://ci.nii.ac.jp/naid/10012874266/

Guilbault, R. (2011). A fast correction for elastic quarter-space applied to 3D modeling of edge contact problems. *Journal of Tribology*, *133*(3). https://doi.org/10.1115/1.4003766

Guilbault, R. (2013). A simplified thermal analysis of elastohydrodynamic contacts. *Journal of Tribology*, *135*(2). https://doi.org/10.1115/1.4023085

Guilbault, R., & Lalonde, S. (2019). A stochastic prediction of roughness evolution in dynamic contact modelling applied to gear mild wear and contact fatigue. *Tribology International*, *140*, 105854. https://doi.org/10.1016/j.triboint.2019.105854

Hamrock, B. J., & Tripp, J. H. (1984). Numerical methods and computers used in elastohydrodynamic lubrication. *Developments in Numerical and Experimental Methods Applied to Tribology*, 11–19. https://doi.org/10.3233/SJI-2011-0713

Hamrock, B. J., & Dowson, D. (1975). ISOTHERMAL ELASTOHYDRODYNAMIC LUBRICATION OF POINT CONTACTS - 1. THEORETICAL FORMULATION. *American Society of Mechanical Engineers (Paper)*, (75-Lub-11). Retrieved from https://asmedigitalcollection.asme.org/tribology/article-abstract/98/2/223/419780

Hartnett, M. J. (1980). GENERAL NUMERICAL SOLUTION FOR ELASTIC BODY CONTACT PROBLEMS. *American Society of Mechanical Engineers, Applied Mechanics Division, AMD*, *39*, 51–66.

He, T., Ren, N., Zhu, D., & Wang, J. (2014). Plasto-elastohydrodynamic lubrication in point contacts for surfaces with three-dimensional sinusoidal waviness and real machined roughness. *Journal of Tribology*, *136*(3). https://doi.org/10.1115/1.4027478

Hertz, H. (1896). On the contact of rigid elastic solids. *J. Reine Und Angewandte Mathematik*, *92*, 156.

Höhn, B. R., Michaelis, K., & Kreil, O. (2006). Influence of surface roughness on pressure distribution and film thickness in EHL-contacts. *Tribology International*, *39*(12), 1719–1725. https://doi.org/10.1016/j.triboint.2006.01.008

Houpert, L. G., & Hamrock, B. J. (1986). Fast approach for calculating film thicknesses and pressures in elastohydrodynamically lubricated contacts at high loads. *Statistical Journal of the IAOS*, 411–419. https://doi.org/10.3233/SJI-2011-0713

Keer, L. M., & Bryant, M. D. (1983). A pitting model for rolling contact fatigue. *Journal of Tribology*, *105*(2), 198–205. https://doi.org/10.1115/1.3254565

KURODA, S., & ARAI, K. (1985). Elastohydrodynamic lubrication between two rollers: Finite width analysis. *Bulletin of JSME*, *28*(241), 1367–1372. Retrieved from https://www.jstage.jst.go.jp/article/jsme1958/28/241/28_241_1367/_article/-char/ja/

Kushwaha, M., Rahnejat, H., & Gohar, R. (2002). Aligned and misaligned contacts of rollers to races in elastohydrodynamic finite line conjunctions. *Proceedings of the Institution of*

Mechanical Engineers, Part C: Journal of Mechanical Engineering Science, *216*(11), 1051–1070. https://doi.org/10.1243/095440602761609434

Li, S., & Kahraman, A. (2013). A physics-based model to predict micro-pitting lives of lubricated point contacts. *International Journal of Fatigue*, *47*, 205–215. https://doi.org/10.1016/j.ijfatigue.2012.09.002

Liu, S., Wang, Q., & Liu, G. (2000). A versatile method of discrete convolution and FFT (DC-FFT) for contact analyses. *Wear*, *243*(1–2), 101–111. https://doi.org/10.1016/S0043-1648(00)00427-0

Liu, Y. (2013). Flash Temperature in EHL Contacts. In *Encyclopedia of Tribology* (pp. 1172–1182). https://doi.org/10.1007/978-0-387-92897-5_653

Masjedi, M., & Khonsari, M. M. (2015). On the effect of surface roughness in point-contact EHL: Formulas for film thickness and asperity load. *Tribology International*, *82*(PA), 228–244. https://doi.org/10.1016/j.triboint.2014.09.010

Mostofi, A., & Gohar, R. (1983). Elastohydrodynamic lubrication of finite line contacts. *Journal of Tribology*, *105*(4), 598–604. https://doi.org/10.1115/1.3254683

Najjari, M., & Guilbault, R. (2014). Edge contact effect on thermal elastohydrodynamic lubrication of finite contact lines. *Tribology International*, *71*, 50–61. https://doi.org/10.1016/j.triboint.2013.11.005

Okamura, H. (1983). A contribution to the numerical analysis of isothermal elastohydrodynamic lubrication. *Ci.Nii.Ac.Jp*, ((Publishers) Ltd., 1983, Session XI, Paper XI(iii)). https://doi.org/10.1016/b978-0-408-22161-0.50048-2

Olver, A. V., & Dini, D. (2007). Roughness in lubricated rolling contact: The dry contact limit. *Proceedings of the Institution of Mechanical Engineers, Part J: Journal of Engineering Tribology*, *221*(7), 787–791. https://doi.org/10.1243/13506501JET318

Park, T. J. (2010). Effect of roller profile and misalignment in ehl of finite line contacts. *ASME 2010 10th Biennial Conference on Engineering Systems Design and Analysis, ESDA2010*, *1*, 395–401. https://doi.org/10.1115/ESDA2010-24367

Park, T. J., & Kim, K. W. (1998). Elastohydrodynamic lubrication of a finite line contact. *Wear*, *223*(1–2), 102–109. https://doi.org/10.1016/S0043-1648(98)00317-2

Polishing - Gear failures - Failure Atlas - ONYX InSight. (n.d.). Retrieved May 7, 2020, from https://onyxinsight.com/wind-turbine-failures-encyclopedia/gear-failures/macropitting/

Shirzadegan, M. (2016). *Elastohydrodynamic Lubrication of Cam and Roller Follower*. Retrieved from http://www.diva-portal.org/smash/record.jsf?pid=diva2:999453

Taee, M., Torabi, A., Akbarzadeh, S., Khonsari, M. M., & Badrossamay, M. (2017). On the Performance of EHL Contacts with Textured Surfaces. *Tribology Letters*, *65*(3), 1–12. https://doi.org/10.1007/s11249-017-0871-3

Vrbka, M., Šamánek, O., Šperka, P., Návrat, T., Křupka, I., & Hartl, M. (2010). Effect of surface texturing on rolling contact fatigue within mixed lubricated non-conformal rolling/sliding contacts. *Tribology International*, *43*(8), 1457–1465. https://doi.org/10.1016/j.triboint.2010.02.002

Warhadpande, A., & Sadeghi, F. (2010). Effects of surface defects on rolling contact fatigue of heavily loaded lubricated contacts. *Proceedings of the Institution of Mechanical Engineers, Part J: Journal of Engineering Tribology*, *224*(10), 1061–1077. https://doi.org/10.1243/13506501JET785

Wolff, R., Nonaka, T., Kubo, A., & Matsuo, K. (1992). Thermal elastohydrodpamic lubrication of rolling/sliding line contacts. *Journal of Tribology*, *114*(4), 706–713. https://doi.org/10.1115/1.2920939

Wymer, D. G., & Cameron, A. (1974). ELASTOHYDRODYNAMIC LUBRICATION OF A LINE CONTACT. *Inst Mech Eng (Lond) Proc*, *188*(19), 221–238. https://doi.org/10.1243/PIME_PROC_1974_188_024_02

Zhu, D., Ren, N., & Wang, Q. J. (2009). Pitting life prediction based on a 3D line contact mixed EHL analysis and subsurface von Mises stress calculation. *Journal of Tribology*, *131*(4), 1–8. https://doi.org/10.1115/1.3195040

Zhu, D., Wang, Q. J., & Ren, N. (2009). Pitting Life Prediction Based on a 3-D Line Contact Mixed EHL Analysis and Subsurface von Mises Stress Calculation. In *Advanced Tribology* (pp. 178–179). https://doi.org/10.1007/978-3-642-03653-8_59